Adding New Functionalities to Optical Fiber Cavities by Direct Laser Writing

Dissertation
zur
Erlangung des Doktorgrades (Dr. rer. nat.)
der
Mathematisch-Naturwissenschaftlichen Fakultät
der
Rheinischen Friedrich-Wilhelms-Universität Bonn

vorgelegt von
Alexander Faßbender
aus
Bonn

Bonn 2023

Angefertigt mit Genehmigung der Mathematisch-Naturwissenschaftlichen Fakultät der Rheinischen Friedrich-Wilhelms-Universität Bonn.

1. Gutachter:	Prof. Dr. Stefan Linden
2. Gutachterin:	Priv.-Doz. Dr. Elisabeth Soergel
Tag der Promotion:	12.06.2023
Erscheinungsjahr:	2023

Abstract

Fiber Fabry–Pérot cavities (FFPCs) are fiber-based optical cavities, which find widespread applications, for example, in cavity quantum electrodynamics, spectroscopy, sensing, metrology, and in many more fields. They provide a range of advantages over other types of optical cavities: The input and output of the cavity are directly fiber-coupled, the cavity is easily tunable, additional components can be brought into the cavity region to study their interaction with the cavity mode, the overall cavity length can be reduced to micrometer sizes in order to reach high coupling strengths, and the setup allows for access to the cavity volume due to the comparably small diameter of the fibers. FFPCs can be assembled inside ferrules, which provide mechanical stability. In this configuration, FFPCs can be universally applied in various environments without worrying about mechanical damages or alignment-disturbance of the fragile fiber construct. This enables, for example, the installation of an FFPC in a cryostat.
Direct laser writing (DLW) allows for the fabrication of polymeric structures on a wide range of surfaces. The process of two-photon absorption enables three-dimensional prints with features on the sub-micrometer scale. A large number of resists with different optical and mechanical properties have been developed and serve for applications in photonics, micromechanics, material science, and many more.
In this thesis, we combine both areas by manipulating optical fibers, designed for the usage in FFPCs, by structures fabricated via DLW. In the following, a polymeric membrane is fabricated on top of a fiber mirror or on a distributed Bragg reflector substrate. It is suspended via its feet and therefore serves as a mechanical structure with characteristic eigenmodes. When this fiber/substrate is used in a Fabry–Pérot cavity setup, the radiative field in the cavity and the mechanical mode of the membrane interact. We extract the coupling strength between the fundamental mechanical mode and the radiative field and investigate the temperature-dependent behavior of the mechanical linewidth and the mechanical resonance frequency. Furthermore, we present the tunability of the mechanical resonance by using the optical spring effect.
In the second part of this thesis, an approach for manipulation of optical fibers via equipping fiber with metallic electrodes is developed. The procedure involves the creation of a polymeric structure via DLW, here serving as a mask for a thermal evaporation procedure. In the experiment, a metallic coating is applied all around the fiber and on its endfacet. Upon removal of the mask, the fiber remains with the created shadow structure. This structure can be used to apply an electric or a magnetic field directly within the FFPC, making the usage of additional electrodes in the cavity region obsolete.

Contents

CHAPTER 1

Introduction

An optical cavity is a resonator for light and allows for a huge number of roundtrips per photon. Therefore, it can be utilized for increasing the intensity of a light field. Optical resonators have been realized in various ways [1]: Whispering-gallery mode resonators [2], photonic crystal resonators [3], microdisk resonators [4], microsphere resonators [5], and Fabry–Pérot [6] cavities pose some examples.
The applications of optical cavities spread over a wide range: They enabled the emergence of the laser [7], allow for trapping of ions and atoms [8], serve for spectroscopy [9], and sensing [10]. Fabry–Pérot cavities [11, 12], constructed by two opposing mirrors, allow for the interaction with additional material by inserting the material in between the mirrors. Further advantages over other types of resonators include the simple tunability, the support of a large number of modes, and their easy setup.
Fabry–Pérot cavities are utilized in various experiments yielding for strong light-matter interaction, e.g., experiments aiming for the strong-coupling regime [13]. In the field of cavity quantum electrodynamics, the interaction of light with trapped microscopic particles is mostly realized with Fabry–Pérot cavities. Prominent examples comprising the optical cavity setup built by mirrors can be associated with the Nobel prizes in physics in the years 2005, 2012, and 2017: Precision spectroscopy with an optical frequency comb [14, 15], the manipulation and measurement of individual quantum systems [16, 17], and the LIGO experiment [18–20], detecting gravitational waves via measuring the induced length change of an interferometric arm, all rely on optical cavities.

The field of optomechanics is dedicated to the interaction between a mechanical motion and a radiative field. One of those systems is typically used for the manipulation of the other one, e.g., by exciting a mechanical oscillation via light. The underlying mechanism for the interaction of the mechanical and the optical system is the radiation pressure of light, the transfer of the photon momentum. Effects arising from this interaction can be observed on a very large scale, for example in the form of comets' tails [21]: Small particles, ablated from the comet, are subject to radiation pressure due to solar photons, and hence a curved trail can be observed. On a very small scale, the transfer of radiation pressure can be utilized to trap a microscopic object by optical tweezers [22]. Since the typical momentum of a single photon is comparably small,

an amplification of the light-matter interaction is desirable. In the case of the comet's tail, an enormous number of interactions can take place. For the interaction between a microscopic trapped particle, the usage of optical cavities has proven successful due to their aforementioned ability of enhancing the field [8, 23].
It has been shown that the optomechanical interaction can be used for a wide range of applications [24], e.g., for the cooling of the mechanical motion [25] leading to resolved-sideband cooling [26, 27]. Furthermore, quantum-coherent coupling [28], meaning the coupling rate between the mechanical and radiative mode exceeds both individual decoherence rates, has been presented. The high sensitivity of the underlying interaction process paves the way for cavity-enhanced spectroscopy and sensing [29], as well as precision sensing applications [30], and microwave-to-optics conversion [31].
Previous experiments showed that optomechanical systems can be embedded in a vast majority of the optical resonator setups [32, 33], such as whispering-gallery mode resonators [34], photonic crystal resonators [35], microdisk resonators [36], and Fabry–Pérot cavities [37]. In the aforementioned LIGO experiment, optomechanical effects come into play and disturb the measurement, as this experiment has to tackle the thermally-induced vibrations of the mirror position [38].

The length of a cavity influences its capability: The coupling between a particle and the intra-cavity field increases the smaller the mode volume is. Short cavities allow for more roundtrips of a photon before it decays so that stronger fields can be obtained compared to the longer counterparts. Hence, the length of a cavity is typically kept as short as possible. Here, the special category of Fabry–Pérot cavities comes into play.

Fiber Fabry–Pérot cavities (FFPCs) feature advantageous properties compared to their free-space-coupled counterparts [39, 40]: The cavity itself is inevitably fiber-coupled, which simplifies the in- and outcoupling of light. The dimensions of commonly used optical fibers (diameter of 125 µm) allow for a compact design. The fibers can be positioned close to each other (on the micrometer scale) to obtain a minimal resonator mode volume, thus enabling high coupling strengths for the light-matter interaction. In addition, the resonator provides good accessibility, e.g., for the insertion of additional material, approaches with electrodes, or additional laser beams. Ferrules that can be used to assemble FFPCs provide a sturdy and protective basis [41]. Therefore, the FFPCs may be exposed to harsh environments, e.g., mounted in a cryostat.
However, the application of FFPCs in combination with trapped microscopic particles or integrated optomechanical structures also features downsides. Regarding trapped particles, it is often desirable or necessary to apply electric or magnetic fields at the position of the trapped (charged) particle. This is often realized by adding metallic tips into the cavity region that can then be used to emit an electric field. Therefore, the overall built volume needed for the realization of a cavity is strongly increased. In addition, this setup requires more alignment than the pure fiber cavity, since the electrodes are positioned as close as possible to the microscopic particle. Another challenge arises due to the small distance between the fibers and the particle: A charged microparticle induces a charge accumulation on a dielectric fiber surface. This accumulation gives rise to an electric field disturbing the charged particle.

In optomechanical experiments, commonly used membranes, such as silicon nitride films, require a suspension [33, 42]. Therefore, the mounting of such a membrane within an FFPC setup requires a periphery holding the membrane, which increases the overall setup size.
These challenges will be tackled in this thesis by applying a fabrication process allowing three-dimensional prints of polymeric material on the microscopic scale.

In classical optomechanical experiments, the membrane has a thickness in the order of λ of the light used, for example by using silicon nitride films as membranes [43, 44]. Here, we exploit membrane thicknesses in the order of several micrometers while probing the cavity at 780 nm. The membrane is fabricated by direct laser writing (DLW), based on a two-photon absorption process [45]. This technique provides a powerful tool for the fabrication of polymeric structures on a variety of interfaces. The commonly used resists comprise optical properties that qualify them for a wide range of applications in photonics [46], for example for the creation of a three-dimensional photonic crystal [47, 48] or the fabrication of objectives [49]. Likewise, the mechanical properties of the resists have been well exploited and used, e.g., in micromechanics [50, 51]. Here, both aspects of the resists interplay and build the platform for our experiments: DLW allows for the creation of almost arbitrary three-dimensional structures on a range of surfaces [52, 53], amongst others on the endfacet of optical fibers [54–56].

In the first part of this work, we utilize the versatile DLW fabrication process for optomechanical experiments in FFPCs. An FFPC is equipped with a polymeric membrane that, on the one hand, locally changes the refractive index inside the cavity. On the other hand, the implemented structure oscillates, and thus, the position of refractive index change is continuously modulated. This oscillation is either induced due to thermal motion or can be actively controlled by manipulation via radiation force.
In its simple form, the mechanical structure consists of a rectangular membrane supported by two feet. The fundamental flexural mode of this configuration corresponds to a simple oscillation of the membrane, where in one direction, two oscillation nodes are located directly at the position of the supporting feet of the membrane and in the other direction, no node is present. However, the versatile fabrication process via DLW enables almost arbitrary structures. In order to reduce damping, additional slits in the structure could reduce the energy loss to the underlying fiber. Likewise, multiple membranes can be stacked on top of each other, resulting in a coupled system.
In the experiment, the effect of the dielectric membrane on the cavity shall be exploited. Light, emitted by a laser, is coupled into the cavity. Reflection spectra are recorded during the scanning of the cavity length in search for a high coupling. The cavity itself can be locked to the laser frequency to ensure a pure measurement of the mechanical mode. From this, the mechanical motion of the structure can be characterized and the coupling between light and matter can be measured. The fabrication via DLW allows for the fabrication of the structure directly on top of a mirror substrate or on top of a fiber mirror. Hence, a finished cavity setup, comprising a fiber-fiber cavity with integrated optomechanical structure, occupies a space of less than $5 \cdot 10^{-4}\,\mathrm{mm}^3$. Making use of the compact and rigid setup by a ferrule-based implementation of the fiber-fiber cavity, it is exposed to vacuum and cryogenic temperatures and

the corresponding performance is measured, aiming for a regime, where the coupling strength and the resonance shift arising due to the optical spring effect surpasses the mechanical linewidth.

The combination of DLW with the field of fiber optics opens the door to more applications. We investigate the possibility to create structured metalizations on a fiber endfacets. These structures may serve for the application of electric or magnetic fields inside an FFPC, e.g., electric fields for the manipulation of ions, magnetic fields for the stimulation of nitrogen-vacancy centers, or just bare ground potential to prevent charge accumulation on fiber ends. The approach taken here involves the fabrication of a DLW-printed mask on a bare glass substrate. A fiber is then inserted into the mask, which shields parts of the fiber in a thermal evaporation process. Upon removal of the mask, the structured fiber can be electrically contacted to external wires. We present the metalization of fibers with various structures, starting from just a single electrode to four electrodes and to an Ω-shaped antenna.

In Ch. 2, the theoretical foundations for the description of the optomechanical interaction will be investigated. We start with the fundamentals of cavities and fiber optics, the foundations of FFPCs, optomechanical interactions, as well as the stabilization schemes of optical cavities. Chapter 3 deals with the fabrication principles of polymeric structures via the DLW system, as well as the surface evaluation of the structures created. At the beginning of Ch. 4, a finite element solving procedure is applied for investigating the estimated mechanical resonances. Next, the optical setups for the characterization of the optomechanical coupling and the optical spring effect are described. Following, the analysis of the data is presented. In Ch. 5, the second project of this thesis is presented: A method to apply a structured metallic coating to a fiber serving, e.g., as electrodes/antenna for the application of electric/magnetic fields, is developed. Here, the polymeric structure serves as a mask during the thermal evaporation procedure. Finally, Ch. 6 provides an outlook on possible further investigations and applications.

CHAPTER 2

Theoretical Foundations

A photon of wavelength λ carries a momentum of $p = h/\lambda$ with Planck constant h. Hence, the interaction between an optical field and a mechanical motion, resulting from momentum transfer, is typically weak concerning a single photon. To obtain a measurable quantity, e.g., for the observation of light-influenced mechanical systems, an increased number of interactions is necessary. Optical cavities with high reflective mirrors have previously proven as a suitable platform for such interactions since a photon can typically oscillate several thousand times in the cavity before it is lost through its decay.
In this chapter, the basics of optical cavities are examined, including their modes and stability criteria. Then, the particular case of fiber Fabry–Pérot cavities (FFPCs) is presented. Subsequently, the interactions of mechanical structures with optical fields are investigated: The foundations of optomechanics are briefly reviewed, including an introduction to the figures of merit of such systems.

2.1 Optical Cavities

A high optical field concentration helps to obtain a measurable light-matter interaction. This high field concentration can be be achieved by a setup that allows a single photon to interact multiple times with the mechanical system. Hence, cavity setups feature an increased field strength due to multiple reflections of light. In a two-mirror cavity, e.g., a single photon is reflected multiple times back and forth and the local intensity scales with the mean number of reflections. This allows for a vast number of applications: In 1960, when the first laser was presented, an optical cavity formed the core of the new invention since it allowed for the interaction with the laser's gain medium and performed wavelength-selective.
Optical cavities have become a powerful tool in the world of photonics and even beyond. The strong light-matter interaction allows, e.g., for a sufficiently high number of possible interactions of a single ion/atom/molecule with the light field [57–59]. Furthermore, the reflection signal is highly sensitive to the material that is inserted between the mirrors. Hence, the measurement of, for example, optical extinction rates is possible with cavity ring-down spectroscopy [9]. But as the cavity reflection signal is not only highly dependent on the properties of the medium between the mirrors but also on the geometrical setup, it can be used for precise spatial measurements:

The LIGO experiment uses Fabry–Pérot cavities for the determination of spatial displacements. In fact, that experiment and the application presented in this thesis have a common ground: Both can be characterized as optomechanical experiments based on Fabry–Pérot resonators.

2.1.1 Fabry–Pérot Cavities

Various platforms for the realization of optical cavities exist: Whispering-gallery mode resonators, photonic crystals, microspheres, or nano-rods [33] are a few examples of the spectrum of realized systems. The cavities considered here consist of two opposing parallel surfaces that reflect light back and forth [6, 60]. For example, two mirrors can form a resonator that gives rise to a standing wave pattern in between. Depending on the resonator's geometry, the supported wavelength changes, and different transversal and longitudinal modes emerge.
In this sense, a Fabry–Pérot cavity is an optical cavity whose two mirrors do not have unity reflectivity but allow a small amount of light to be transmitted. The mirror properties may strongly vary in terms of reflectivity, transmittance, and supported bandwidth, since they are selected according to the application and the size of the cavity. The outcoupled light via transmission through one of those mirrors is used in our experiments to investigate and characterize the resonator.

Longitudinal Modes A scheme of the fields in a Fabry–Pérot resonator is given in Fig 2.1. The resonator considered here is entirely defined by the length L of the cavity and the properties of the mirrors M_i, namely their corresponding reflectivity (r_i, $r_i = \sqrt{\mathcal{R}_i}$), transmittance ($t_i$, $t_i = \sqrt{\mathcal{T}_i}$), and losses ($l_i$, $l_i = \sqrt{\mathcal{L}_i}$, $\mathcal{R}_i + \mathcal{T}_i + \mathcal{L}_i = 1$), which can be attributed to scattering, diffraction, and absorption. The electric field that builds up inside the resonator can be expressed as the sum of the initial incoupled field and the series of fields reflected in the resonator:

$$E_{\mathrm{circ}} = \imath t_1 E_{\mathrm{in}} \left(1 + r_1 r_2 \mathrm{e}^{\imath\phi} + \left(r_1 r_2 \mathrm{e}^{\imath\phi}\right)^2 + \ldots\right) \tag{2.1}$$

$$= \imath t_1 E_{\mathrm{in}} \frac{1}{1 - r_1 r_2 \mathrm{e}^{\imath\phi}}, \tag{2.2}$$

with $\mathrm{e}^{\imath\phi}$ representing the phase shift accumulated during a round-trip in the cavity. The criterion for constructive interference inside the resonator demands the light field to reproduce after the reflection off the two mirrors. Thus, the total phase shift after one round trip $\delta = k \cdot 2L'$ needs to be an integer multiple of 2π. Here, the used optical length L' depends on the refractive index n of the medium inside the resonator $L' = nL$. In the following, we assume $n = 1$.
Since the fields in the cavity are not directly measurable, an expression for the reflected or transmitted field is needed. Here, we concentrate on the reflected field. In accordance with Fig. 2.1 the reflected electric field can be expressed as the composition of a directly reflected part from the incoming field, which never entered the resonator, and the outcoupling of the resonator:

$$E_{\mathrm{r}} = r_1 E_{\mathrm{in}} + r_2 \imath t_1 E_{\mathrm{circ}} \mathrm{e}^{\imath\phi} \tag{2.3}$$

$$= E_{\mathrm{in}} \left(\frac{r_1 - r_2(1 - \mathcal{L})\mathrm{e}^{\imath\phi}}{1 - r_1 r_2 \mathrm{e}^{\imath\phi}}\right). \tag{2.4}$$

It is assumed $\mathcal{L}_1 = \mathcal{L}_2$ as well as $\mathcal{L} \ll 1$. In a measurement, we determine the reflected power, which is given by $P \propto |E|^2$

$$P_r = P_{\text{in}} \mathcal{T} \frac{\mathcal{F}^2}{\pi^2} \frac{1}{1 + 4\frac{\mathcal{F}^2}{\pi^2} \sin^2\left(2\pi \frac{\nu}{2\Delta\nu_{\text{FSR}}}\right)}. \tag{2.5}$$

Figure 2.2 shows the reflected power in dependence on the frequency. The graph depicts various longitudinal modes that are supported by the resonator. They are separated in frequency space by the free spectral range (FSR), defined by

$$\Delta\nu_{\text{FSR}} = \nu_{\text{N+1}} - \nu_{\text{N}} = \frac{c}{2L}, \tag{2.6}$$

where ν_N is the frequency that fulfills the condition $\nu_N = N \cdot c/(2L)$, with integer N. The quotient

$$\frac{\Delta\nu_{\text{FSR}}}{\Delta\nu_{\text{FWHM}}} = \mathcal{F} = \frac{\pi r}{1 - r^2} \tag{2.7}$$

defines the so-called finesse $\mathcal{F}$ with the assumption $r_1 = r_2$ [6, 61]. Here, $\Delta\nu_{\text{FWHM}}$ denotes the full width at half maximum (FWHM).

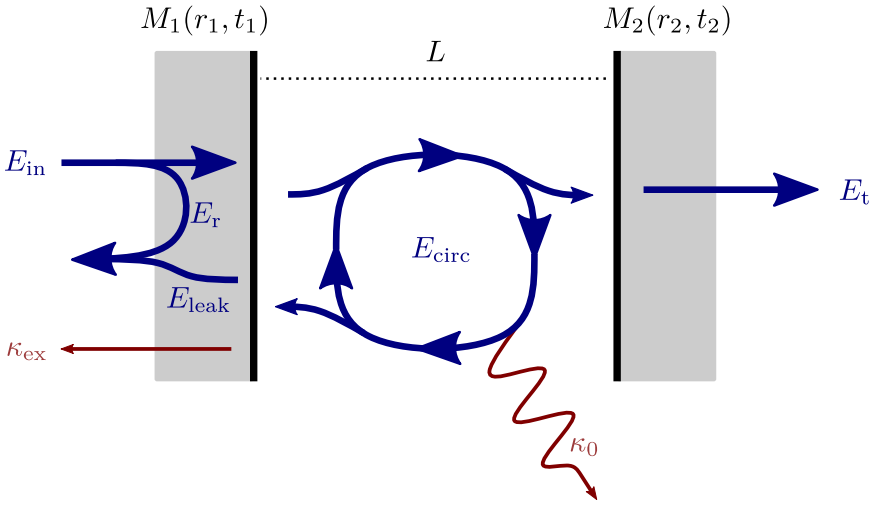

Figure 2.1: Schematic view on the present fields in a resonator setup: Depending on the mirrors' properties, the incoming electric field (E_{in}) is partially reflected (E_{r}) and partially contributes to the field inside the resonator (E_{circ}).

Transversal Modes The cavity is operated at a transversal eigenmode, whose phase profile reproduces itself after each reflection by the mirror. This condition requires the mirror curvature and wavefront to coincide. Transversal electromagnetic modes TEM_{nm} are denoted with the number of nodes n and m in the x- and y-direction of the beam's intensity cross section. Depending on the setup of the cavity, different modes are supported. For a perfectly aligned

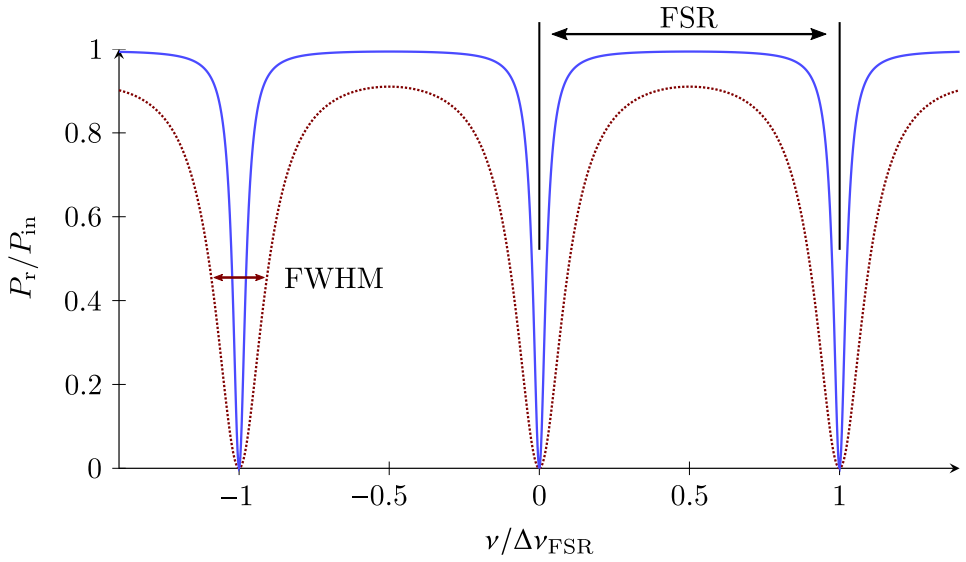

Figure 2.2: Reflection spectrum of a Fabry–Pérot cavity. The lineshape depends on the number of roundtrips the light can take before it leaves the cavity. This quantity can be quantified by the so-called finesse, defined as the ratio of the free spectral range between two supported modes and the full width at half maximum of such a mode.

resonator, we would expect that after exciting the fundamental TEM_{00} mode, only this mode is present, even after numerous cavity reflection trips. Higher-order modes play an increasing role when dealing with misalignments or imperfections in the mirrors.

2.1.2 Loss Channels and Stability Criteria

To achieve sufficient intensity in the cavity, one needs to maximize the energy that can be coupled into the cavity and simultaneously reduce the occurring losses inside. Responsible for the first is impedance-matching, which describes the amount of incoming power which can be stored in the cavity. A cavity is called impedance-matched if the loss rates in one roundtrip of the light are exactly equal to the contemporary inserted energy rate:

$$\mathcal{T}_1 = 2\mathcal{L} + \mathcal{T}_2. \tag{2.8}$$

In this case, the cavity is critically coupled, meaning the reflected power vanishes. If the incoupled energy rate exceeds the loss rate, the cavity is overcoupled. It is undercoupled if the loss rate dominates the incoupled energy rate and the cavity continuously loses energy to the surrounding. The suppression of reflections on resonance, or equivalently the impedance matching, can be quantified with the impedance matching factor

$$\eta_{\mathrm{imp}} = 1 - \left(\frac{\mathcal{T}_2 - \mathcal{T}_1 + 2\mathcal{L}}{\mathcal{T}_2 + \mathcal{T}_1 + 2\mathcal{L}}\right)^2. \tag{2.9}$$

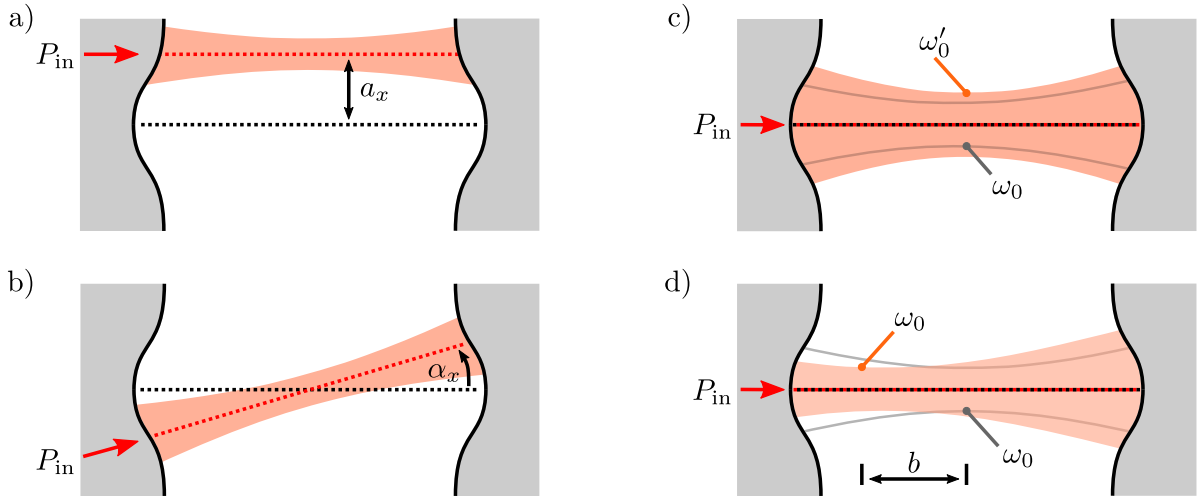

Figure 2.3: Possible cavity misalignments include a) an offset, or b) a tilt between the input axis and the cavity axis, c) a mode mismatch in size, or d) position of input mode and cavity mode, compare [62]. The contour in the resonator in c) and d) indicates the fundamental mode of the cavity.

For the measurements, an overcoupled state is preferred: In an overcoupled state, cavity fluctuations do not influence the reflection signal as strong as in the impedance matched case. The losses of the cavity are dominated by the losses due to outcoupling, which enables the observation of the cavity performance in reflection mode. In addition, internal losses arise. These contributions can be divided into different channels, e.g., losses due to various types of misalignment, the aforementioned inherent losses occurring at the mirrors, or clipping losses. Misalignment of the input beam and the cavity axis can result in coupling to off-axis eigenmodes of the cavity [62]. Figure 2.3 depicts a set of possible misalignments, e.g., displacements of input axis and cavity axis or mode waist mismatches. These examples emphasize the importance of well-fabricated and placed mirror shots and the relative alignment of the surfaces in the experimental setup.
Clipping losses play a prominent role when considering a fiber-based cavity: Due to the size of the fiber, the possible mirror radius is finite. If the mode diameter exceeds the area of the usable mirror, the mode is clipped, and energy leaves the cavity. This emphasizes the importance of a high-quality fiber mirror fabrication procedure.
A further criterion concerns the geometry of the cavity: Mirrors come in different shapes, but not all combinations allow to build a stable cavity that enables light to be reflected multiple times back and forth. One possibility to define the stability is based on an approach using the transfer matrix method [63]. The g-parameter is defined as $\mathrm{g}_i = 1 - L/R_i$, with R_i being the radius of the mirror [6]. The cavity is said to be stable if it fulfills

$$0 \leq \mathrm{g}_1\mathrm{g}_2 \leq 1. \tag{2.10}$$

Figure 2.4 shows this relation, including some prominent mirror geometry combinations.

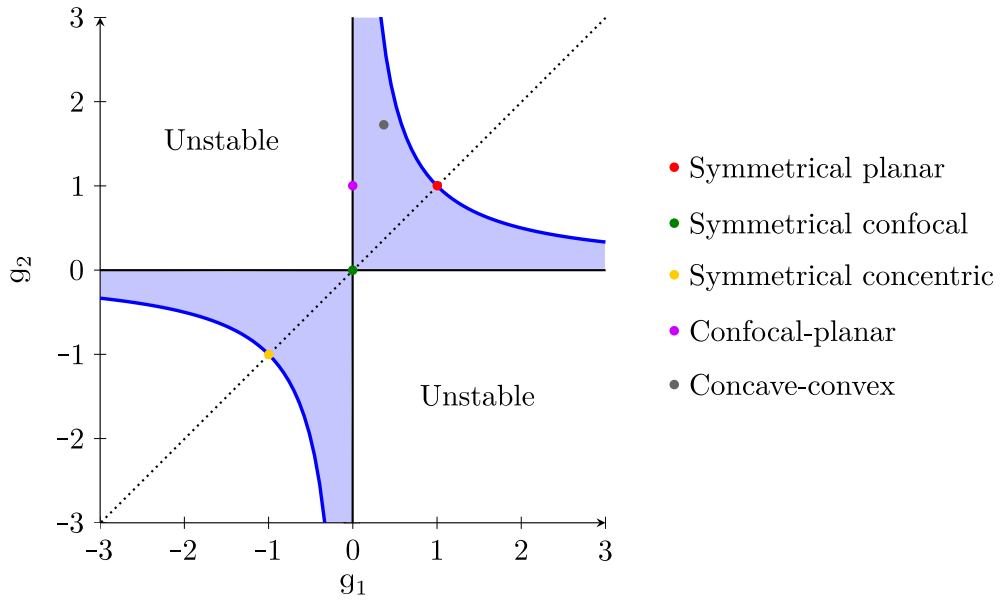

Figure 2.4: Stability diagram for a cavity, assembled from two mirrors with the respective g_i-parameters. Some prominent mirror geometry combinations are highlighted.

2.1.3 Fiber Fabry–Pérot Cavities

Optical fibers are used to guide light at low losses over large distances. This is achieved by their internal structure. The working principle of conventional optical fibers relies on total internal reflection, thus a fiber features a composition of materials with different refractive indices. Via reflection and refraction, the light is guided along the fiber. The size of the fiber core and the kind of refractive index transition from core to shell determines the optical properties of the fiber. Various fibers for specific purposes, e.g., single-mode or multi-mode fibers, are available. In the following, we deal with single-mode fibers, which support the fundamental mode solely. Fiber Fabry–Pérot cavities unite several advantageous properties: The cavity is inherently fiber-coupled, which provides a simplified incoupling of light into the cavity. In addition, the outcoupled light is directly coupled into the fiber (if it matches the fiber mode), resulting in a streamlined setup.
By using fiber for building cavities, not only the whole experimental setup becomes more compact, in particular the cavity itself can be downsized: The fibers' diameter amounts to 125 µm, while classical mirror substrates have a diameter of 12.7 mm. Hence, when a cavity is formed by positioning two half-inch mirrors very close to each other (in the order of $\approx 100\,\mu$m), the mode region is hard to reach. This can be an issue if, e.g., additional electrodes or laser are required within the cavity region. In contrast, the open geometry of an FFPC provides convenient access to the resonator mode, allowing, e.g., the implementation of electrodes nearby that apply electric fields for the manipulation of ions. Due to the small size of the fibers, the approach with electrodes or laser beams can be realized, even at an angle. For the presented optomechanical realizations, the typical fiber cavity length is in the order of 30 µm.
Therefore, the cavity volume is strongly reduced. This compactness is, on the one hand, beneficial regarding miniaturization, and, on the other hand, it also serves a physical purpose:

The coupling between the intra-cavity field and, e.g., an atomic ensemble scales with the mode volume V_{mode} via $V_{\text{mode}}^{-\frac{1}{2}}$. Thus, a small mode volume enhances the coupling.
Due to the reduced cavity length, the resulting large number of roundtrips, and the small mode volume, high field strengths can be achieved, and losses attributed to cavity length are strongly reduced.
Furthermore, FFPCs can become outstanding robust if, for example, both fibers are inserted into a ferrule and glued in place. A rigid setup allows for a wide range of applications that go beyond the applications in the lab environment: A robust assembly can for example be used in a vacuum or cryogenic surrounding, which does not allow for mechanical tuning as, e.g., re-aligning the fibers, once the corresponding chamber is evacuated. These properties let FFPCs stand out as a powerful platform for the implementation of a variety of experiments, including the optomechanical ones we focus on here.
In contrast to free-space Fabry–Pérot cavities, the fiber-based Fabry–Pérot cavities show an asymmetric resonance lineshape in reflection mode. It turns out that this asymmetry is independent of power and polarization and emerges as a result of the inherent mode matching to the fiber-guided modes. In the following, the lineshape will be briefly reviewed from a mathematical point of view. The derivation closely follows those given in [64–66].
Using the Dirac notation [67], the electric fields involved are noted as

$$E_i = \mathcal{E}_i \left|\psi_i\right\rangle , \tag{2.11}$$

with $\mathcal{E}_i$ being the complex-valued amplitude of the field, including the time dependence $\exp(\imath\omega t)$. The involved modes are the forward and backward traveling modes in free-space or in the fiber, respectively, $\left|\psi_{\text{f}}^{+}\right\rangle$ and $\left|\psi_{\text{f}}^{-}\right\rangle$, the forward and backward traveling modes in the cavity $\left|\psi_{\text{cav}}^{+}\right\rangle$ and $\left|\psi_{\text{cav}}^{-}\right\rangle$, and the reflection of the first mirror denoted by $\left|\psi_{\text{r}}\right\rangle$.
Thus, the incoming light field is described via

$$E_{\text{in}} = \mathcal{E}_{\text{in}} \left|\psi_{\text{f}}^{+}\right\rangle , \tag{2.12}$$

while the intra-cavity field can be described as (compare Eq. 2.2)

$$E_{\text{circ}} = \mathcal{E}_{\text{in}} \frac{\imath t_1 \left\langle \psi_{\text{cav}}^{+} \middle| \psi_{\text{f}}^{+} \right\rangle}{1 - r_1 r_2 \mathrm{e}^{\imath\phi}} \left|\psi_{\text{cav}}^{+}\right\rangle . \tag{2.13}$$

With this, the leaking field that is transmitted through mirror 1 becomes

$$E_{\text{leak}} = \imath t_1 \mathcal{E}_{\text{circ}} r_2 \mathrm{e}^{\imath\phi} \left|\psi_{\text{cav}}^{-}\right\rangle \tag{2.14}$$

$$= \mathcal{E}_{\text{in}} \frac{-t_1^2 r_2 \mathrm{e}^{\imath\phi}}{1 - r_1 r_2 \mathrm{e}^{\imath\phi}} \left\langle \psi_{\text{cav}}^{+} \middle| \psi_{f}^{+} \right\rangle \left|\psi_{\text{cav}}^{-}\right\rangle . \tag{2.15}$$

In order to simplify the notation, we replace

$$\xi = \frac{t_1^2 r_2 e^{\imath\phi}}{1 - r_1 r_2 e^{\imath\phi}}. \tag{2.16}$$

Another contribution to the measurement in reflection arises from the directly reflected field, which never entered the cavity:

$$E_\mathrm{r} = r_1 \mathcal{E}_\mathrm{in} \left|\psi_\mathrm{r}\right\rangle . \tag{2.17}$$

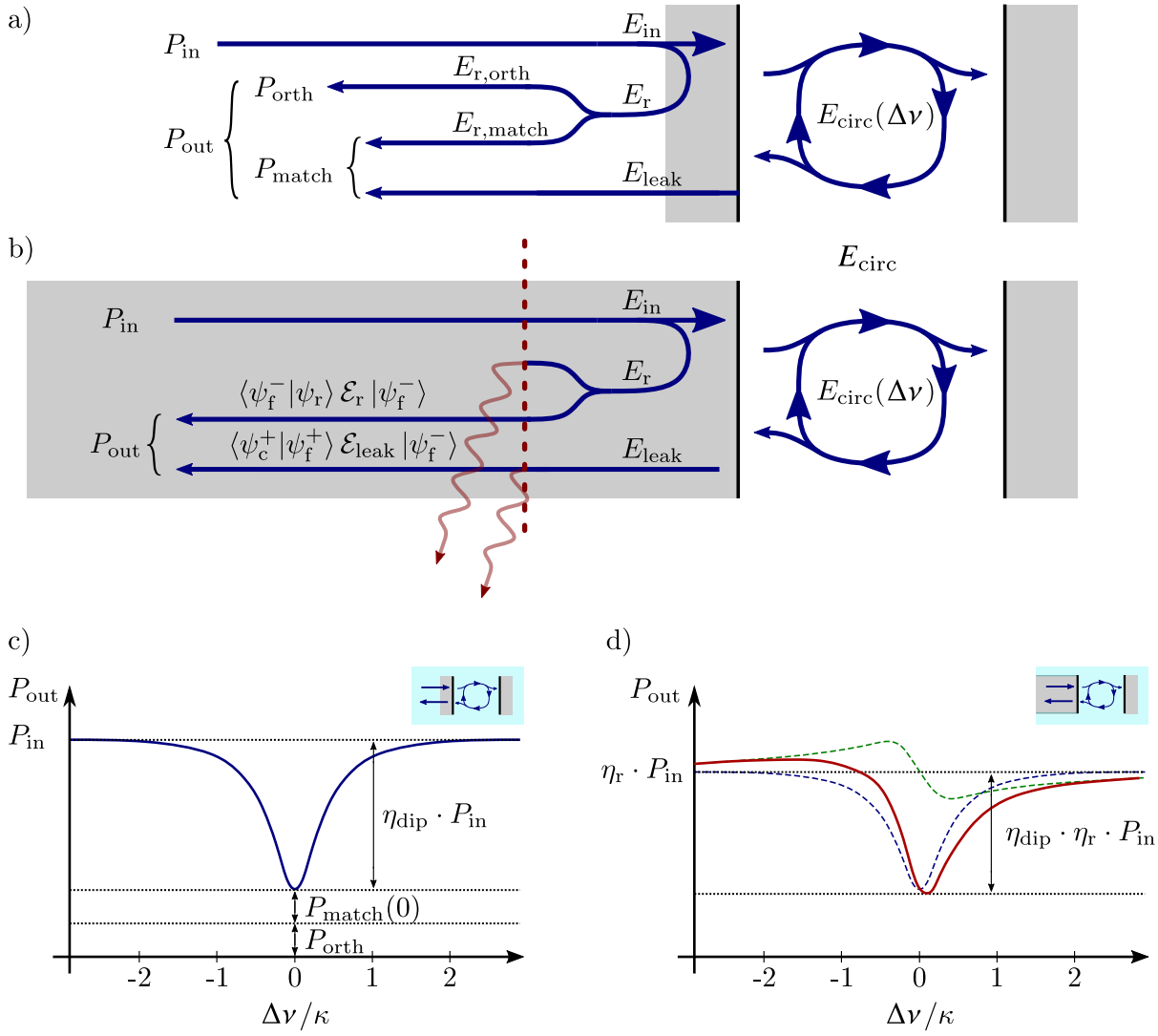

Figure 2.5: Schematic view of a) a free-space-coupled cavity and b) a fiber-coupled cavity. Values for the derivation of the reflected power spectrum are supplied. Measurements of the reflected power reveal a) a Lorentzian lineshape for the free-space-coupled cavity, while b) the fiber-coupled cavity inhibits an additional dispersive behaviour on top of the Lorentzian. Compare [64, 65].

The reflected field can be split up into two parts, which are orthogonal to each other. In the case of free-space Fabry–Pérot cavities, one part can be chosen to interfere with the leaking field from the cavity mode, while the other one does not interfere, compare Fig. 2.5a. The total intensity measured in reflection mode consists of the superposition of those. In the case of a fiber-coupled Fabry–Pérot cavity, the considerations can be done equivalently with the exception that the fiber does not allow for all the reflected or leaking light to pass through: If the mode does not match to the fiber, the light is coupled into the cladding and absorbed, compare Fig. 2.5b. Therefore, the reflected intensity signal behaves significantly different.

Free-Space-Coupled Cavities Starting with the free-space coupled cavities, the reflected field is split up into a matched reflection field $E_{\mathrm{r,\,match}}$ and an orthogonal field $E_{\mathrm{r,\,orth}}$:

$$E_{\mathrm{r,\,match}} = r_1 \left\langle \psi_{\mathrm{cav}}^{-} \middle| \mathcal{E}_{\mathrm{r}} \right\rangle \left| \psi_{\mathrm{cav}}^{-} \right\rangle \tag{2.18}$$

$$= r_1 \mathcal{E}_{\mathrm{in}} \left\langle \psi_{\mathrm{cav}}^{-} \middle| \psi_{\mathrm{r}} \right\rangle \left| \psi_{\mathrm{cav}}^{-} \right\rangle . \tag{2.19}$$

This is the mode-matched field that undergoes interference with the leaked field E_{leak}. The orthogonal component can be calculated as the remaining contribution:

$$E_{\mathrm{r,\,orth}} = E_{\mathrm{r}} - E_{\mathrm{r,\,match}} = r_1 \mathcal{E}_{\mathrm{in}} \left(|\psi_{\mathrm{r}}\rangle - \left\langle \psi_{\mathrm{cav}}^{-} \middle| \psi_{\mathrm{r}} \right\rangle \left| \psi_{\mathrm{cav}}^{-} \right\rangle \right) . \tag{2.20}$$

For the experimental realization, high reflectivity mirrors are used, thus r_1 is in the following approximated as $r_1 \approx 1$. The total power leaving the cavity in reflection configuration can be expressed as

$$P_{\mathrm{out}} = P_{\mathrm{r,\,orth}} + P_{\mathrm{r,\,match}}. \tag{2.21}$$

Applying the properties of the Dirac notation for complex conjugates $(\langle\psi_i|)^\dagger = |\psi_i\rangle$ and $(|\psi_i\rangle)^\dagger = \langle\psi_i|$, as well as the normalization of the wave functions, P_{out} is determined using $P_i = {E_i}^\dagger E_i$ via

$$P_{\mathrm{out}} = E_{\mathrm{r,\,orth}}^{\dagger} E_{\mathrm{r,\,orth}} + \left(E_{\mathrm{r,\,match}} + E_{\mathrm{leak}} \right)^{\dagger} \left(E_{\mathrm{r,\,match}} + E_{\mathrm{leak}} \right) . \tag{2.22}$$

In the following, the overlap of the cavity mode and the reflected field is defined as $\left\langle \psi_{\mathrm{cav}}^{-} \middle| \psi_{\mathrm{r}} \right\rangle = \alpha$, so $\left\langle \psi_{\mathrm{cav}}^{-} \middle| \psi_{\mathrm{r}} \right\rangle \left\langle \psi_{\mathrm{r}} \middle| \psi_{\mathrm{cav}}^{-} \right\rangle = |\alpha|^2$. Alongside this definition, the overlap integral of $\left\langle \psi_{\mathrm{cav}}^{+} \middle| \psi_{\mathrm{f}}^{+} \right\rangle$ can be rephrased

$$\left\langle \psi_{\mathrm{cav}}^{+} \middle| \psi_{\mathrm{f}}^{+} \right\rangle = \left\langle \psi_{\mathrm{cav}}^{+} \right| R^\dagger R \left| \psi_{\mathrm{f}}^{+} \right\rangle = \left\langle \psi_{\mathrm{cav}}^{-} \middle| \psi_{\mathrm{r}} \right\rangle = \alpha, \tag{2.23}$$

revealing the same result. Here, R corresponds to the reflection on the mirror, and $R^\dagger R$ is unitary. This gives rise to the physical correspondence of the variable α: $|\alpha|^2$ corresponds to a mode matching efficiency $|\alpha|^2 = \varepsilon_1$, characterizing the match between, e.g., a fiber mode and cavity mode. Utilizing these identities, P_{out} is simplified to

$$P_{\mathrm{out}} = \mathcal{E}_{\mathrm{in}}^2 \left(1 - \varepsilon_1\right) + \mathcal{E}_{\mathrm{in}}^2 \left(\varepsilon_1 (1 - 2\xi + \xi^2) \right), \tag{2.24}$$

with the definition of ξ as given in Eq. 2.16. Alongside the presented approach [64–66] this results in a Lorentzian-shaped dip, compare Fig. 2.5c:

$$\frac{P_{\mathrm{out}}}{P_{\mathrm{in}}} = 1 - \eta_{\mathrm{dip}} \frac{1}{1+\nu^2}, \tag{2.25}$$

where a Taylor series expansion was applied around the ν_{cav} and $\nu = (\nu_{\mathrm{laser}} - \nu_{\mathrm{cav}})/\kappa$ with cavity decay rate $\kappa = \Delta\nu_{\mathrm{FWHM}}/2$. Here, η_{dip} is defined via

$$\eta_{\mathrm{dip}} = \varepsilon_1 \left(1 - |1 - \xi(0)|^2\right) = \varepsilon_1 \eta_{\mathrm{imp}}. \tag{2.26}$$

Fiber-Coupled Cavities Considering fiber-coupled cavities, the outcoupled electric field undergoes an additional filtering procedure: Only light that matches the fiber properties is guided and thus contributes to the reflection spectrum. Mathematically, the overlap integral of the outcoupled light with the fiber mode has to be applied:

$$E_{\mathrm{out}}(\Delta\nu) = \left(\left\langle \psi_{\mathrm{f}}^{-} \right| E_{\mathrm{r}} + \left\langle \psi_{\mathrm{f}}^{-} \right| E_{\mathrm{leak}}(\Delta\nu) \right) \left| \psi_{\mathrm{f}}^{-} \right\rangle . \tag{2.27}$$

Inserting the formulas found for E_{r} and E_{leak} and expressing the overlap integral of the fiber guided mode and the reflected mode as $\left\langle \psi_{\mathrm{f}}^{-} | \psi_{\mathrm{r}} \right\rangle = \beta$ leads to

$$P_{\mathrm{out}}(\Delta\nu) = E_{\mathrm{out}}^{\dagger}(\Delta\nu) E_{\mathrm{out}}(\Delta\nu) \tag{2.28}$$

$$= \mathcal{E}_{\mathrm{in}}^2 \left| \beta - \alpha^2 \xi(\Delta\nu) \right| . \tag{2.29}$$

A further simplification step involves the representation of the found expression in accordance with the one found in Eq. 2.24 and the application of a Taylor series expansion following [64, 65]. This results in

$$\frac{P_{\mathrm{out}}(\nu)}{P_{\mathrm{in}}} = \eta_{\mathrm{r}} - \eta_{\mathcal{L}} \left(\frac{1}{1+\nu^2} - \mathcal{A} \frac{\nu}{1+\nu^2} \right). \tag{2.30}$$

Here, the origin of the asymmetric lineshape becomes obvious: While in the free-space scenario, the ratio is made up of a single Lorentzian-shaped dip, the fiber-based case features an additional dispersive contribution. The power ratio's baseline is set by the amplitude of the reflection η_{r}. The Lorentzian profile exhibits an amplitude $\eta_{\mathcal{L}}$ and the dispersive curve exhibits an amplitude $\mathcal{A}$. Among other things, the minima of the reflected power do not coincide anymore with the mode-matched case, compare Fig. 2.5d. For a detailed description, including the determination of $\eta_{\mathcal{L}}$ and $\mathcal{A}$ refer to [64, 65].

2.2 Fundamentals of Cavity Optomechanics

In the field of optomechanics the interaction between a radiative field and a mechanical oscillator is investigated. The interaction is based on the radiation pressure: Photons of the radiative field each carry a momentum of $p = h/\lambda$, with the Planck constant h and the wavelength of the photon λ. The momentum can be transferred to the mechanical system. In the following, we will refer to the radiative field as optical field for the sake of clarity. Nevertheless, the very first experiments on this topic have shown that the same principles hold true for the microwave regime.

The following description is based on the explanation given in [33]. An optical mode (described by $\hat{a}$) and a mechanical mode ($\hat{b}$) are represented as harmonic oscillators, compare the scheme depicted in Fig. 2.6. The mechanical mode's frequency Ω_m and the optical mode's resonance frequency ω_cav are linked via the Hamiltonian

$$\hat{H}_0 = \hbar\omega_\mathrm{cav}\hat{a}^\dagger\hat{a} + \hbar\Omega_\mathrm{m}\hat{b}^\dagger\hat{b}, \tag{2.31}$$

describing the pure oscillation of the radiative and the mechanical mode. The mechanical mode is characterized by the mechanical quality factor $Q = \frac{\Omega_\mathrm{m}}{\Delta\Omega_\mathrm{FWHM}}$ with $\Delta\Omega_\mathrm{FWHM}$ representing the full width at half maximum. If the description is to include losses, the mechanical system exhibits a mechanical damping rate called Γ, and for the radiative field, the overall cavity intensity decay rate is named κ. The resonance frequency of the optical field depends on the position of the movable mirror, which means that ω_cav is a function of the mirror displacement x:

$$\omega_\mathrm{cav}(x) = \omega_\mathrm{cav} + x\partial\omega_\mathrm{cav}/\partial x + \dots . \tag{2.32}$$

For most applications, where there are only small displacements, it is sufficient to continue with

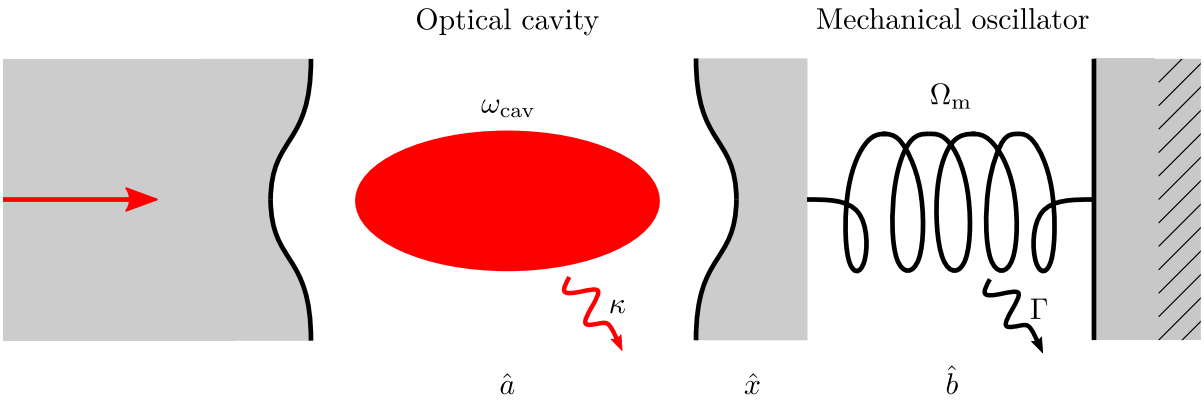

Figure 2.6: Schematic setup resembling the mirror on a spring configuration. Radiative field and mechanical mode are inherently coupled via radiation pressure due to the suspension of one cavity mirror on a spring. This setup allows for the interaction of a photon of the radiative field with a phonon of the mechanical mode and vice versa.

the linear term and omit higher terms. The so-called frequency-pull paramter $G^{(1)}$ is defined via

$$G^{(1)} = -\partial\omega_{\mathrm{cav}}/\partial x = \omega_{\mathrm{cav}}/L \tag{2.33}$$

and describes the shift of the resonance frequency of the optical field per displacement of the mirror.[1] The parameter L corresponds to the total length of the optical cavity. Including this parametric dependence, the contribution of the radiative mode in the Hamiltonian can be rewritten as

$$\hbar\omega_{\mathrm{cav}}(x)\hat{a}^\dagger\hat{a} \approx \hbar(\omega_{\mathrm{cav}} - G^{(1)}\hat{x})\hat{a}^\dagger\hat{a}. \tag{2.34}$$

The displacement x of the mirror can be reformulated as an expression of the phonon operator $\hat{b}$ as $\hat{x} = x_{\mathrm{ZPM}}(\hat{b} + \hat{b}^\dagger)$, with

$$x_{\mathrm{ZPM}} = \sqrt{\frac{\hbar}{2m_{\mathrm{eff}}\Omega_{\mathrm{m}}}} \tag{2.35}$$

being the so-called zero-point motion (to be more precise, the mechanical zero-point fluctuation amplitude). Here, m_{eff} denotes the effective mass that is subject to the oscillations. Equation 2.35 leads to an important figure of merit for the optomechanical system, the vacuum optomechanical single-photon coupling strength

$$g_0 = G^{(1)}x_{\mathrm{ZPM}}. \tag{2.36}$$

The value of g_0 describes the frequency shift per displacement x_{ZPM}. With this, an interaction part for the Hamiltonian can be formulated as

$$\hat{H}_{\mathrm{int}} = -\hbar g_0\hat{a}^\dagger\hat{a}(\hat{b} + \hat{b}^\dagger). \tag{2.37}$$

The force due to radiation pressure can be expressed as

$$\hat{F} = -\frac{d\hat{H}_{\mathrm{int}}}{d\hat{x}} = \hbar G^{(1)}\hat{a}^\dagger\hat{a} = \hbar\frac{g_0}{x_{\mathrm{ZPM}}}\hat{a}^\dagger\hat{a}. \tag{2.38}$$

The total Hamiltonian reads

$$\hat{H} = \hat{H}_0 + \hat{H}_{\mathrm{int}} = \hbar\omega_{\mathrm{cav}}\hat{a}^\dagger\hat{a} + \hbar\Omega_{\mathrm{m}}\hat{b}^\dagger\hat{b} - \hbar g_0\hat{a}^\dagger\hat{a}(\hat{b} + \hat{b}^\dagger). \tag{2.39}$$

In typical experiments, the vacuum optomechanical single-photon coupling strength is much smaller than the intrinsic losses of the cavity. Therefore, a cavity is populated with many photons to observe coupling contributions. From the theoretical point of view, this can be expressed as a linearization of the Hamiltonian [68]. Thus, the photon operator $\hat{a}$ is split up via $\hat{a} = \bar{\alpha} + \delta\hat{a}$, where $\bar{\alpha} = \sqrt{n_{\mathrm{cav}}}$ links to the mean photon number in the cavity n_{cav} and $\delta\hat{a}$ describes small

[1] Alongside to the definition of $G^{(1)}$, the second order frequency-pull parameter $G^{(2)}$ follows as $G^{(2)} = -\partial^2\omega_{\mathrm{cav}}/\partial x^2$ and defines the second order coupling strength per $g_0^{(2)} = \frac{1}{2}G^{(2)}x_{\mathrm{ZPM}}^2$.

fluctuations around that. The interaction term of the Hamiltonian can be expressed as

$$\hat{H}_{\text{int}} = -\hbar g_0 \hat{a}^\dagger \hat{a}(\hat{b} + \hat{b}^\dagger) \tag{2.40}$$

$$= -\hbar g_0 (\bar{\alpha} + \delta\hat{a})^\dagger (\bar{\alpha} + \delta\hat{a})(\hat{b} + \hat{b}^\dagger) \tag{2.41}$$

$$= -\hbar g_0 (|\bar{\alpha}|^2 + \bar{\alpha}^\dagger \delta\hat{a} + \bar{\alpha}\delta\hat{a}^\dagger + \delta\hat{a}^\dagger\delta\hat{a})(\hat{b} + \hat{b}^\dagger). \tag{2.42}$$

The resulting term including $\delta\hat{a}^\dagger\delta\hat{a}$ is omitted in the following since it is smaller by a factor of $|\bar{\alpha}|$ compared to the others. The term proportional to $|\bar{\alpha}|^2$ describes a general offset: This can be explained with the presence of an average radiation force $\bar{F} = \hbar G|\bar{\alpha}|^2$. It is possible to omit this term as well by shifting the reference frame to the origin of the resulting displacement

$$\delta\bar{x} = \frac{\bar{F}}{m_{\text{eff}}\Omega_{\text{m}}^2}. \tag{2.43}$$

The resulting interaction Hamiltonian reads as

$$\hat{H}_{\text{int, linear}} = -\hbar g_0 \sqrt{n_{\text{cav}}}(\delta\hat{a} + \delta\hat{a}^\dagger)(\hat{b} + \hat{b}^\dagger). \tag{2.44}$$

This is the linearized Hamiltonian as it is linear in $\delta\hat{a}$ and $\hat{b}$. Even though large photon numbers motivated the derivation, it still holds true if n_{cav} is not excessively large [33].

2.2.1 Optical Spring Effect

As presented above, the radiative field interacts with the mechanical motion. While the previous consideration just targeted the determination of this interaction, it can likewise be used to tune the mechanical response. To stay with the image of a mirror on a spring, this corresponds to a change in the spring constant D_0. The so-called optical spring effect describes an induced damping or amplification of the mechanical motion and a shift in frequency [33, 69–71]. The change of the spring constant is driven by the impinging radiation pressure force via

$$D = D_0 - \frac{\mathrm{d}F}{\mathrm{d}x}. \tag{2.45}$$

Typically, the damping or amplification can be observed in the sideband-resolved regime[2] [26, 33], while for our experimental case, solely the resonance shift is observed. In the corresponding systems, the change in mechanical response can be utilized further: Depending on the detuning of the impinging radiative field with respect to the mechanical mode, either a cooling or a heating (amplification) effect of the mechanical motion can be realized [25, 72, 73]. In a simplified picture, this can be understood as follows: To fit the cavity resonance, the impinging laser is missing energy if its frequency is lower than the cavity's frequency. This energy is taken from the mechanical mode, which is therefore cooled. In reverse, if the laser's frequency is larger than the cavity's, the excess energy is transferred to the mechanical mode. A scheme concerning the heating/cooling of the mechanical motion is presented in Fig. 2.7a and 2.7b, respectively.

[2] In the resolved sideband regime, the mechanical resonance frequency Ω_{m} surpasses the decay rate κ of the cavity [28].

The presented optical cooling allows for the preparation of a system to the ground state and thus enables sophisticated measurements without the need for a full cryogenic system [70].

a) $\omega_{\mathrm{cav}} - \omega_{\mathrm{laser}} < 0$

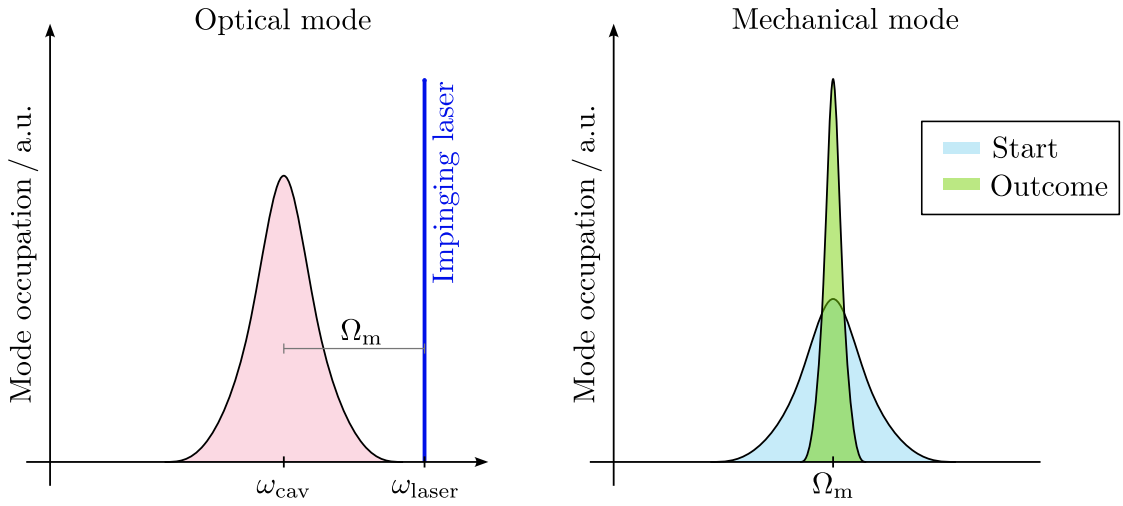

b) $\omega_{\mathrm{cav}} - \omega_{\mathrm{laser}} > 0$

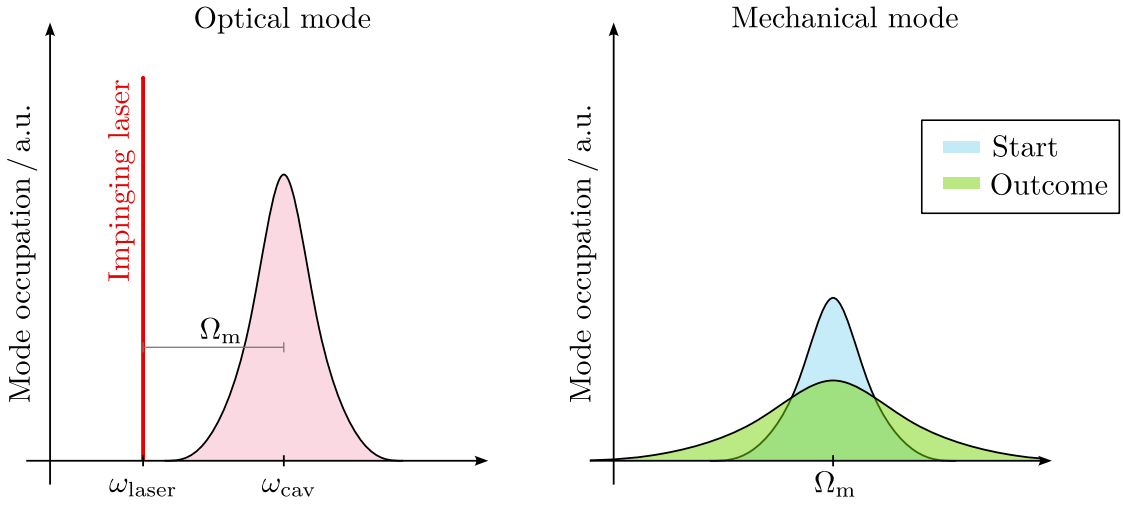

Figure 2.7: Schematic representation of the a) heating and b) cooling effect that can be obtained by the optical spring effect and be observed in sideband-resolved systems. Depending on the detuning of the impinging laser with respect to the cavity mode, energy is either added to or extracted from the mechanical system, resulting in an amplification/cooling process of the mechanical membrane, respectively.

2.3 Membrane-in-the-Middle System

A special kind of optomechanical system is posed by a so-called membrane-in-the-middle (MIM) system. In contrast to the aforementioned mirror on a spring scheme, the mechanical and optical functionalities are no longer interrelated [71, 74–76]: A dielectric membrane is inserted into the cavity formed by two stationary mirrors. The membrane itself can oscillate and features a different refractive index than the free space in the cavity. The reflection of the membrane's surface is negligible so that the cavity mode penetrates through the dielectric. Depending on the position of nodes of the electromagnetic wave inside the cavity with respect to the dielectric material boundaries, the coupling between mechanical motion and radiative field varies. Thus, in a MIM system, not the geometrical length of the cavity but the effective optical path length is modulated by the oscillations.[3]
In the following, we want to determine the effect that a membrane inside a resonator yields. We first find an expression for the fields in the setup that can be parameterized depending on the shift of the membrane along the cavity axis. Later, a perturbative method is applied to calculate the effect on the optomechanical coupling strength by analyzing the displacement of the medium.
Based on the description given in [66, 77], the electric field $\mathbf{E}$ and the magnetic field $\mathbf{H}$ can be expressed via a vector potential $\mathbf{A}$, assuming a source-free setting:

$$\mathbf{E}(\mathbf{r}) = -\frac{\partial}{\partial t}\mathbf{A}(\mathbf{r}) \tag{2.46}$$

$$\mathbf{H}(\mathbf{r}) = \frac{1}{\mu}\nabla \times \mathbf{A}(\mathbf{r}). \tag{2.47}$$

When a cavity is driven at resonance, a standing wave pattern inside the cavity builds up. Here, the polarization axis is chosen arbitrarily along the x-axis, which reduces the spatial dependence to one axis. The following derivation is based on several additional assumptions. Firstly, the cavity mode waist needs to be much smaller in size than the oscillating membrane. This ensures a uniform displacement of the material in the region of interest. Thus, any bending of the membrane is omitted in this ansatz.
The derivation further comprises a plane-wave assumption. Thus, any Gaussian beam characteristics describing the cavity mode are omitted. In consequence, the Rayleigh length of the present Gaussian mode should be comparably large to the cavity length L.
Lastly, the mirror properties should ensure that the cavity length purely depends on the physical geometry. Thus, the mirrors are assumed to be non-dispersive.
The vector potential can then be split into three parts, describing the potential on the left, inside,

[3] In conventional MIM systems, the thickness of the membrane is much smaller than λ. Hence, in these systems the approach differs from the one presented here: For thin membranes, the resulting effect is derived from a phaseshift and a change in transmission.

and on the right of the membrane.

$$\mathbf{A}(x,t) = \begin{cases} a_{\mathrm{L}}(t)\exp(\imath k_0 x) + b_{\mathrm{L}}(t)\exp(-\imath k_0 x) & \text{for } L_1 \leq x < 0 \\ a_{\mathrm{M}}(t)\exp(\imath k x) + b_{\mathrm{M}}(t)\exp(-\imath k x) & \text{for } 0 \leq x \leq d \\ a_{\mathrm{R}}(t)\exp(\imath k_0 x) + b_{\mathrm{R}}(t)\exp(-\imath k_0 x) & \text{for } d < x \leq d + L_2, \end{cases} \tag{2.48}$$

where the x-axis is chosen as the cavity axis. The time dependence is included in $a_i(t), b_i(t)$ but can be expanded as $\exp(-\imath\omega t)$. The membrane is sitting at $x = 0$ with its left surface and extending to $x = x_0$, the thickness d of the dielectric corresponds to $d = x_0$. The left mirror is sitting at $x = x_1$ and the right mirror at $x = x_2$, which means the total cavity length L is given by $L = L_1 + d + L_2$, with $L_1 = |x_1|$ and the height of the membrane above the mirror (the height of the membrane's feet) $L_2 = x_2$. For the definition of the geometry compare Fig. 2.8.

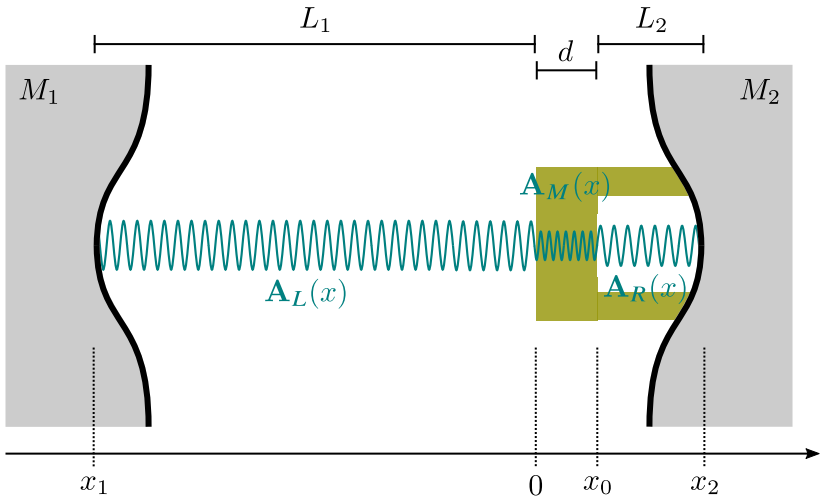

Figure 2.8: Schematic representation of a MIM setup. The membrane comprises a different refractive index compared to its surrounding. The underlying ansatz assumes a uniform displacement of the membrane in x-direction, with the cavity mode being much smaller than the membrane size. Reflections occurring at the boundaries of the surfaces are neglected. Compare [66].

The boundary conditions of the electric and magnetic field are applied: Since the mirrors are formed by conductive surfaces[4], the electric field needs to vanish on top of the surface. For the transition between dielectric media, both, the electric and the magnetic field, have to be continuous at the surface of the membrane. This results in the conditions

$$\frac{\partial}{\partial t}\mathbf{A}_L(x_1,t) = 0 \tag{2.49}$$

$$\frac{\partial}{\partial t}\mathbf{A}_R(x_2,t) = 0 \tag{2.50}$$

[4] The penetration depth of a DBR substrate is neglected in this derivation.

$$\frac{\partial}{\partial t}\mathbf{A}_L(x=0,t) = \frac{\partial}{\partial t}\mathbf{A}_M(x=0,t) \tag{2.51}$$

$$\frac{\partial}{\partial t}\mathbf{A}_M(x=x_0,t) = \frac{\partial}{\partial t}\mathbf{A}_R(x=x_0,t) \tag{2.52}$$

$$\frac{\partial}{\partial x}\mathbf{A}_L(x,t)\Big|_{x=0} = \frac{\partial}{\partial x}\mathbf{A}_M(x,t)\Big|_{x=0} \tag{2.53}$$

$$\frac{\partial}{\partial x}\mathbf{A}_M(x,t)\Big|_{x=x_0} = \frac{\partial}{\partial x}\mathbf{A}_R(x,t)\Big|_{x=x_0}. \tag{2.54}$$

Inserting these into Eq. 2.48 results in a lengthy calculation. The full calculation was performed by [66] and results in the condition

$$S_{\mathrm{MIM}}(L_1,L_2,d) = A_+(L_1)\exp(-\imath n k_0 d) - A_-(L_2)\exp(-\imath n k_0 d). \tag{2.55}$$

This term $S_{\mathrm{MIM}}(L_1,L_2,d)$ is required to be equal to zero for a resonant setup. The parameter $A\pm$ is defined via

$$A_\pm(L_i) = \frac{1 \mp \imath n \tan(k_0 L_i)}{1 \pm \imath n \tan(k_0 L_i)} \tag{2.56}$$

and L_i from (L_1, L_2). Fixing one of the three parameters, the expression can be presented in two dimensions. Figure 2.9 depicts the absolute value of S_{MIM} for a fixed membrane thickness of $d = 1.5\,\mu\mathrm{m}$ in dependence on L_1 and L_2, each normalized with the wavelength $\lambda = 780\,\mathrm{nm}$. The red lines mark the parameter combinations where $S_{\mathrm{MIM}} = 0$ so that the resonance condition is fulfilled.

2.3.1 Optomechanical Coupling Strength

Next, the optomechanical coupling strength shall be derived. As found in Sec. 2.2, the vacuum optomechanical coupling strength g_0 serves as a figure of merit for optomechanical systems. From finite element simulations, various properties of the mechanical mode are retrieved numerically, such as the mechanical eigenfrequency, the effective mass of the mode, and, in consequence, the zero-point motion. Hence, the frequency-pull parameter $G^{(1)}$ is the missing link to determine g_0.
Two methods for computing the value of $G^{(1)}$ will be briefly discussed. The first method considers a slight shift of the geometric properties. The parameter $G^{(1)}$ can then be determined from the effect on the aforementioned equations. The second method is based on perturbation theory and the effect on Maxwell's equations at the boundaries of the membrane.

Shifting the Boundaries of the Membrane The motion of the membrane results in a shift of the resonance frequency of the radiative field, as determined by Eq. 2.32. In the following, this shift of frequency is exploited. The membrane is assumed to move according to its fundamental mechanical mode. This implies a constant thickness of the membrane $d = \mathrm{const.}$, while the distances from the membrane's surfaces to the mirrors' surfaces are modulated. This modulation

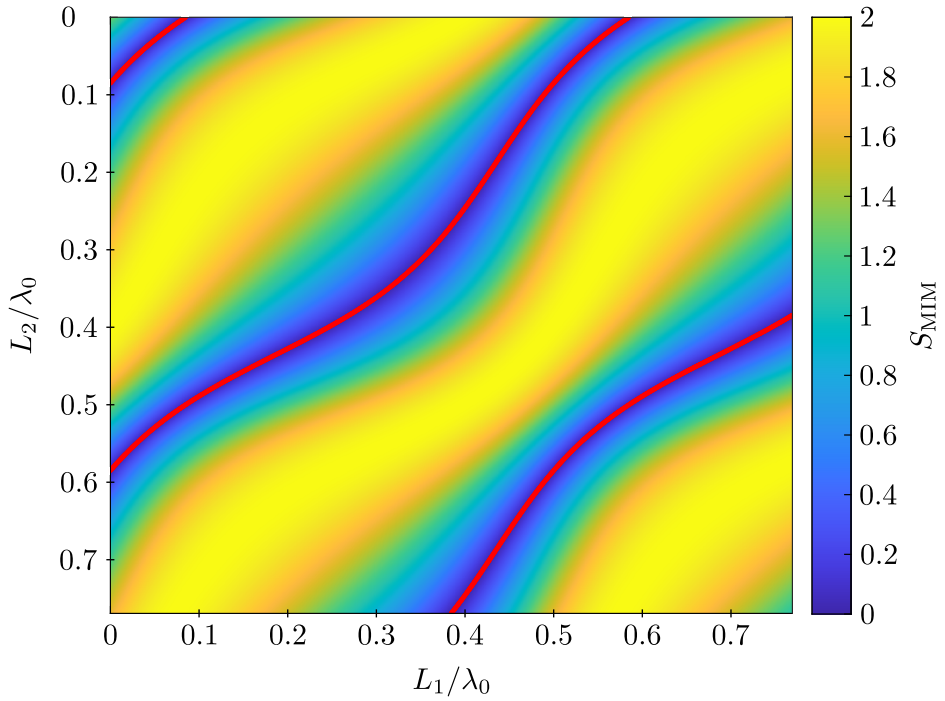

Figure 2.9: Graphical representation of the condition emerging from Eq. 2.55. For this graph, the membrane thickness is fixed to $d = 1.5\,\mu\mathrm{m}$. The red lines denote the parameter combinations of L_1 and L_2 that fulfill the resonance condition S_{MIM} and thus provide a resonant cavity. Both axes are normalized by the wavelength $\lambda_0 = 780\,\mathrm{nm}$.

is performed symmetrically. If denoted by a length shift ΔL, it can be expressed by the transitions

$$L_1 \rightarrow L_1 + \Delta L \tag{2.57}$$

$$L_2 \rightarrow L_2 - \Delta L. \tag{2.58}$$

When inserted in Eq. 2.55, the shift Δk on the wavenumber $k_0 \rightarrow k_0 + \Delta k$ can be extracted. This angular wavenumber is transferred to an angular frequency shift $\Delta\omega_{\mathrm{cav}}$, which allows the determination of $G^{(1)}$ as

$$G^{(1)} = \frac{\Delta\omega_{\mathrm{cav}}}{\Delta L}. \tag{2.59}$$

The quadratic coupling parameter $G^{(2)}$ can be retrieved from the calculations as derivative of $G^{(1)}$ with respect to x. As a result, the quadratic coupling reaches an extreme value when $G^{(1)} = 0$. The Hamiltonian can thus be reduced to the quadratic coupling term (if the fast oscillating terms are dropped again by changing the reference system)

$$H_{\mathrm{int}} = \hbar g_0^{(2)} (\hat{b} + \hat{b}^\dagger)^2 \hat{a}\hat{a}^\dagger \tag{2.60}$$

so that H_{int} is directly proportional to the phonon number $n_{\mathrm{Phonon}} = \hat{b}^\dagger \hat{b}$ [33, 66].

If the aforementioned assumptions are fulfilled, the presented approach allows to derive the coupling strength. The retrieved value is consistent with a more elaborate approach, including an ansatz emerging from perturbation theory. This perturbation approach will be investigated in the following since it provides additional insight into the behavior of $G^{(1)}$.

Perturbation Theory Approach Perturbation theory serves as a method to provide solutions if a setting with an already known solution undergoes small changes. The following derivation is once again based on the assumptions that were made previously in Sec. 2.3. According to the approach given in [78], the present system can be described by the wave-equation, which represents an eigenproblem of the electric field $|E\rangle$:

$$\nabla \times \nabla \times \mathbf{E} = \left(\frac{\omega}{c}\right)^2 \epsilon \, |E\rangle \, . \tag{2.61}$$

In the Dirac notation, the inner product is defined via $\langle E|E'\rangle = \int \mathbf{E}^* \mathbf{E}' \mathrm{d}V$. When introducing the perturbation in the form of a slight spatial shift Δx of the dielectric, resulting in a shift $\Delta\epsilon$ in permittivity, it holds

$$|E\rangle = \sum_{n=0}^{\infty} \left|E^{(n)}\right\rangle = \left|E^{(0)}\right\rangle + \left|E^{(1)}\right\rangle + O(\Delta x^2) \tag{2.62}$$

$$\omega_{\mathrm{cav}} = \sum_{n=0}^{\infty} \omega_{\mathrm{cav}}^{(n)} = \omega_{\mathrm{cav}}^{(0)} + \omega_{\mathrm{cav}}^{(1)} + O(\Delta x^2) \tag{2.63}$$

for the eigensolutions. Inserting those into the initial eigensolution with respect to the condition $\left\langle E^{(0)}\right| \epsilon \left|E^{(i)}\right\rangle = 0$ with $i \neq 0$, it follows

$$\omega_{\mathrm{cav}}^{(1)} = -\frac{\omega_{\mathrm{cav}}^{(0)}}{2} \frac{\left\langle E^{(0)}\right| \Delta\epsilon \left|E^{(0)}\right\rangle}{\left\langle E^{(0)}\right| \epsilon \left|E^{(0)}\right\rangle}. \tag{2.64}$$

In its differential form, this can be expressed as

$$G^{(1)} = \frac{\mathrm{d}\omega_{\mathrm{cav}}}{\mathrm{d}x} = -\frac{\omega_{\mathrm{cav}}^{(0)}}{2} \frac{\left\langle E^{(0)}\right| \frac{\mathrm{d}\epsilon}{\mathrm{d}x} \left|E^{(0)}\right\rangle}{\left\langle E^{(0)}\right| \epsilon \left|E^{(0)}\right\rangle}. \tag{2.65}$$

The permittivity $\epsilon(x)$ can be replicated by the formula

$$\epsilon(x) = \epsilon_2 + [\epsilon_1 - \epsilon_2](\Theta(x - x_0) - \Theta(x - (x_0 - d)) \tag{2.66}$$

with the permittivity ϵ_1 of the dielectric medium and permittivity ϵ_2 of air and the Heaviside step function Θ. The derivative of the step function is the delta function $\delta(x)$.

A series of transformations (compare [66, 78]) results in the expression

$$G^{(1)} = \frac{\mathrm{d}\omega_{\mathrm{cav}}}{\mathrm{d}x} = \frac{\mathrm{d}\omega_{\mathrm{cav}}^{(0)}}{2} \frac{\int_{\mathcal{S}_R} \mathrm{d}\mathcal{S} \left(1 - \frac{\mathrm{d}(x_0+d)}{\mathrm{d}x}\right) \Delta\epsilon \left|E_{\parallel}^{(0)}\right|^2 - \int_{\mathcal{S}_L} \mathrm{d}\mathcal{S} \left(1 - \frac{\mathrm{d}x_0}{\mathrm{d}x}\right) \Delta\epsilon \left|E_{\parallel}^{(0)}\right|^2}{\int_V \mathrm{d}V \epsilon(x) \left|E_{\parallel}^{(0)}\right|^2}. \quad (2.67)$$

The surface integral $\int_{\mathcal{S}_i} \mathrm{d}\mathcal{S}$ with $i = (L, R)$ corresponds to the area overlap between the membrane and the radiative mode on the left/right-hand side of the membrane, respectively. The shift in ϵ is expressed via $\Delta\epsilon = \epsilon_1 - \epsilon_2$. Figure 2.10a shows the optomechanical coupling map that results from this derivation. Here, the frequency-pull parameter reaches its maximum at $G^{(1)} = 11\,\mathrm{GHz/nm}$.

The result is identical to the result of the first approach. Nevertheless, the perturbative method adds value to the found expression since it provides a deeper insight into the behavior of $G^{(1)}$. Upon inspection of the numerator, the fundamental dependencies can be derived. Assuming a radiative mode with the same amplitude on both sides of the membrane, the terms in the numerator will cancel out each other, resulting in $G^{(1)} = 0$. Suppose the mode overlap on one side of the membrane vanishes. In that case, the numerator will obtain a maximal value: For a mode overlap equal to zero on the left-hand side of the membrane, $G^{(1)}$ reaches its maximal positive value, a mode overlap equal to zero on the right-hand side results in a negative extreme value.

This can be understood intuitively in the frame of the radiation pressure as a mediator between mechanical motion and radiative mode. In the case of equal intensities on the left and on the right-hand side of the membrane, the net force of the radiation pressure equals zero, thus there is no coupling between radiative and mechanical mode present, and $G^{(1)} = 0$. If the field is zero on one side and maximal on the other, the applied force is maximal, thus resulting in an extreme value of $G^{(1)}$. This can be seen in the graphs of Fig. 2.10b, displaying various field combinations at the interfaces of the membrane with their corresponding location in the optomechanical coupling map.

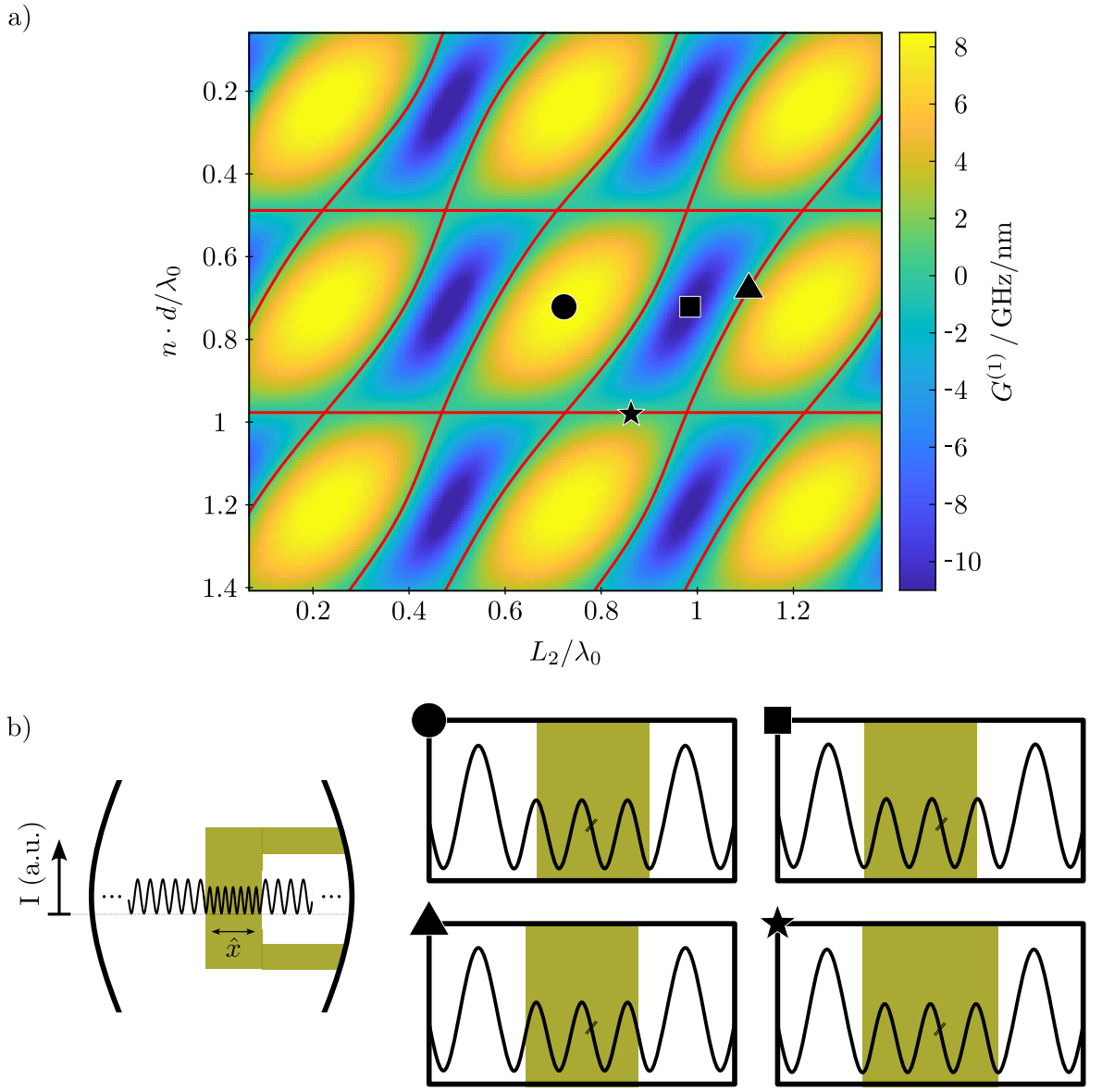

Figure 2.10: a) The linear coupling map depicting the dependence of $G^{(1)}$ with respect to d and L_2, each normalized by the wavelength $\lambda_0 = 780\,\text{nm}$. The pattern is periodic with half the material wavelength so that a modulo operation with regards to λ_0 could be performed on both axes. The not depicted parameter L_1 is chosen according to the cavity condition $S_{\text{MIM}} = 0$ from Eq. 2.55. The total length of the setup $L_{\text{total}} = L_1 + d + L_2$ is kept as constant as possible: The aforementioned cavity condition may induce slight fluctuations on L_{total}. The shape of the maximum and minimum differ due to the chosen geometry dimensions: $L_1 \approx 2 \cdot L_2$. The red lines depict scenarios where $G^{(1)} = 0$. b) The intensity distributions of some prominent configurations from the map are depicted (see ●, ■, ▲, ★). The yellowish region represents the membrane. The effect of the membrane's surface overlap with the mode, as presented by Eq. 2.67, becomes evident. While the coupling strength is reduced to zero if equal intensities on both sides are present, it reaches an extreme value for configurations where the field vanishes on one side while it is maximal on the other.

2.4 Locking Schemes

In order to determine the characteristics of the mechanical membrane in the fiber Fabry–Pérot cavity, a frequency locking mechanism is needed: This allows to filter out background movements of the cavity setup by continuously adjusting the fiber position and therefore the length of the Fabry–Pérot cavity. The mechanical oscillation of the membrane itself must remain unchanged by the locking procedure: The frequency noise, which will be filtered out, shall not lay in the order of the mechanical excitation, since this signal of interest would be filtered out as well.
The technique emerged from the intention of stabilizing a laser's frequency. Nevertheless, it can be analogously applied to control the cavity length. The initial idea is the measurement of frequency fluctuation with the help of a cavity. The reflected light from the cavity is used to determine the detuning of the laser with respect to the cavity resonance. A signal is generated and sent back to the laser to compensate for the shift. This laser tuning can be performed in several ways, e.g., by temperature controlling, by introducing an additional cavity in the laser beam path or by an acousto-optic modulator. Following this approach, the cavity is assumed to be more stable than the laser's output.
For the application in an FFPC with integrated membrane, the laser is not tuned in its frequency, but the cavity length is varied to create a stable lock, assuming the laser's frequency to be stable. In the following, two locking scheme will be reviewed qualitatively.

2.4.1 Side-of-Fringe Locking

Assume a laser coupled directly into a cavity. Figure 2.2 depicts the reflected intensity out of the cavity in dependence on the incoupling laser's frequency. When the frequency of the laser is slightly shifted, the intensity outcoupled from the cavity is affected: Assuming a lock on the blue-detuned slope with respect to the cavity resonance, an increase in intensity corresponds to the information that the frequency was shifted to lower values. Hence, the laser frequency shall be increased to return to the locking point. Vice versa, upon noticing a decrease in intensity, the laser's frequency is lowered. In the case of a locking point on the red-detuned slope, the corresponding signs for frequency tuning switch. The strongest phase-intensity dependence (the highest steepness) is typically found at half the depth of the cavity resonance. It is beneficial to choose this spot for locking due to the high intensity response. However, this comprises a loss of approximately half of the laser power that cannot be used for the experiment. In some scenarios, where high intensity is desirable, this poses a significant disadvantage of the side-of-fringe (SoF) locking mechanism.
If the reference point was tuned to the resonance of the cavity, the total laser power would be available, but slight frequency variations would yield in only minor changes of the intensity signal. Additionally, the symmetry veils the information about the sign of the shift. Hence, SoF locking does not allow for a locking on the resonance frequency of the cavity.
Furthermore, independent of the tuning point, a shift in laser frequency cannot be distinguished from possible fluctuations in the laser intensity. Thus, more elaborate schemes of this method include additional feedback loops to stabilize the laser intensity. To put it in a nutshell, SoF locking is a simple and fast locking method if the laser provides a stable output intensity and if this provided intensity is much higher than the requirements.

In the following, a procedure is presented that allows to lock a system at higher intensities due to the usage of a signal proportional to the derivative of the intensity.

2.4.2 Pound–Drever–Hall Locking

The Pound–Drever–Hall (PDH) locking scheme, first presented in 1983 [79], provides a frequency-dependent signal proportional to the derivative of the intensity. Its setup includes a device (e.g., an EOM, electro-optic modulator) to create sidebands on the laser (carrier) signal. This device is driven by a radio frequency (RF) source. The frequency detuning of the sidebands with respect to the laser frequency is typically much smaller than the free spectral range of the cavity. It is chosen so that the sidebands do not mix with the laser signal within its linewidth.
For PDH locking, the resulting cavity response signal is mixed with the signal of the harmonic oscillator signal, which serves for the input of the EOM-input. The signals are phase corrected with respect to each other due to different delay times in both paths. The resulting mixture thus contains a low-frequency part and a part at almost twice the modulation frequency. The low-frequency signal can be extracted by a filter (low-pass filter, LPF) and describes the shift of the cavity with respect to the incoming frequency: The frequencies of the sidebands are not supported by the cavity geometry if the carrier frequency is driving the cavity in resonance. In this case, the intensity at the frequencies of the sidebands is fully reflected at the entrance mirror of the cavity, while no signal of the carrier wave is reflected. Due to heterodyne mixing with the RF source signal, a signal at the sideband frequency is generated. In the resonant case, the two sideband mixtures inhibit a phase difference of exactly π, so they cancel out each other. If the carrier frequency (or the cavity geometry) undergoes a slight shift, the intensity at the carrier frequency can be measured. In addition, the mixed signal contains a contribution at the sideband frequency as their relative phase shift is not equal to π. The amplitude of this signal is then used for the correction of the setup: It is fed to the piezo controller driving the cavity length for stabilization of the cavity response.
For a quantitative evaluation and further reading, refer to [80–82], which includes the mathematical description of the scheme.

CHAPTER 3

Fabrication via Direct Laser Writing

For the fabrication of three-dimensional structures, a wide variety of procedures exist. While some of these methods allow for easy and fast mass production, such as injection molding, others may provide unique pieces for a specific application. The latter methods experienced strong growth over the last decade in both, industry and even household applications. What they all have in common is a microchip-controlled production of the pieces. These methods can be further subdivided on the one hand into subtractive manufacturing procedures, for example, water jet cutting or computerized numerical control (CNC) milling, which are most widely used for metal and wood processing. On the other hand, additive manufacturing procedures pile up material at designated places and hence allow for almost arbitrary three-dimensional models: Sintering provides a method to fabricate workpieces from durable and strong materials such as metal, glass, ceramic, and polymers. Selective laser sintering (SLS) even allows for the inclusion of detailed inner parts in the geometry.
The number of 3D printers that can nowadays be found in households strongly increasing over the last years. Here, fused deposition modeling (FDM) printers pose a wide-spread type [83]. A string of material is inserted into a so-called hotend. This hotend, depending on the printing material, heats up to a temperature of around 220 °C. The machines are usually equipped with a heatbed, which is heated to around 60 °C during printing. This improves the print adhesion to the bed and preserves the printed structure from buckling up due to a high temperature difference between freshly printed material and already deposited material. The hotend can move relative to the heatbed in x- and z-direction, while the bed typically travels in y-direction. This allows the print of arbitrary geometries. A wide variety of polymeric materials can be used with these machines if their hardware supports the appropriate temperature regions: Polylactic acid (PLA), polyethylenterephthalat (PET), and acrylnitrit-butadien-styrol-copolymere (ABS) are the most common ones, but some machines also allow for nylon, wood filament, and metal filament [84]. The names of wood filament and metal filament are misleading: These filaments are based mostly on PLA or ABS and incorporate fine wood/metal debris. The print has thus the appeal of a wooden or metal object, but its mechanical and/or electrical properties differ. Nevertheless, not every FDM printer can cope with these filaments due to the debris that might cause clogging.
Furthermore, another type of machine for additive manufacturing can be found in private households: Stereolithography printers (SLA, stereolithography apparatus) provide much higher

resolutions in comparison to FDM-based printers [85, 86]. Here, the print material is a liquid resin, which is filled in a tank. The printbed is mounted upside down and can be driven by a motor into the resin tank. On the bottom, the tank features a transparent window. Depending on the type of apparatus, the resin is now polymerized either a) by a laser, which can be moved by a galvanometer scanner controlled (galvo) mirror (Laser SLA), or b) by a projector (DLP-SLA, digital light processing SLA) or c) by a liquid crystal display (LCD) (MSLA, masked SLA). The latter is the most common method for affordable at-home SLA printers. By selectively illuminating each layer, the three-dimensional model builds up over time. MSLA machines also have the unique property that larger print cross sections do not increase the overall printing time: It does not affect the time whether the LCD illuminates the resin only in a minimal area or over the whole display. Only the height, the direction perpendicular to the display, is relevant for the printing time when comparing the same print parameters. The resins used for SLA are most commonly UV-resins, which polymerize at a wavelength of 405 nm.
Here, we utilize a fabrication procedure that involves direct laser writing (DLW). The first impression might suggest that there are several analogies to the principle of the aforementioned SLA printers. When the term direct laser writing came up in the 1980s, it was presented as a method to pattern a structure onto a sample [87]. In that case, a positive tone photoresist is spin-coated onto a substrate. A laser beam is focused into the resist while the sample is moved on a computer-controlled stage. These first realizations were solely based on the principle of one-photon absorption (OPA) and hence use a HeCd ($\lambda = 442\,\mathrm{nm}$) for the illumination [87–89]. This allows only for patterning in two dimensions or in 2.5 dimensions if applied layerwise.
In the second half of the 1990s, the approach of photo lithography making use of two-photon absorption (TPA) comes up [45]. This allows to overcome the low resolution in beam direction and enables to truly 3D-print arbitrary structures in a photoresist, not limited by underlying layers. In the following, the process of TPA is reviewed in detail.

3.1 Two-Photon Absorption

In the case of OPA, a linear photoresist is polymerized by a laser of fitting wavelength. It is limited to structures without overhangs since all the molecules in the beampath undergo a polymerization process. Thus, the structures are limited to 2.5 dimensions.
TPA processes offer a high lateral and, in particular, a high axial resolution. Here, a laser source at double the wavelength of the resin-specific wavelength is strongly focused into the resist. A high field strength at the focal spot is necessary to trigger the polymerization process. This is achieved by the strong focusing and the utilized pulsed femtosecond laser source[1]. Relative to the neighboring molecules, those in the focal spot have an increased probability of absorbing two photons at once, therefore beating the polymerization threshold. A crucial point for achieving a high resolution is the choice of photoresist. Typically, the polymerization procedures are triggered at an energy corresponding to a UV-photon [91]. A laser source for TPA is located in the near-infrared (NIR) regime. The linear absorption of NIR-light is insignificant for a typical UV-resist, which allows for a high-resolution process. Figure 3.1a and 3.1b show two

[1] Nevertheless, it has been shown that TPA processes for direct laser writing can also be triggered by a continuous wave laser [90].

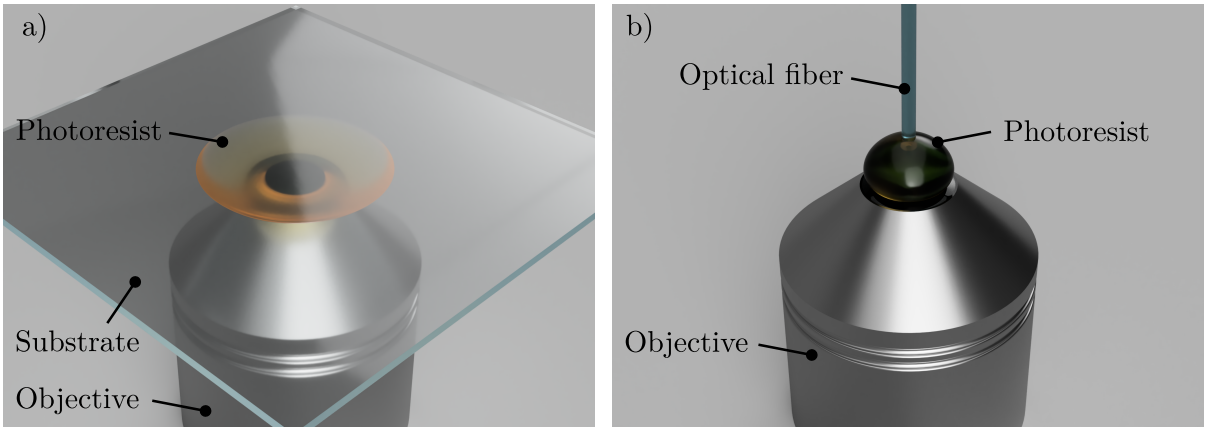

Figure 3.1: Configurations of the DLW system. a) Depicted is the dip-in configuration used for the printing on a substrate. A droplet of photoresist is cast on the substrate, which is subsequently mounted upside down in the machine. The objective then approaches the substrate and is covered with the resist as well, reducing the number of transitions between media. b) Instead of a flat substrate, a custom holder enables the print on the endfacet of a fiber. In this case, the automatic interface finding has to be omitted and replaced by a manual procedure.

configurations for DLW. The resist is in direct contact with the objective, which represents the so-called dip-in configuration. The photoresist simultaneously serves as immersion medium, hence a high numerical aperture can be obtained, resulting in a strongly focused laser spot. In addition, aberrations due to refraction at the interfaces of different media are avoided. While the system is designed to use a flat substrate as a basis for fabrication, it is possible to print on various different surfaces as well, including optical fibers, as depicted in Fig. 3.1b. Here, adaptations to the system have to be made, e.g., for the mounting of the optical fiber in the machine. In addition, automatic systems, like the interface-finding algorithms, do not work anymore due to the reduced surface area of fibers compared to an extended glass substrate. It should be noted that the depicted dip-in-configurations are not the only options for the fabrication of polymeric structures with the system. The photoresist can also be applied on the substrate's side facing upwards. Depending on the objective used, either immersion oil is applied between the objective and the substrate or no immersion medium is necessary at all. However, in both cases, the laser has to travel through air/immersion oil and substrate before entering the photoresist. This leads to additional refractions and reflections at the interfaces. Therefore, the typical achievable resolution with those methods is lower.

The first applications of the DLW technique were driven by the idea of producing large photonic crystals from a dielectric material [47, 48]. Before this technique was known, producing such crystals was demanding manual labor involving holographic lithography and stacking layer by layer. Since this takes much time and is labile, those crystals were made of only a few layers. DLW provides an alternative fabrication method that allows hassle-free scaling up of the crystals. The minimal size of the volume cell that polymerizes (called voxel, for volume element, in accordance with the term pixel for two-dimensional characterization, composition from "picture" and "element") depends on the iso-surfaces of the objective used, the deposited dose, and the polymerization threshold of the resist [48].

Following the derivation given in [91], the polarization of a material is expressed in terms of the electric field E and the susceptibility χ via

$$P = \chi^{(1)}E + \chi^{(2)}E^2 + \chi^{(3)}E^3 + \chi^{(4)}E^4 + \chi^{(5)}E^5 + \dots, \tag{3.1}$$

where $\chi^{(x)}$ is a tensor and corresponds to the x-th order optical susceptibility. Assuming a resonant process, the even order susceptibilities vanish [92]. With $\chi^{(1)}$ representing a linear process, the nonlinear process is covered by $\chi^{(3)}$, $\chi^{(5)}$, and higher orders. Their imaginary parts represent the losses in the material. The energy exchange between light and matter is composed of the electric field and the polarisation via

$$\frac{\mathrm{d}W}{\mathrm{d}t} = \left\langle \vec{E} \cdot \dot{\vec{P}} \right\rangle \tag{3.2}$$

$$= \frac{8\pi\omega}{c^2 n^2} I^2 \mathrm{Im}\left[\chi^{(3)}\right]. \tag{3.3}$$

In contrast to the resist used in OPA (where the exposure dose is linear to the number of photons that pass a molecule, given by $\chi^{(1)}$), in TPA, the polymerization rate depends quadratically on the light intensity I. Due to its dependence on $\chi^{(3)}$, TPA is a third-order process. As elaborated in [91], the cross section for the TPA can be derived, which is given by

$$\delta = \text{const.} \cdot \frac{\nu^2}{n^2 N} I^2 \mathrm{Im}\left[\chi^{(3)}\right]. \tag{3.4}$$

The cross section describes the ability of a material to absorb the energy of the photons. For TPA, this cross section shows a quadratic dependence on the incoming intensity. Here, n is the number of absorbed photons, while N depicts the number density of the molecules that absorb. Materials have been designed for exhibiting a specifically high cross section for TPA. In the following, an insight to the chemical background will be given before the detailed procedure of the fabrication process is presented.

3.2 Chemical Background

The fundamental functionality of the vast majority of photoresists for TPA is a mixture of a monomer/oligomer and a photoinitiator [45, 53]. In the following, such a polymerization procedure will be discussed. A commonly used mixture is made of the monomer pentaerythritol triacrylate (PETA, $C_{14}H_{18}O_7$), see Fig. 3.2, mixed with 1 wt% of the photoinitiator bis(2,4,6-trimethylbenzoyl)-phenylphosphineoxide ($C_{26}H_{27}O_3P$, BAPO), see Fig. 3.3a.
The exact composition of the resist sold by the manufacturer (Nanoscribe GmbH & Co. KG), which is used in this work, is not published. However, it is stated in the article [93] by author Martin Wegener, who is also a co-founder and shareholder of Nanoscribe GmbH & Co. KG that this composition is ”well investigated and largely similar to commercially available 3D DLW systems and photoresists (Photonic Professional and IP resists, Nanoscribe GmbH)”. In addition,

the list of hazardous contingents, published in the respective material safety data sheet of the resist IP-S [94], coincide with a resist made from the composition of PETA plus photoinitiator. Hence, this mixture is exemplary used in the following description of the processes that are initiated by TPA.
The process of polymerization [91, 97] describes the merger of multiple smaller molecules into a macromolecule. Typically, the small molecules are in a liquid phase, while the macromolecule becomes solid. The process is based on two chemical processes: Photo crosslinking and photo polymerization. In the photo crosslinking process a single photon is typically able to link two monomers. Regarding the photo polymerization process, a single photon can start a chain reaction of polymerization and thus, this process dominates the merger. To trigger this photo polymerization process, additional compounds can be mixed into the monomers (M), namely photo initiators (I), e.g., BAPO. Those likely absorb the incoming energy to form radicals ($R\cdot$) via an excited state I^*, compare Fig. 3.3:

$$I \xrightarrow{2h\nu} I^* \longrightarrow R\cdot \ . \tag{3.5}$$

The radicals can then attach to a monomer, forming a radical-monomer compound ($M_xR\cdot$), which then attaches to the next monomer, and so on:

$$M \xrightarrow{R\cdot} MR\cdot \xrightarrow{M} MMR\cdot \xrightarrow{M} \dots . \tag{3.6}$$

This chain reaction is stopped in either one of two possible ways when two radical-monomer chains meet:

$$M_xR\cdot + M_yR\cdot \longrightarrow RM_{x+y}R \tag{3.7}$$
$$M_xR\cdot + M_yR\cdot \longrightarrow RM_x + RM_y. \tag{3.8}$$

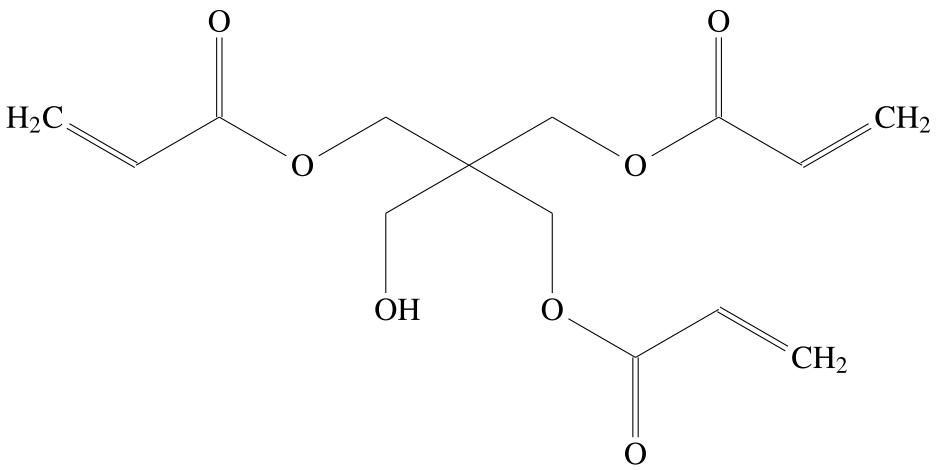

Figure 3.2: The monomer PETA, featuring three acryloyl groups at its ends, serving as a connection point for the chain reaction procedure.

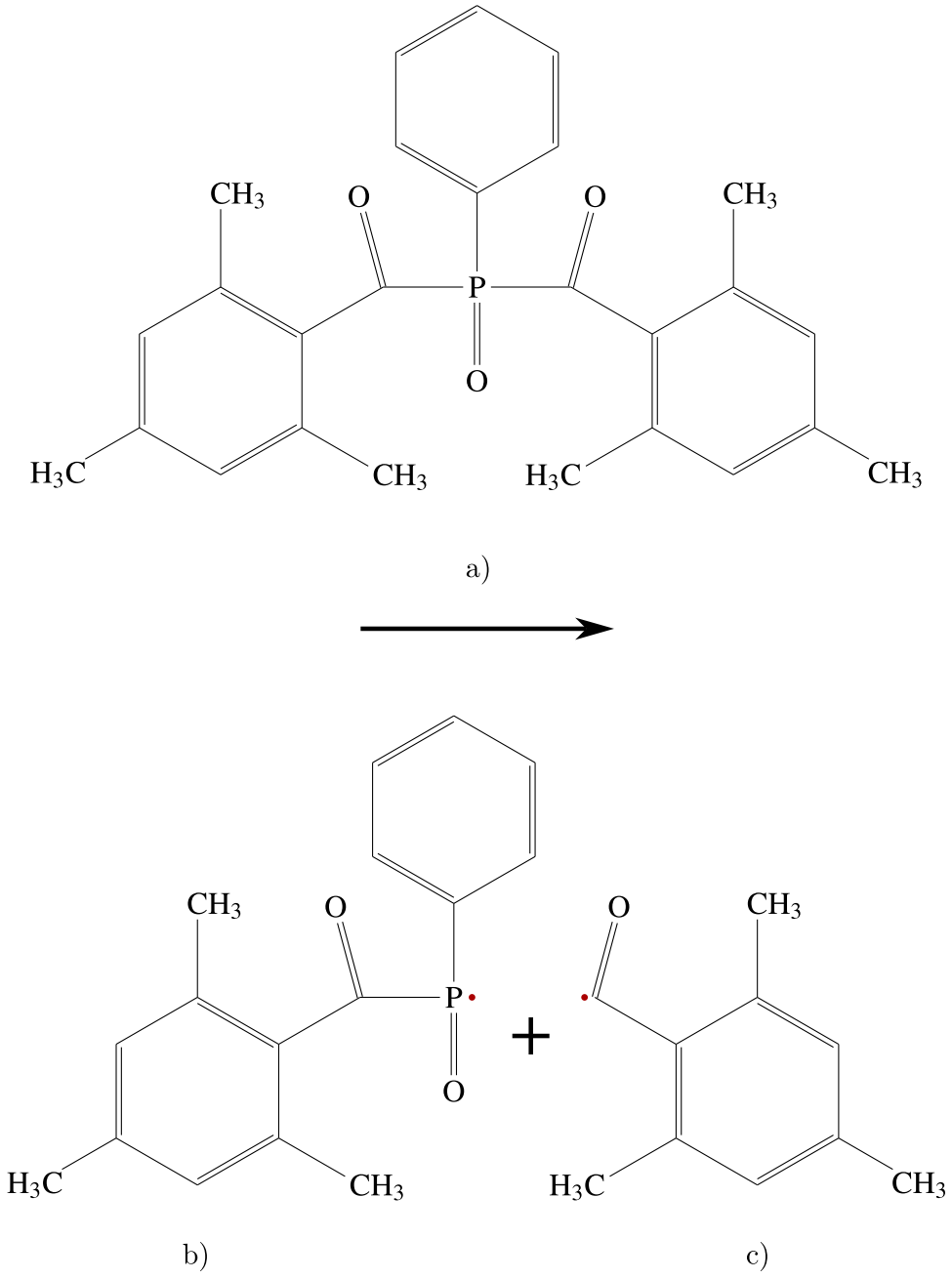

Figure 3.3: Photoinitiator (bis(2,4,6-trimethylbenzoyl)-phenylphosphineoxide), which can be transferred into two radicals when depositing the energy of an UV-photon (or due to the TPA of two NIR photons) [95, 96]. The BAPO molecule a) is split into two radicals, b) a phosphinoyl radical and c) a benzoyl radical.

A further advancement of this process is the addition of photosensitive materials to the compound. Those help to absorb the light and transfer the energy to the initiator [91]. In a development step, the monomers that did not form a chain are washed away using an organic solvent, e.g., propylene glycol methyl ether acetate (PGMEA). Further post-processing steps may improve the structure's properties, e.g., by linking residual monomers that have not been washed out (for example because they are trapped in a closed volume inside a polymerized structure). Flood-exposure via an UV source triggers this crosslinking. A plasma ashing step can lead to an improved surface quality of the obtained structure [98].

3.3 Comparison between One-Photon Absorption and Two-Photon Absorption

For a qualitative comparison between achievable results with OPA and TPA, the intensity pattern in the focal plane of the objective is assumed to follow an Airy pattern, as it would be in an idealized world. This intensity distribution can then be expressed as

$$I(x) = I_0 \cdot \left[\frac{2J_1(x)}{x}\right]^2, \tag{3.9}$$

with $J_1(x)$ being the first kind Bessel-function of order one.

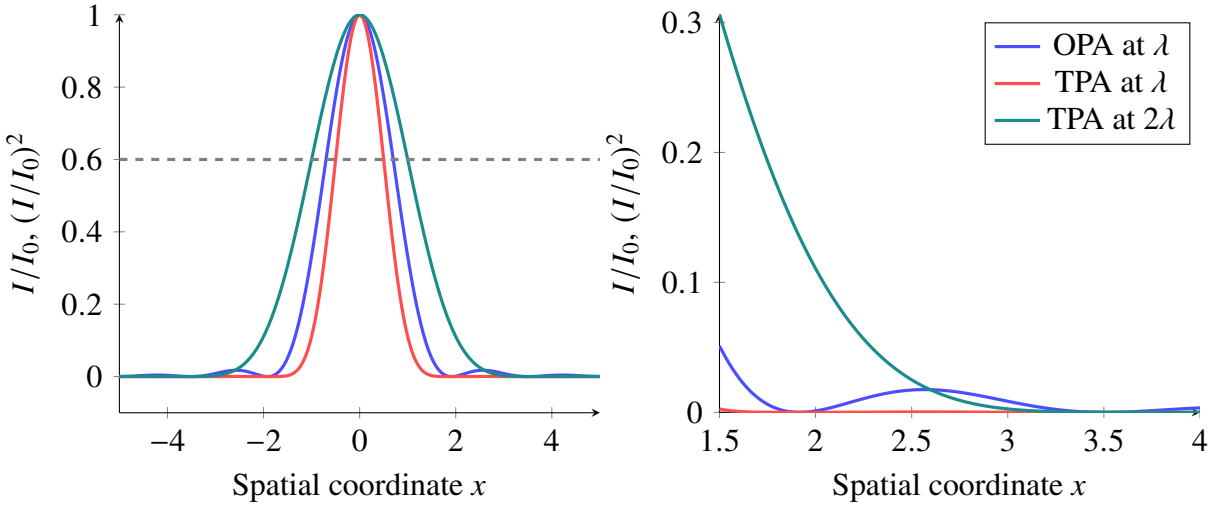

Figure 3.4: Graph depicting the cross sections of the respective processes. Since it is scaling with the intensity I, the distribution of I/I_0 in the focal plane is depicted for a one-photon absorption process. The TPA processes scale with $(I/I_0)^2$, compare Eq. 3.4. Note that an OPA-sensitive process at a wavelength λ corresponds per se to a TPA process at 2λ. The dotted gray line marks a possible threshold for the polymerization process. The right graph depicts a magnified region from the graph shown on the left.

Figure 3.4 shows a cross section through the intensity profile in the focal plane. Intensities above a threshold (chosen arbitrarily in this sketch) enable the polymerization process in the

resist and thus determine the size of the polymerized voxel. As elaborated above, TPA is a third-order process, and the TPA cross section is proportional to the squared intensity. This reduces the size of the voxel that surpasses the intensity threshold, comparing the width of the blue and the red peaks in Fig. 3.4. However, for a qualitative comparison, it needs to be taken into account that the TPA proceeds at twice the wavelength of the OPA. Including this, the achievable voxel sizes above the threshold are actually larger compared to OPA. While TPA allows arbitrary polymerizing of the resists in three dimensions, the underlying process does not assure the highest possible resolution. Small beam diameter and high NA-objective are necessary to achieve high resolutions.
However, its advantage over OPA becomes apparent on the right-hand side of Fig. 3.4, which depicts a section of the graph on the left-hand side. Side lobes present in the OPA intensity distribution are strongly suppressed in the TPA process. This is very handy for the lithography application since numerous exposures with side lobe intensities could lead to unwanted polymerization and thereby cause artifacts in the printed structure. DLW based on TPA prevents these effects by relying on a third-order process.

The volume that polymerizes follows the shape of the focal spot, see Fig. 3.5a. Its dimensions depend on the objective used, the photoresist, and the print parameters, such as laserpower and scanspeed. A typical voxel has at least a lateral size of 200 nm and a height of 400 nm. It is indeed possible to print finer details using the following setup: The focal spot is only partially guided through the unpolymerized resist, while the rest is submersed, e.g., in the substrate or an already polymerized region, compare Fig. 3.5b. A resolution in the order of 150 nm has been achieved using TPA [52].

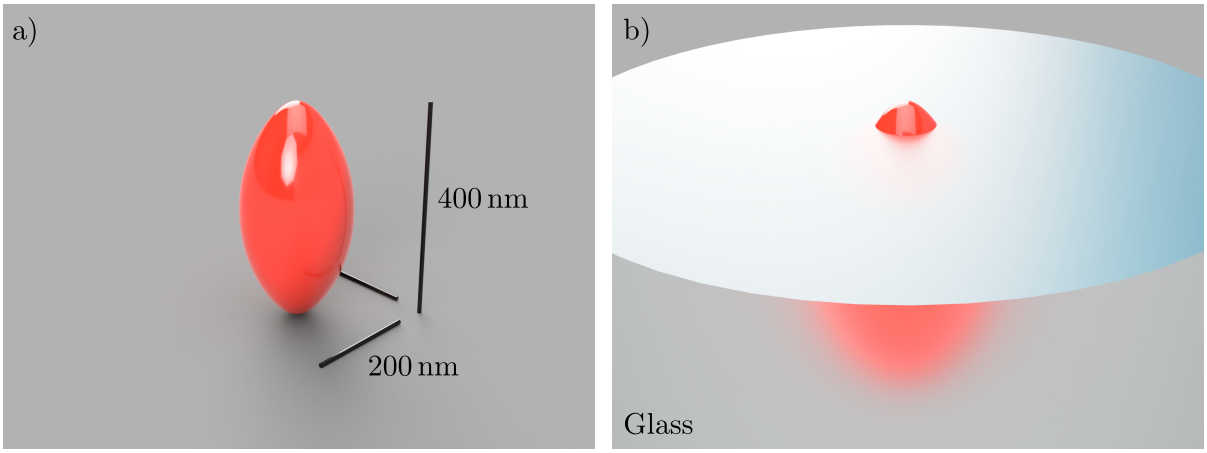

Figure 3.5: a) Representation of the typical dimensions of a voxel that follows the shape of the focal spot of the laser. Depicted here is the order of magnitude that can be reached with the 63× objective (Plan-Apochromat, Carl Zeiss AG). b) Smaller features can be realized by partially immersing the voxel into, e.g., the substrate as shown here or into already polymerized regions.

3.4 Patterning the Photoresist

In order to create arbitrary three-dimensional structures, the photoresist has to be patterned. In the DLW system used, two operation modes are available, compare Fig. 3.6 and [53]. The piezo scan mode is selected when aiming for structures with the highest possible resolution. In this case, the beam path of the laser is fixed, while the piezo stage, on which the substrate is mounted, is driven by piezo actuators in x-, y-, and z-direction. The piezo actuators provide high spatial precision but are limited in their range of movement: The piezo stage has a travel range of 300 µm in each direction. Furthermore, this mode is slow, compared to the other available one: In the galvo scan mode, the stage position is fixed and a system of galvo mirrors, located below the objective, patterns the resist. Different layers can be addressed by utilizing the z-drive of the microscope objective. Here, the achievable patterning area depends on the objective used. In both modes, the stage that is hosting the piezo stage with the sample mounted on top can be addressed for fabricating larger structures. In this case, multiple writing fields next to each other are stitched together via the movement of this rather coarse stage. This allows for structures with dimensions up to several millimeters.

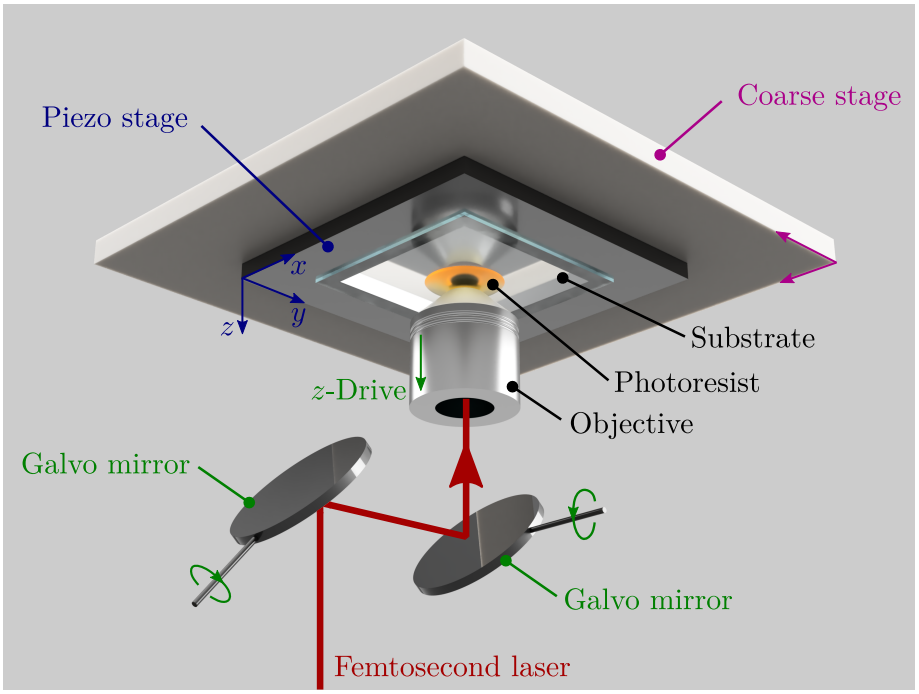

Figure 3.6: Schematic setup of the DLW system. In order to create three-dimensional structures from the presented polymerization procedure, two patterning modes are available. When using the piezo mode, the focus position is fixed and the substrate is translated by a piezo actuator-driven stage (blue components). This allows for structures with the highest possible resolution. In the other mode, the so-called galvo mode, the stage is fixed. In this case, the beam is patterned over the sample via a system of galvo mirrors. For varying the height, the z-drive of the microscope is utilized. Here, the green-marked components are involved. In order to obtain structures that extend the writing field of the piezo or galvo mode, a coarse stage (indicated in purple), hosting the piezo stage with the sample, can be addressed for stitching together structures from multiple writing fields.

3.5 Designing a Structure

Scanners for three-dimensional objects on various scales [99–102] can be purchased on the market. Furthermore, everyone with a smartphone can nowadays scan three-dimensional: Open source software is available for download, which remodels an object based on several images taken from different positions and angles if only enough images and reference points exist. This 3D-scanning is especially useful if one owns an object that shall be copied. Restrictions on this application are posed by the maximum detail that can be resolved and by the inner structure of the object.
The more common way of preparing a printable file is programming in a computer-aided design (CAD) software. CAD software allows to define geometries in three dimensions, and some software even prepares them for 3D printing. Often, these programs also offer a simulation tool, for example, calculating the mechanical stress a printed part could withstand, given that no printer-induced flaws occur. The software Describe (Nanoscribe GmbH & Co. KG) provides a tool to import .stl-files. The software slices the model according to the chosen settings and provides the DLW system with the necessary information for printing, such as where to polymerize the material at which dose.
For applications demanding fine and accurate structures, it has proven beneficial to program the laser paths manually. For this purpose, Describe allows editing and compiling .gwl-files. ".gwl" is the suffix of files of the so-called general writing language (Nanoscribe GmbH & Co. KG). Since its syntax differs from common programming languages, I created a program library with C89. The library allows programming in C-code using the commands referenced in the library file. Compiling the code creates a .gwl-file, and the three-dimensional structure can be displayed using Describe.

3.6 Surface Processing and Characterisation

Inserting additional dielectric material into the optical cavity leads to a degradation of its optical properties. High optical quality and a huge number of round-trips per photon are specifically important for sophisticated experiments aiming at, e.g., the strong-coupling regime. Even when not directly aiming for that regime, we still need to ensure a decent optical quality for our observations.
Analog to the description in Eq. 2.7, the finesse can be expressed by the quotient of 2π and the total round trip losses. In the present case, this adds up to

$$\mathcal{F} = \frac{2\pi}{T_1 + L_1 + T_2 + L_2 + L_{\mathrm{scat}} + L_{\mathrm{abs}} + L_{\mathrm{clip}}}. \tag{3.10}$$

The values for T_1, L_1, T_2, and L_2 are well known from the coating procedure of the mirror surfaces: A fiber mirror ($T_1 = 2000\,\mathrm{ppm}$, $L_1 = 15\,\mathrm{ppm}$) in combination with a half inch mirror substrate ($T_2 = 10\,\mathrm{ppm}$, $L_2 = 15\,\mathrm{ppm}$) are chosen to improve the impedance matching for the case when additional polymeric material (adding losses in the order of 1000 ppm) is inserted into the system on top of the flat mirror substrate.
The used photoresist (IP-S, Nanoscribe GmbH & Co. KG) features small absorption losses L_{abs}. Neglecting those and any clipping losses (L_{clip}) leaves us with the scattering losses (L_{scat}) of

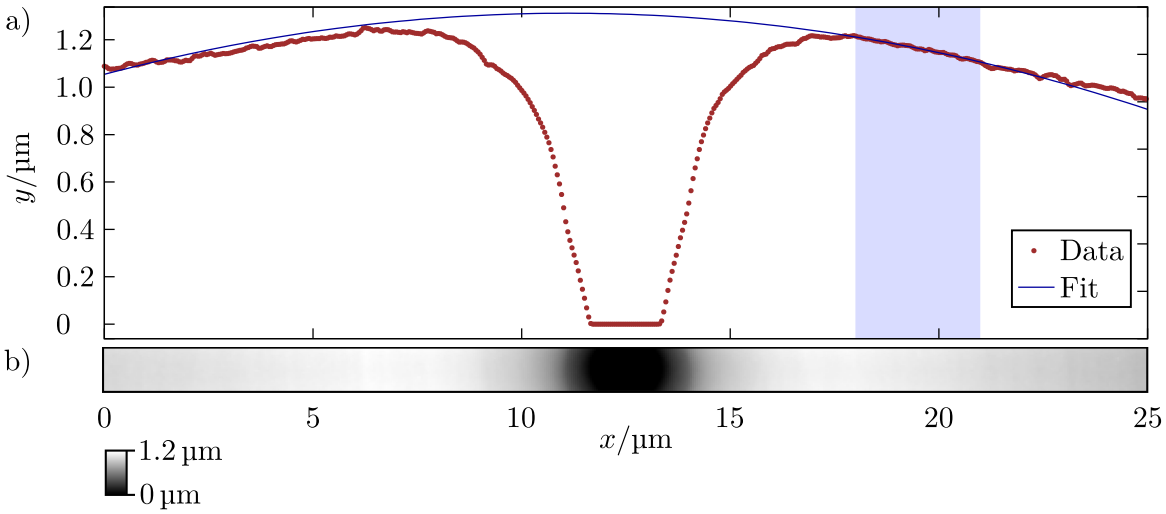

Figure 3.7: AFM measurement of a printed disk structure. Depicted are the results of a scan covering the central region of the disk. Part a) presents the height profile of a single linescan across a polymeric disk. A second-order polynomial is fitted over a distance of 3 µm to the data points. Here, the best fit is obtained in the interval [18 µm : 21 µm]. The structure is fabricated multiple times with various laser powers and hatching distances. The deviations from the second-order polynomial are used to analyze the dependency of the surface quality on the parameters. Part b) depicts the full AFM scan from which the linescan of a) is extracted.

the polymeric structure inside the cavity. The scattering losses can be split up into scattering happening in the bulk material and scattering at the surface of the structure. However, the scattering losses at the textured surface dominate every other mentioned loss channel to such an extent that we will exclusively focus on these.
As mentioned above, the shape of the voxel follows the focal spot size. For many applications, including the optomechanical experiments realized here, obtaining superb surface quality is beneficial or crucial. This means the surface roughness must be reduced as much as possible. Starting from the beginning, circular drums were the first approach. Here, concentric written voxel lines are stacked. The separation between the concentric lines in lateral direction is called hatching distance. When analyzing the printed structure in the optical microscope, a distortion of the print becomes obvious: The spots where the concentric lines start and end are prominent in the images and definitely pose a surface defect.
For improvement, the printing pattern is adapted: A spiral pattern with the same hatching distance results in a structure that does not exhibit a seam defect at first sight. The measurement of the surface of these structures in an atomic force microscope (AFM, the AFM mode of the neaSNOM, Attocube Systems GmbH, is used) reveals another flaw of the design. In the center of the spiral, several difficulties occur: Due to the decreasing circumference, adjacent lines are polymerized in much shorter time intervals than on the outer regions. This affects the polymerization process so that the effectively deposited dose is increased. In addition, the spiral pattern ends at some point. Thus, the very central region inevitably exhibits a deviation. Especially this central region (order of magnitude: Beam waist of the cavity mode) is particularly important in the optomechanical experiments.

However, the regions outside the center can be used for an investigation of the surface quality. A parameter sweep in varying both, laserpower and the hatching distance, is performed. The resulting structures are investigated with the AFM. For further investigations, a single linescan through the center of the structure is extracted. Figure 3.7a exemplary shows such a profile measured over the surface of a structure, extracted from the AFM measurement depicted in Fig. 3.7b. Here, a range of 3 µm length is chosen to fit a quadratic polynomial to the data points in that range. Additionally, the deviation w from the fit f to the N data points (x_i, y_i) is calculated via

$$w = \sqrt{\frac{1}{N-3}\left[(y_1 - f(x_1))^2 + (y_2 - f(x_2))^2 + ...\right]}. \tag{3.11}$$

This is performed for all ranges of the linescan, separated by a distance of 200 nm. A mean of the ten smallest values of w is calculated to weigh possible anomalies not too much. Table 3.1 presents the resulting values. As a result, the hatching distance is chosen to 62.5 nm. Furthermore, the measurements reveal a higher surface quality at lower doses. Thus, the dose is set to a value that barely triggers the polymerization process. Consequently, the region patterned to these specifications typically shows a reduced overall height. As a next step, chemical solvents are applied to the structures to improve the surface quality. Acetone, methoxy-nonafluorobutane (Novec 7100 Engineered Fluid, 3M Deutschland GmbH), and N-methyl-2-pyrrolidon (NMP) are tested in the development process, but the AFM measurements indicate that none clearly improves the overall surface quality.
In addition, none of the post-development procedures can compensate for the inherent imperfection at the center of the disk. Thus, a different printing pattern, the so-called woodpile structure, is applied [48]. Inspired by the relatively smooth surface at the outer regions of the disk, a frame formed by a ring structure is filled with a layer of straight voxel lines, parallel to each other and separated by the hatching distance of 62.5 nm. The next layer is set upon this layer in a so-called slicing distance of 263 nm, compare Fig. 3.8a. Following this procedure, the central

Table 3.1: Results of a surface characterization procedure. Structures are fabricated with varying laserpowers (LP) and varying hatching distances (hd). The resulting array is then examined with an AFM to determine the surface quality. The table shows the variation around the fitted polynomial as well as their standard deviation for the regime where the deviations from the data points to the polynomial are minimal. Here, the sample is additionally treated with Novec 7100 Engineered Fluid. However, this does not improve the surface quality, so such treatment is omitted in further development processes.

	hd = 250 nm	hd = 125 nm	hd = 83.3 nm	hd = 62.5 nm
LP = 30%	15.32 nm σ = 0.91 nm	5.44 nm σ = 0.18 nm	6.37 nm σ = 0.24 nm	5.25 nm σ = 0.31 nm
LP = 25%	10.90 nm σ = 0.34 nm	4.89 nm σ = 0.28 nm	4.51 nm σ = 0.59 nm	3.77 nm σ = 0.31 nm
LP = 22%		3.76 nm σ = 0.35 nm	4.04 nm σ = 0.26 nm	3.28 nm σ = 0.36 nm
LP = 20%				3.56 nm σ = 0.09 nm

part of the disk is not exceptional in the printing process and exhibits the same surface finish as the surrounding area. Hence, features arising due to a singularity, as present in the concentric printing pattern and the spiral pattern, do not occur using this procedure. Measurements with the AFM reveal a very smooth surface, with deviations in the order of 25 nm over a distance of 15 µm. Figure 3.9a shows the profile extracted from the AFM measurement depicted in Fig. 3.9b. Here, the surrounding frame around the membrane clearly stands out since it was written at a higher dose. Hence, Fig. 3.9c presents a cropped domain of the profile depicted in Fig. 3.9a, which illustrates the scale on which fluctuations of the surface roughness occur. In the direction perpendicular to the uppermost printed voxel lines, the surface quality is good but not outstanding. To improve the quality of the surface for our experiments, the relevant layers, meaning the very top and very bottom layer of the membrane, are printed in both directions, compare Fig. 3.8b. An electron micrograph of a fabricated woodpile structure (but the top layer written only in one lateral direction) can be seen in Fig. 3.8c.

The measurement of a woodpile-printed surface via AFM provides helpful guidelines for the membrane's surface quality. Indeed, the following experiments will be sensitive to the surface quality in the sense that the scattering losses dictate the outcome. However, for determination of the optical quality, the analysis of the mechanical roughness is not sufficient. Therefore, a probing setup is introduced for the measurement of optical properties.

In this setup, a semi-hemispherical cavity is constructed with a fiber mirror and a half-inch mirror substrate. By scanning the cavity in length, a spectrum is recorded, which can be analyzed and gives insight into the material inserted into the cavity. The polymeric structure is applied directly on top of the half-inch mirror substrate: A sample with step-wise increasing polymer thickness is produced using the woodpile pattern as mentioned above. It features 9 steps, each with a surface of 25×25 µm and a height difference of 25 nm between neighboring steps, covering in total a thickness of roughly $\lambda/2$.

The cavity's resonance and finesse can be directly measured in the experiment. Using a motorized translation stage, an automatized procedure is applied to create a finesse map of the structure, while the total cavity length $L_1 + d + L_2 = 30$ µm is kept constant. The finesse is normalized to the finesse measured at a position without polymeric structure. The losses attributed to the scattering at the polymeric surface are deduced using Eq. 3.10, using the known values for the mirror properties.

As presented in Ch. 2, the cavity is driven in resonance if the electric field reproduces itself upon reflection off the mirror. This gives rise to a standing wave pattern. Due to the different layer thicknesses of the polymer on the mirror substrate, the surface of the polymer structure essentially shifts through the standing wave pattern. The highest losses due to scattering at the surface are expected to happen if the surface sits at an anti-node position of the standing wave. Overall, shifting the surface through the cavity, a periodic behavior of the losses is to be expected.

Due to the lateral diameter of the light field in the cavity (about 4 µm), a certain amount of spatial averaging is already included in the measurements. This is the reason why the steps themselves cannot be resolved in the measurement, compare Fig. 3.10a.

Using this setup, the optical properties of the polymeric structures are investigated in combination with a treatment to potentially reduce losses. The first approach to smoothen the surface is applying a plasma ashing procedure. The plasma ashing machine (Zepto, Diener electronic

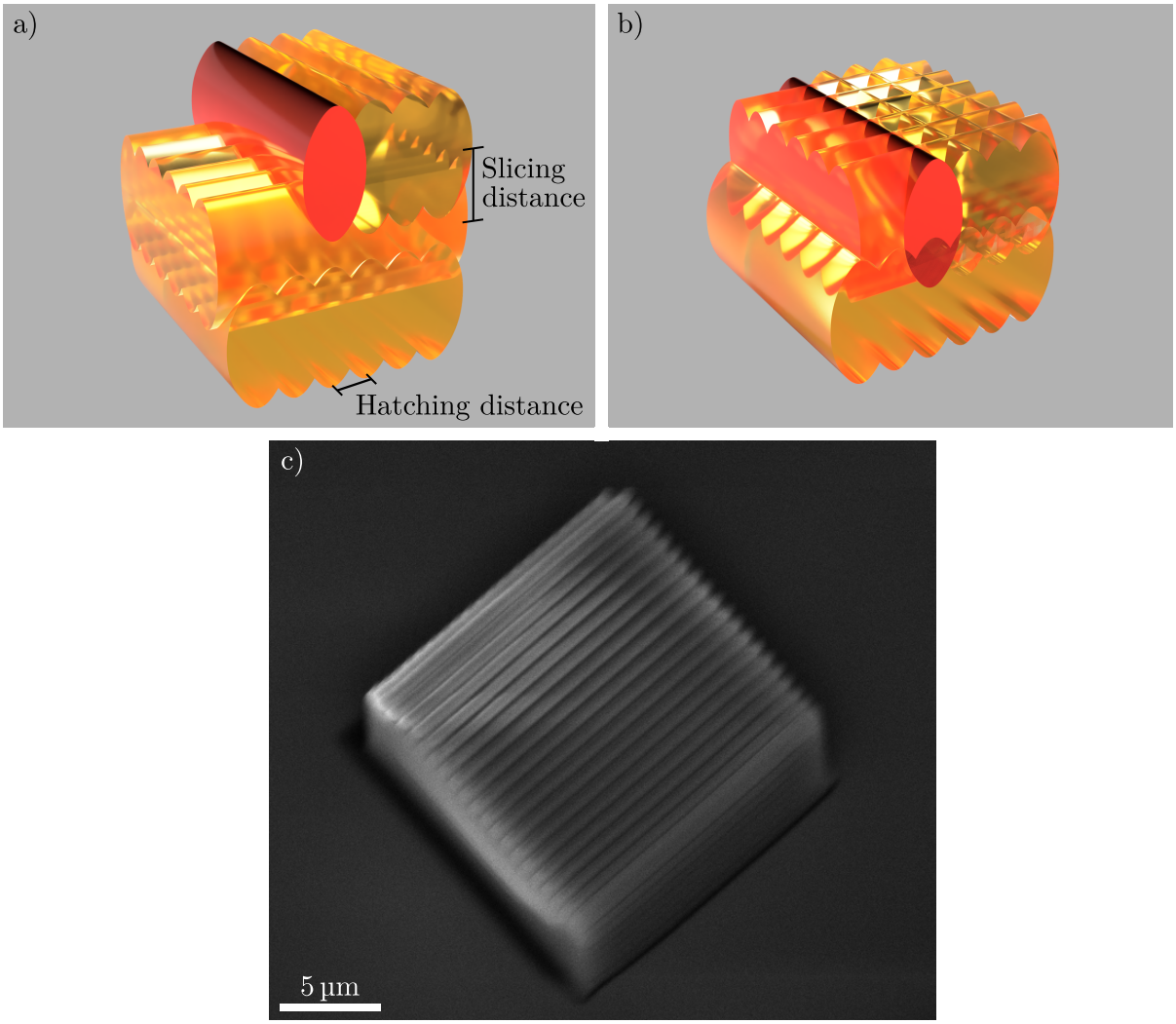

Figure 3.8: Schematic depiction of the printing process of the membrane. The voxel lines are separated in lateral direction by the hatching distance and in vertical direction by the slicing distance. a) For a region below the top surface of the membrane, the structure is made up of alternating layers in both horizontal directions. The red highlighted voxel line serves as a guide to the eye for the fabrication procedure. b) Here, the scheme includes a surface region of the membrane. In this case, the very top layer is written in both horizontal directions for improved surface quality. c) Electron micrograph of a block written in woodpile order according to the design depicted in a).

GmbH & Co. KG) is evacuated to a level of about 10 mbar (by a Scrollvac 7 Plus, Leybold GmbH) before a plasma is ignited. In this case, the plasma is created using nothing else than the surrounding atmospheric gas composition. The plasma created can thus be approximated to be an O_2-plasma. Due to the plasma process, the very top surface of the polymer is ablated. Therefore, the polymer height shrinks a little bit, which results in a shifting of the periodicity of the losses.
The plasma process creates radicals that can form a bond with free polymer ends, which are then removed by the vacuum system [103]. Thus, the exposed polymer structure undergoes a surface

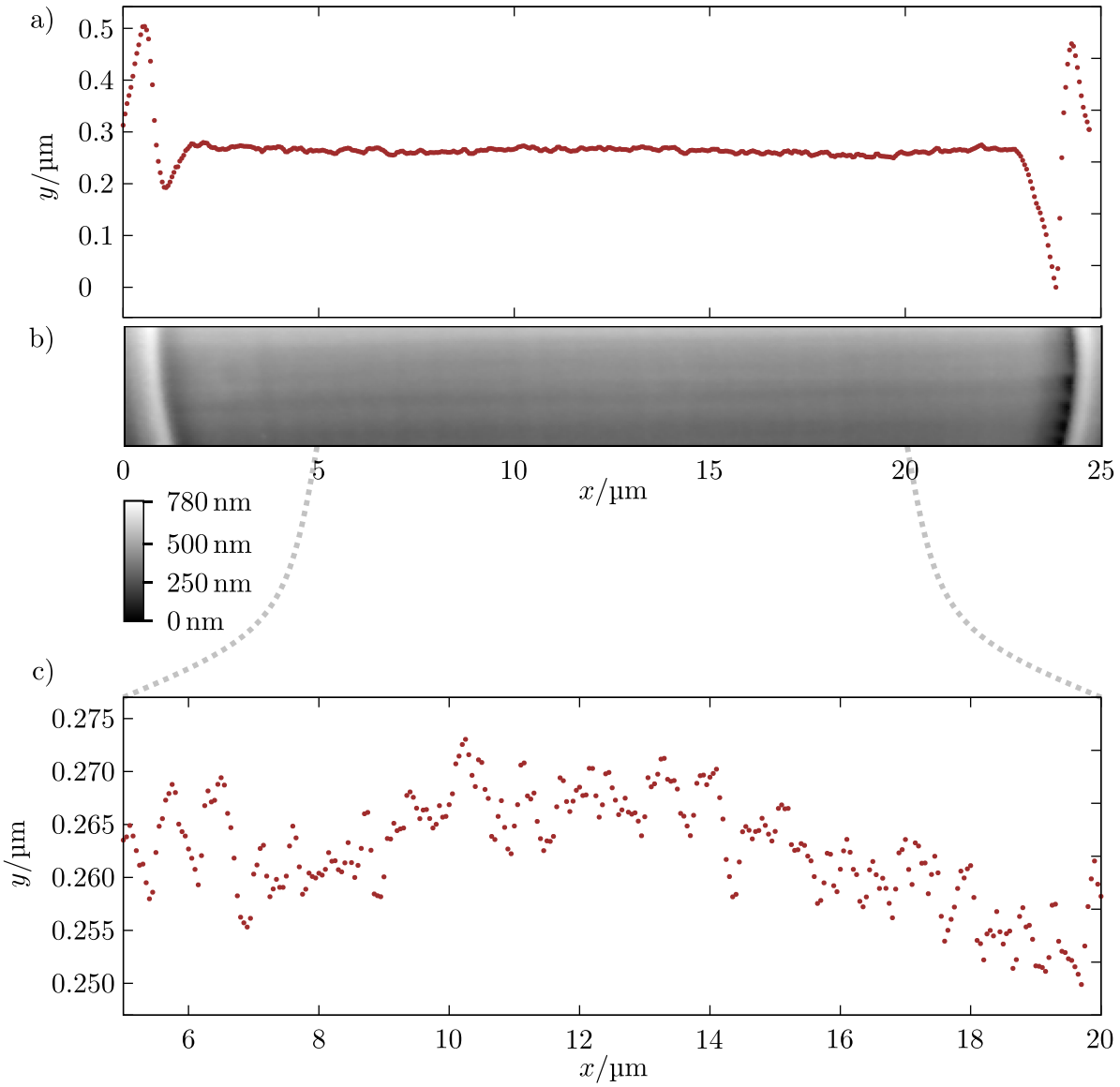

Figure 3.9: AFM measurement of membrane written in wood pile manner. A single linescan a), extracted from the full scan b), shows the surface roughness of the membrane. The ring structure, written at a higher dose, clearly stands out in contrast to the membrane area, which is written at a dose close above the polymerization threshold. An extract of graph a) is shown in c), presenting surface fluctuations in the order of 25 nm over a distance of 15 µm.

polishing procedure. The structure is exposed to the plasma over different periods at different plasma intensities. Figure 3.10a shows a finesse map of the structure and its losses after the first plasma ashing process. Figure 3.10b depicts the same sample after multiple consecutive treatments. The polishing effect can be identified by comparing the map and the averaged losses in Fig. 3.10a and 3.10b. Upon analysis of the structure between the separate steps, as shown in Fig. 3.10c, a significant reduction of the losses is found, namely by more than 35% between the untreated sample and the sample after the fourth plasma ashing treatment.

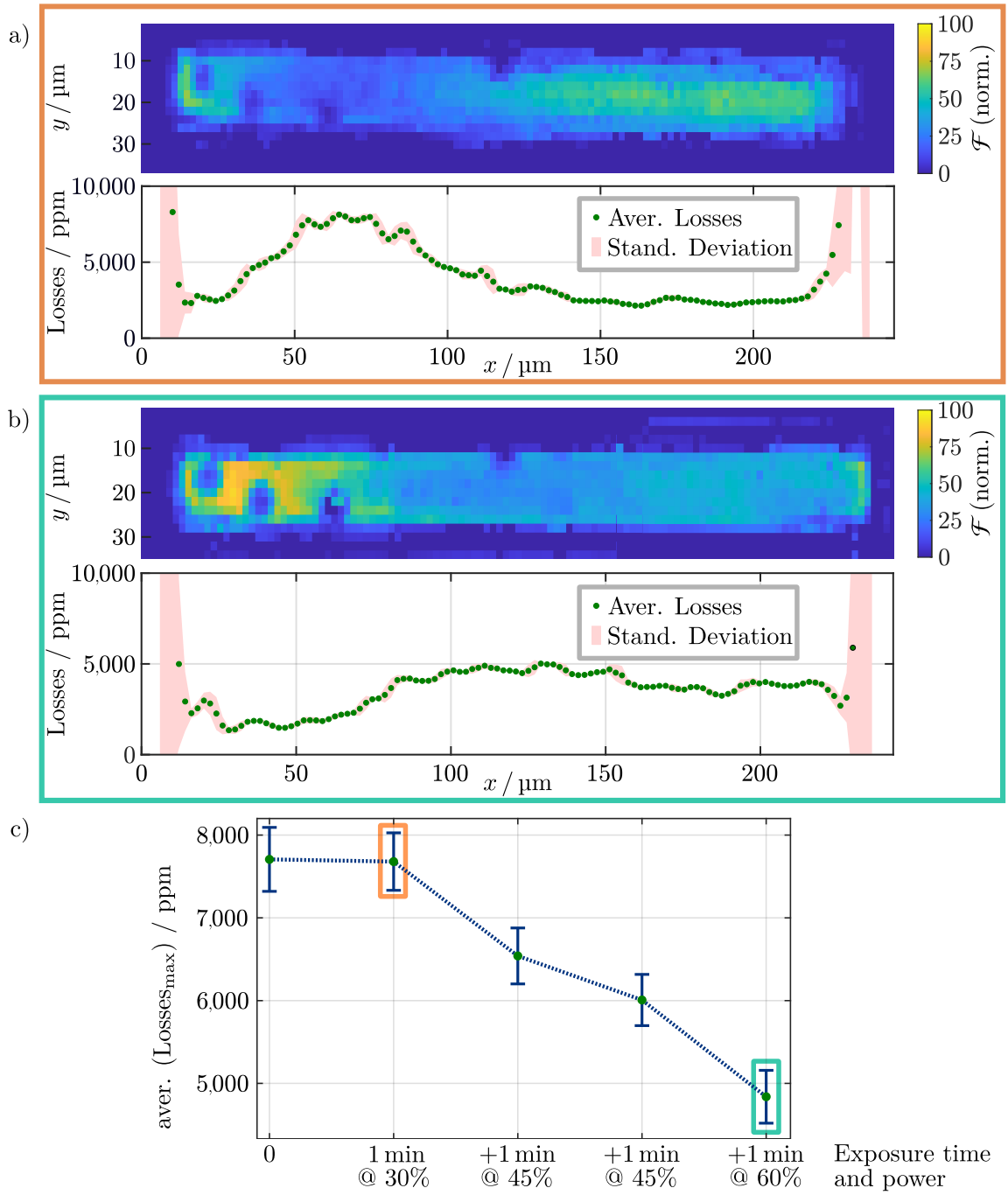

Figure 3.10: Results of the finesse measurements in between the process of plasma ashing, compare [66]. The step-shaped polymer structure is exposed to an O_2-plasma. a) A detailed map of the finesse is measured after a first polishing step with a duration of 1 minute at a plasma power of 30% of the maximal possible 300 W that the generator can provide. Each pixel of the map has a size of 2 µm × 2 µm and corresponds to a separate finesse measurement. Below, the losses averaged over the width of the structure are displayed, while apparent defects are not considered. In b), the corresponding finesse map and the losses after an iteration of four plasma ashing steps is depicted. c) The graph shows the averaged values for the losses after each individual plasma ashing step. The overall improvement of the surface quality due to the ashing can be clearly seen.

Analogously, the measurement is performed with a second structure, undergoing a different treatment, using the solvent NMP instead of plasma ashing. In contrast to the previous findings, this application does not improve the optical properties of the structure, compare Fig. 3.11. Here, the averaged losses stay constant independent of the treatment duration. This corresponds with the AFM measurements performed previously on an NMP-treated sample, showing no signs of improvement due to the treatment.

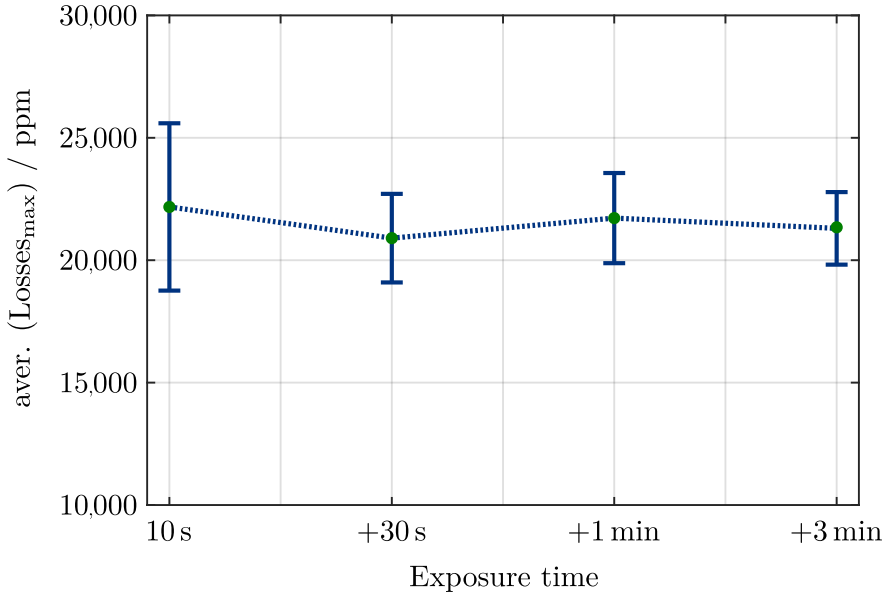

Figure 3.11: Analysis of the chemical surface treatment: The step-shaped polymer structure is exposed to NMP. Then, the finesse is measured and mapped. Via averaging, the losses for each treatment step are calculated and presented in the diagram, compare [66]. However, no evident polishing effect can be deduced by comparing the data.

CHAPTER 4

Optomechanical System

In this chapter, the performance of optomechanical structures is investigated. These structures are hosted either in a semi-hemispherical cavity (consisting of a fiber mirror and a flat half-inch substrate) or in a fiber-fiber cavity (two fiber mirrors building a cavity). First, the mechanical properties of the polymeric structures used are investigated via numerical simulations based on the finite element method (FEM). Next, the preparation procedure of the optical fibers is described. This involves fiber shooting, the coating procedure, and the assembly in a ferrule if necessary. A setup for quality control of the aforementioned procedure is presented. The printing process implementing polymeric structures with high quality on top of fiber or substrates was presented in Ch. 3. Next, the setup for the measurement of the optomechanical coupling strength of applied polymeric drums is described, and the results are presented. It is shown how the coupling strength g_0 is extracted from the measurement of the cavity's reflection spectrum. Subsequently, the experiments and the results of measurements in vacuum/cryogenic environments are presented. Here, a comparison of the mechanical properties in the three investigated environments is performed. The temperature dependence of the mechanical resonance frequency and linewidth is exploited in detail. The present loss channels are discussed, including approaches to further reduce those. In the following section, the link between the measured coupling strength and the optomechanical coupling map as presented in Sec. 2.3 is examined. In the last section, the optical spring effect is investigated by utilizing a polymeric written structure.
This project was performed in collaboration with Lukas Tenbrake and Dr. Hannes Pfeifer from the group of Prof. Dr. Sebastian Hofferberth and previously Prof. Dr. Dieter Meschede. While the design and the fabrication of the structure were done by me, the measurement and collection of data was done by Lukas Tenbrake. The analysis of the results was performed in collaboration. Thus, the results can also be found in [66] and in the publication [104].

4.1 Finite Element Simulation

Numerical simulations are a useful tool as they allow to set up the experiment in an idealized environment. Inserting the known properties and geometries allows the scientist to gain an idea on what to expect from the actual experiment.

In the following, the software Comsol Multiphysics (Comsol Multiphysics 5.6, Comsol Multiphysics GmbH) is used, which relies on a finite element solving procedure for partial differential equations. The geometry is traced using a mesh, which is then utilized to locally solve the differential equations element-by-element of the mesh. The resulting simulation is the composition of many elements of the mesh.
By inserting the known parameters into the simulation, the experimental results can be cross-checked. Alternatively, the simulation can provide insight into influences on the expected resonance frequency. This can be used to adapt the geometry to yield in a certain frequency regime.
In the following, we take a look at the mechanical properties of the polymeric structure. The eigenfrequency Ω_m of the fundamental mechanical mode is derived.

4.1.1 Simulation Procedure

For the sake of simulating the mechanical modes of the structure, the program requires the user to insert the mechanical properties of the material used. Here, the properties according to the specifications provided by the supplier of the resist [94], and the density of the polymerized material as specified in [105] for the resist IP-S are used:

$$\text{Young's modulus} \qquad E = (5.33 + \imath 0.26) \cdot 10^9\,\mathrm{Pa} \tag{4.1}$$

$$\text{Poisson's ratio} \qquad \nu_\mathrm{P} = 0.3 \tag{4.2}$$

$$\text{density} \qquad \rho = 1.15 \cdot 10^3\,\frac{\mathrm{kg}}{\mathrm{m}^3}. \tag{4.3}$$

It should be noted that the resist properties themselves depend on the specific fabrication procedure, including laserpower, scanspeed, or development characteristics. Therefore, the results can provide a guideline as to what might be expected but should not be taken for granted in an experiment. The material properties of SiO_2 are chosen for the fiber.
Next, a geometry is defined. In this step, one can save computational time and resources since the investigated structure exhibits symmetries. Thus, one can limit the computational domain to a unit cell and mirror the resulting solution.
The geometry is chosen according to the design of the structure that has been fabricated. The dimensions of the printed structure can be checked via electron micrographs taken by a scanning electron microscope (SEM, Zeiss Sigma Gemini, Carl Zeiss AG), see Fig. 4.1a. Via tilting the stage, multiple perspectives depict the outcome of the fabrication procedure. However, the determination of the effective height of the membrane itself is not apparent.
Thus, a structure with an opening is fabricated and utilized to measure the thickness of the membrane, compare Fig. 4.1b. The thickness of the membrane can be estimated to roughly 3 µm from the SEM capture. The membrane is thinner compared to the surrounding frame due to the printing procedure: As explained in Ch. 3, exceptional surface quality can be obtained with a woodpile-structured procedure driven at a laserpower that just barely triggers the polymerization process. The frame is written with higher speed at a higher laserpower, since its surface quality is not of interest. Thus, it exhibits a bigger thickness.

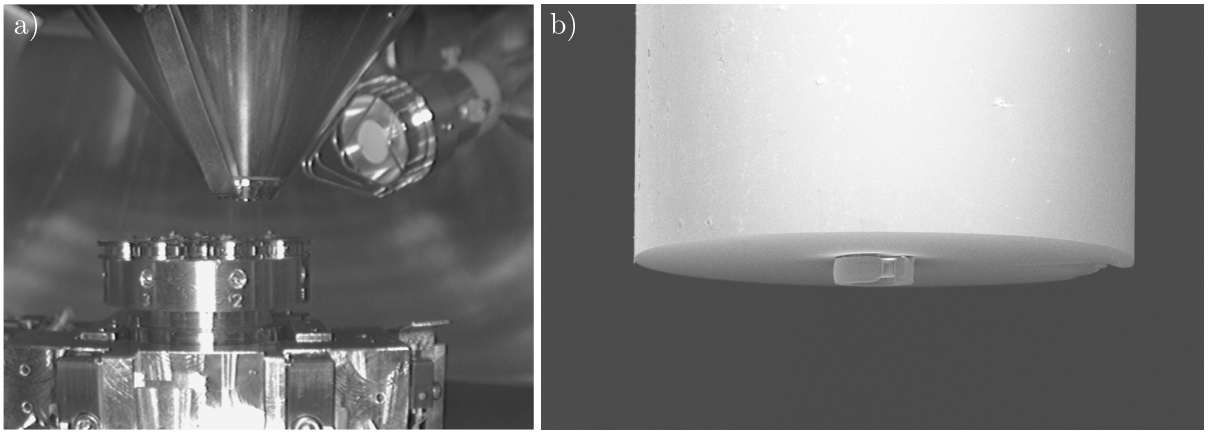

Figure 4.1: a) View inside the SEM. For the examination of fibers, those are glued with conductive carbon pads onto a stage that can be tilted to adjust the viewing angle. b) Structure for checking the membrane thickness of the printing process exhibiting an intentional opening. Due to the tilted viewing angle, a scale bar would be misleading, but as a guide for the eye, the diameter of the fiber can be specified to 125 µm.

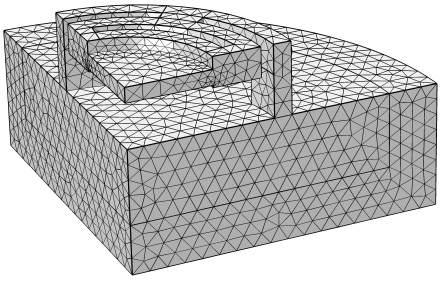

Figure 4.2: Shown is a generated mesh whose spacing depends on the richness of detail of the underlying topology, covering the geometry of the structure. Depicted is one quarter of the whole entity since only the symmetrical modes are of interest here. Thus, symmetrical boundary conditions are applied to yield relevant modes at reduced computational load.

For the simulation, the fiber is surrounded by a perfectly matched layer, absorbing impinging energy without reflection. The fiber has a finite length, and its bottom end is defined as a fixed layer. Due to the aforementioned simplification, the cut faces of the structure are defined as symmetry planes. For the simulation, the structure is set in a vacuum surrounding, which means possible losses through the air are not considered.

Simulation Fundamentals For the determination of the eigenfrequency, the underlying formalism is given by

$$\left[\mathbf{K} + \imath\Omega\mathbf{C} - \Omega^2\mathbf{M}\right]\mathbf{u} = 0 \tag{4.4}$$

with stiffness matrix $\mathbf{K}$, angular frequency Ω, mass matrix $\mathbf{M}$, viscous damping matrix $\mathbf{C}$, and the displacement vector $\mathbf{u}$ for the eigenmode [106, 107]. The stiffness matrix itself incorporates a

set of equations describing the interplay between nodes via the generalization of spring constants arising from Hook's law. Neglecting damping ($\mathbf{C} = 0$) results in

$$\left[\mathbf{K} - \Omega^2 \mathbf{M}\right] \mathbf{u} = 0. \tag{4.5}$$

This differential equation fully describes the oscillation of the structure. In the following, it will be applied to a set of spatial points on the structure to determine the local movement and thus the shape of the eigenmode.

Mesh In the next step, the geometry is traced via a mesh. This mesh is utilized in the following for the local solving of the differential equations. The mesh itself is generated by the software and has to be chosen fine enough for the simulations to converge: This implies that a refinement of the mesh will not influence the simulation results. Simultaneously, the meshing is chosen to be adequately large to keep the computational load light and reduce the simulation time. An exemplary result of the meshing procedure can be found in Fig. 4.2. Numerically, the differential equation system is solved, resulting in the mechanical displacement field $\mathbf{u}(x, y, z)$ of the respective eigenfrequencies Ω_m based on the material, geometry, boundary, meshing, and a predefined evaluation range.
The mechanical displacement field can be thought of as assigning vectors to the points of the body to describe its deformation transition. Here, the transition occurs from the inserted geometry to the deformation that arises due to the resonant oscillation at an eigenfrequency.

4.1.2 Drum Geometry

In the course of work, we first started with a drum-shaped membrane and evaluated its geometry. We analyzed the effect of additional slits in the outer areas of the drum. The idea is to uncouple the membrane in the middle as much as possible from the outer frame and the feet. This would potentially prove useful in a vacuum environment and minimize the losses: In vacuum, one loss channel of the mechanical energy is the coupling of the motion to the underlying substrate (or fiber). These losses are additionally suppressed by the impedance mismatch between the polymeric structure and the fiber: Since the speed of sound in both materials differs, energy can not be efficiently coupled from one to the other material. Therefore, the main loss channel is the damping inside the material itself due to energy being lost in the deformation process. In the case of an atmospheric environment, the damping due to the surrounding gas molecules is the dominating loss.
The geometry used is depicted in Fig. 4.3. According to the aforementioned procedure, the drum is divided into quarters, and symmetrical boundary conditions are applied at both cut faces. The aim of the simulation is the determination of the eigenfrequencies of the structure. With the found eigenfrequency of a mode, a set of properties can be derived for the given mode. For the drum-shape, a simulated eigenfrequency of

$$\Omega_\mathrm{m}/2\pi = (1.721 + \imath 0.042)\ \mathrm{MHz} \tag{4.6}$$

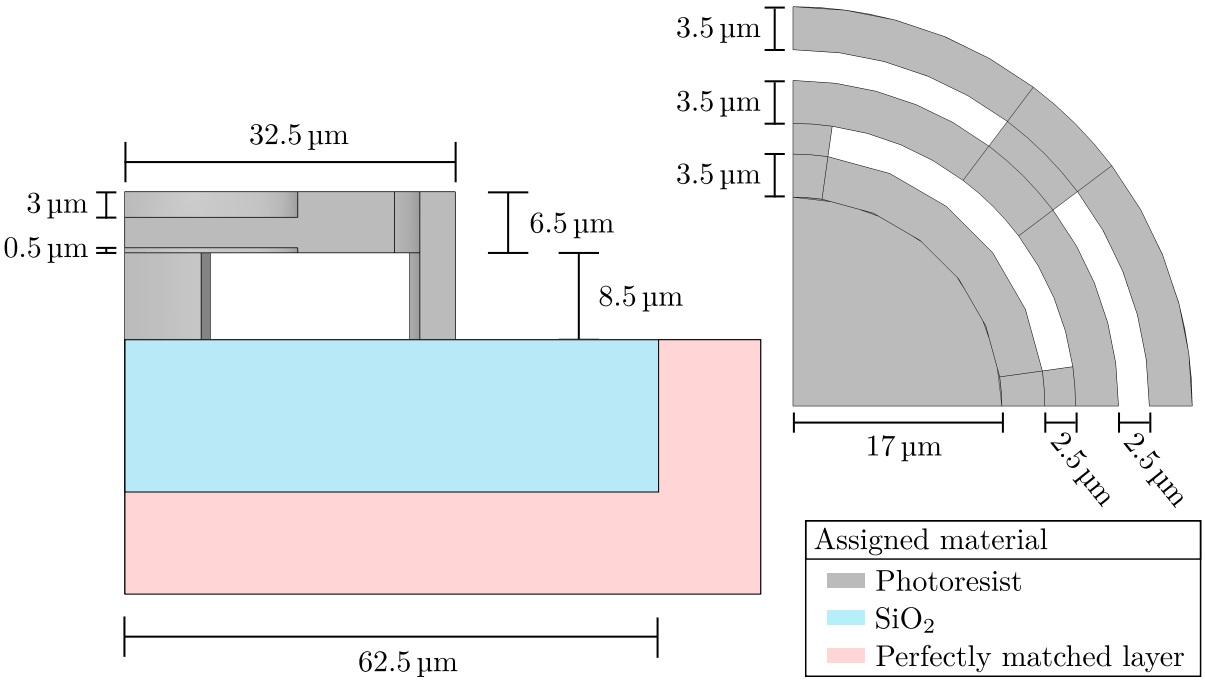

Figure 4.3: Geometry of the structure that is the basis for the calculations. The drum-shaped structure, with assigned photoresist properties, is located on a cylindrical shape, representing the fiber and assigned SiO_2 properties. The drum-shaped structure's dimensions closely follow the values that are extracted from micrographs taken of real structures.

is found. This is the fundamental mechanical mode of the structure according to the mode shape calculated by the program and depicted in Fig. 4.4a. This picture also reveals how stored energy is coupled to the fiber and thus guided away from the mechanical motion. The associated mechanical quality factor, defined as the quotient of the resonant frequency and the mechanical linewidth, is calculated to $Q = 20.511$. From the simulation, the integral over the polymeric volume calculating the maximum displacement squared and multiplied by the density of the polymer is determined as $5.29 \cdot 10^{-32}\,\mathrm{kg\,m^2}$.
The maximal displacement squared yields in $9.37 \cdot 10^{-21}\,\mathrm{m^2}$. The equation

$$m_{\mathrm{eff}} = \frac{\int_V \mathrm{d}V \rho |\mathbf{u}(x,y,z)|^2}{\max(|\mathbf{u}(x,y,z)|^2)}$$

allows determining the effective mass of the mode. The formula weights the displacement of a mass element with respect to its oscillation energy normalized by the total potential energy available in the mode [108, 109].
The effective mass thus results in $m_{\mathrm{eff}} = 5.65 \cdot 10^{-12}\,\mathrm{kg}$. Here, the integral for the weighted displacements is applied over the whole volume of the structure. This has to be considered when the computational domain is reduced and symmetries are applied.
The zero-point motion is calculated using $x_{\mathrm{ZPM}} = \sqrt{\hbar/(2m_{\mathrm{eff}}\Omega_{\mathrm{m}})}$ and yields in $x_{\mathrm{ZPM}} = 9.30 \cdot 10^{-16}\,\mathrm{m}$. With the z-component of the displacement field $w = 9.66 \cdot 10^{-11}\,\mathrm{m}$ at the

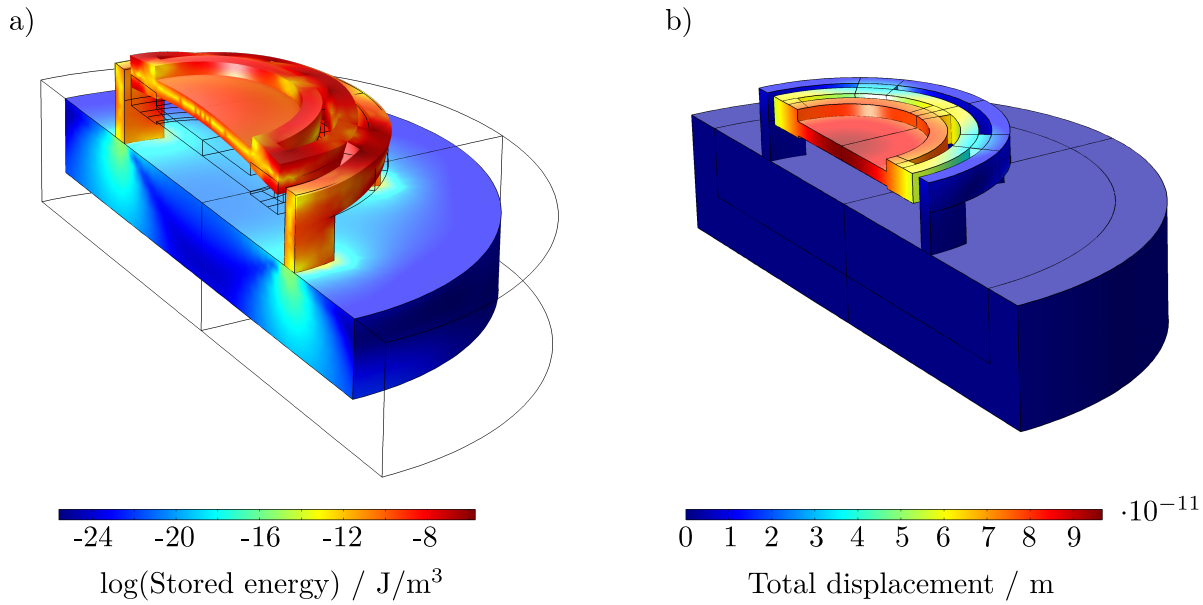

Figure 4.4: a) Result of the eigenfrequency analysis of the simulation software on the geometry as shown in Fig. 4.3. The colorbar depicts the logarithm of the stored energy density. The deformation shows the displacement field, scaled with a factor of roughly 65, 000 for the sake of visualization. b) Structure with a colorbar encoding the total displacement.

membrane center, compare Fig. 4.4b, and a maximal displacement of $\mathbf{u}_{\max} = 9.68 \cdot 10^{-11}$ m, the optomechanical coupling strength g_0 could be determined via $g_0 = G^{(1)} \cdot x_{\mathrm{ZPM}} \cdot w/(\mathbf{u}_{\max}) = 1.02 \cdot 10^4$ Hz. Here, the frequency-pull parameter $G^{(1)} = 11\,\mathrm{GHz/nm}$, acquired from the optomechanical coupling map as presented in Fig. 2.10a, is used.

4.1.3 Bridge Geometry

Several different geometries have been tested and compared. Starting from the simple drum structure, including slits as described above, and another one without slits, oval and quadratic shaped drums, directly connected to the outer frame or suspended freely, to relatively simple bridge-like structures. In the experiment, the simple bridge-like shape exhibits comparably high coupling values. In the following, this bridge-like structure is examined via an FEM simulation. The structure features a rectangular footprint. It is based on two feet, extending each over a rectangular base's complete side. The two feet support a cuboid on their top, as illustrated in Fig. 4.5a. The footprint of the rectangular block is 45 µm × 60 µm, thus the net membrane area is 45 µm × 50 µm, since the feet on the 45 µm-wide side have a width of 5 µm. The membrane itself has a thickness of 6 layers, which can be estimated to be roughly 2.7 µm. The height of the feet here is 8.5 µm.
Again, two symmetry conditions are applied. The simulation determines the frequency of the fundamental mode to

$$\Omega_{\mathrm{m}}/2\pi = (2.140 + \imath 0.052)\ \mathrm{MHz}. \tag{4.7}$$

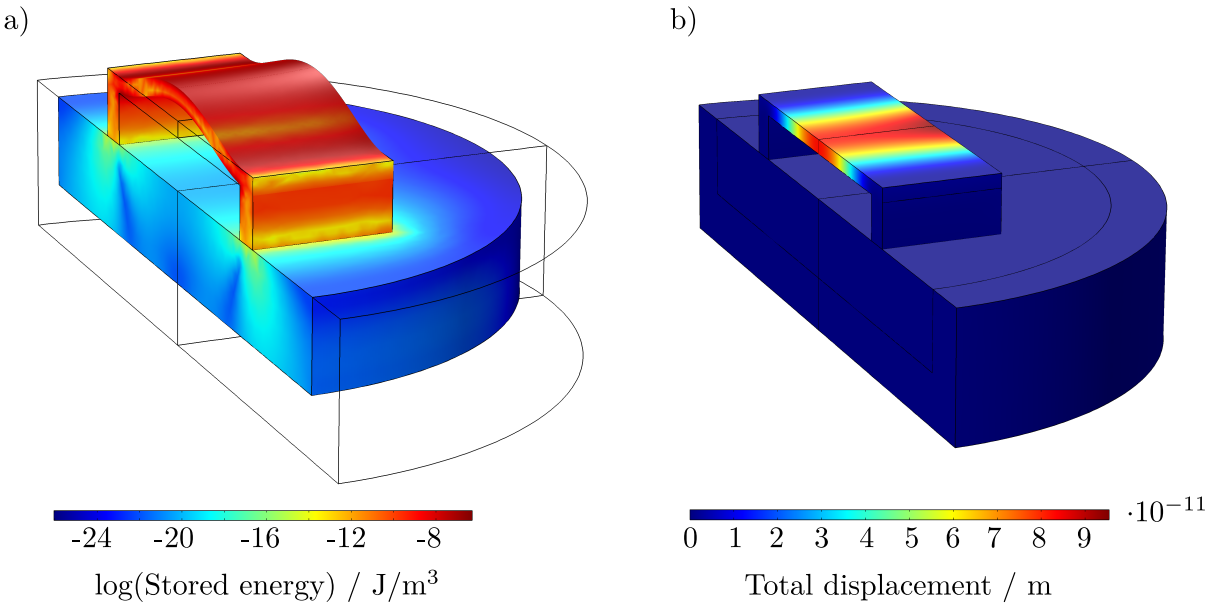

Figure 4.5: a) The result of the analysis of the bridge-shaped geometry with the colorbar depicting the logarithm of the stored energy density. Again, the deformation shows the displacement field, scaled with a factor of roughly 65, 000 for the sake of visualization. b) Structure with a colorbar encoding the total displacement.

The corresponding mechanical quality factor is calculated to $Q = 20.538$. Analogously to the simulation of the drum on the fiber, the value of the integral over the polymeric volume calculating the maximum displacement squared and multiplied by the density of the polymer is determined to $2.22 \cdot 10^{-32}$ kg m^2. The maximal displacement is $\mathbf{u}_{\max} = 9.55 \cdot 10^{-11}$ m. The z-component of the displacement field yields to $w = 8.23 \cdot 10^{-11}$ m.
Thus, the effective mass $m_{\text{eff}} = 2.43 \cdot 10^{-12}$ kg can be calculated. The zero-point motion is $x_{\text{ZPM}} = 1.27 \cdot 10^{-15}$ m. Therefore, the optomechanical coupling strength can be determined via $g_0 = 1.20 \cdot 10^4$ Hz. Again, the frequency-pull parameter $G^{(1)} = 11$ GHz/nm is used.

4.1.4 Parameter Sweep

A parametric sweep of the geometry variables enables the optimization of the structure with respect to this property. In the following, we present the results of several sweeps aiming at improving the mechanical structure. Depending on the chosen geometry, a shift in the eigenfrequency of the fundamental mode is observed. Likewise, the mechanical quality factor, a figure of merit of the damping, is derived. The effective mass m_{eff} and the resulting zero-point motion x_{ZPM} are determined based on the values found. The vacuum coupling strength is not considered due to its dependence on $G^{(1)}$, which has to be evaluated separately for each membrane thickness and membrane height above the mirror. Nevertheless, the values found provide insight into the intrinsic behavior of the geometries.
The mechanical motion of the bridge-shaped structure is investigated. The varied variables are named according to the scheme presented in Fig. 4.6. The first sweep covers the dependence of

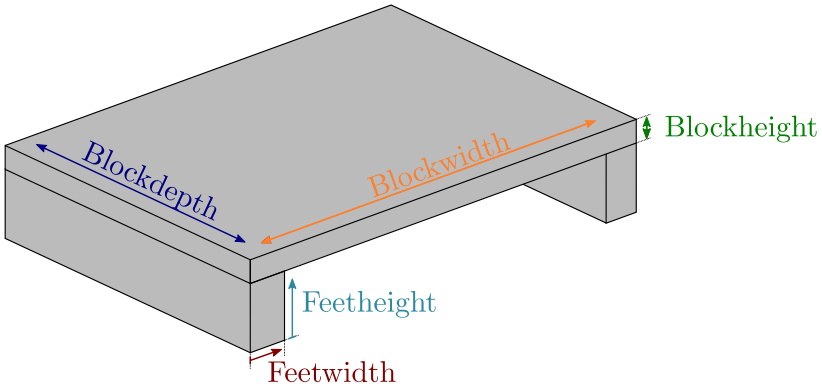

Figure 4.6: Schematic depiction of the bridge geometry with the parameters that are varied in the following sweep procedures.

mechanical properties on blockwidth and blockdepth. These values determine the overall size of the structure in two dimensions. Figure 4.7a shows that the eigenfrequency of the fundamental mode is independent of the blockdepth. This can be understood intuitively when looking at the mode's displacement field as depicted in Fig. 4.5a. The mode shape inhibits a displacement variation in the direction of the blockwidth, but not in the direction of the blockdepth. The dependence on the blockwidth shows that the structure's eigenfrequency increases for smaller widths, corresponding to a stiffer structure.
What becomes evident in Fig. 4.7b is the low bandwidth of the achieved Q-factors. There is no specific combination that stands out and provides extraordinarily high Q-factors. Intuitively, the effective mass being moved by the fundamental mode as represented in Fig. 4.7c experiences a maximum if both, the blockdepth and blockwidth, are maximized. Likewise, the absolute minimum is observed for the minimum of both dimensions. The zero-point motion, depicted in Fig. 4.7d, as incorporating the eigenfrequency and the effective mass, is maximized where the product of these constituents is minimized.
Comparing these graphs to those in Fig. 4.8 indicates that the height of the block influences the mechanical mode, in contrast to the blockdepth. This contribution incorporates a continuous shift to the eigenfrequency graph (Fig. 4.8a), but it does not cause a specific geometric combination to stand out and exhibit superior mechanical qualities.
The feet, as a link between membrane and substrate, may guide energy from the mode away to the substrate. A change in feet dimension might influence this energy loss of the membrane. The analysis of the graphs depicted in Fig. 4.9 precludes this. The absolute height of the feet does not appear to have a significant influence, neither on the eigenfrequency of the system, nor on the Q-factor. The effective mass does not depend on the feetwidth, since the moving part of the geometry is not changed. Whereas a change in feetdepth does change the effective mass since with increasing feetdepth the effective oscillating membrane is reduced in size.
All in all, the simulations provide insight into the influences of individual parameters on the mechanical mode. The presented mechanical structure provides a sturdy and robust system where slight variations in dimensions do not cause an outstanding mode drift. The simulations may be used to further improve the geometry of the structure. However, a specific combination of parameters with exceptional mechanical quality is not apparent. Thus, the geometry as described above in Sec. 4.1.3 is used for optomechanical experiments.

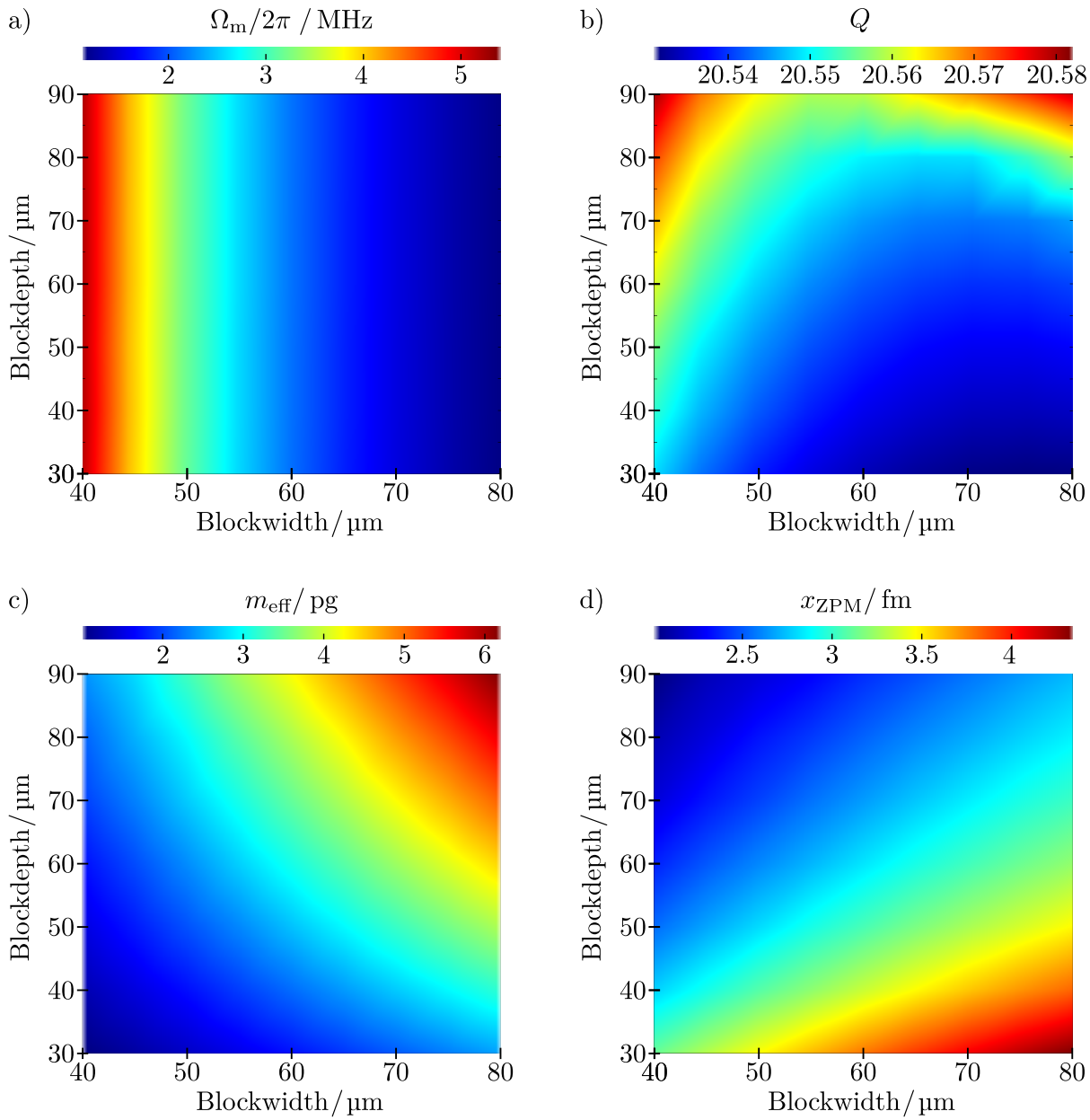

Figure 4.7: Results of a sweep of blockwidth and blockdepth. From the simulation, values for a) the eigenfrequency, b) the Q-factor, c) the effective mass, and d) the zero-point motion are extracted. An increase in blockdepth does not appear to influence the eigenfrequency (in contrast to the blockwidth), but it adds mass to the mode. This also affects the zero-point motion. However, there is no obvious local maximum or minimum that would suggest a particularly suitable parameter combination for high mechanical quality.

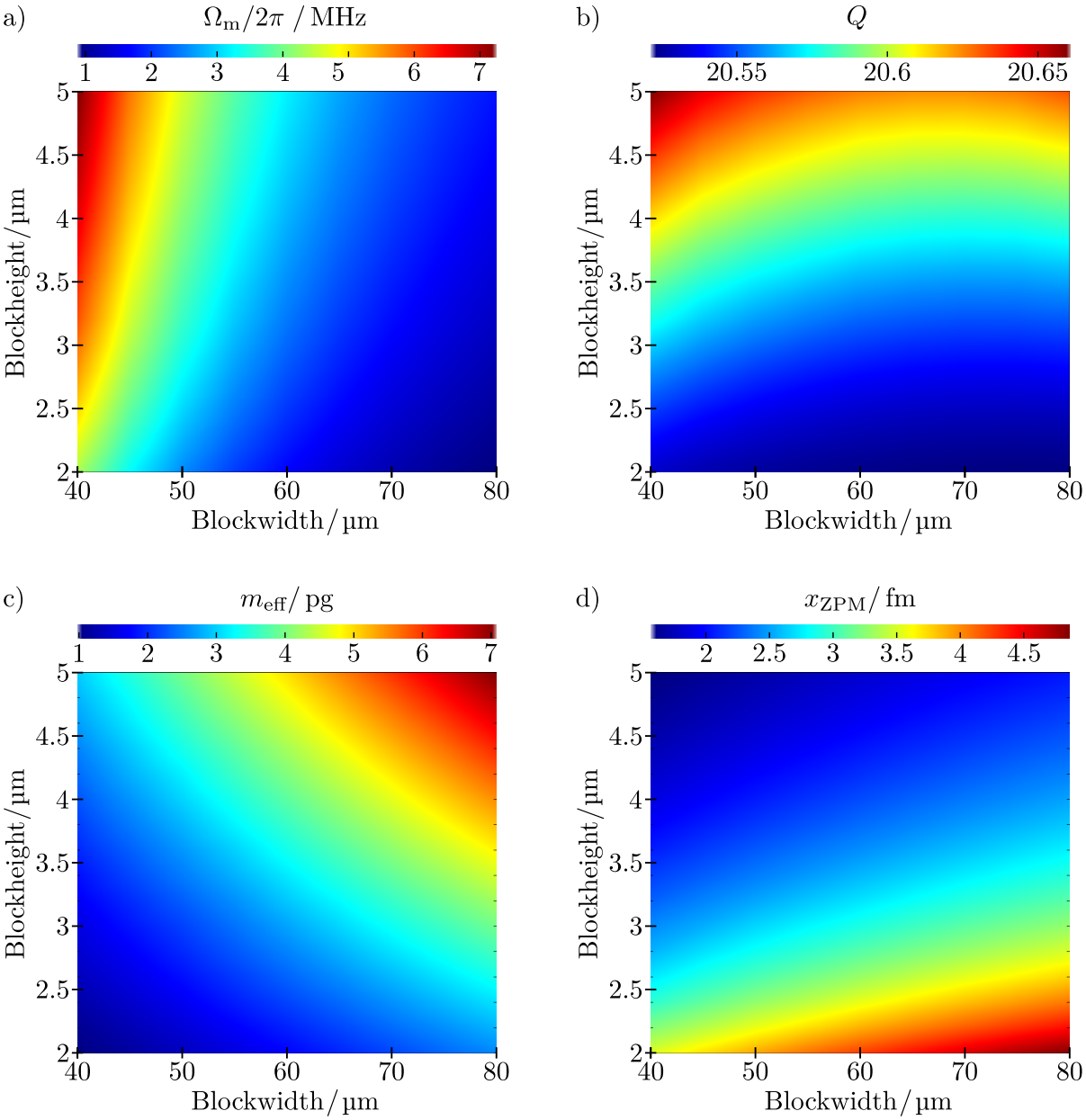

Figure 4.8: Results of a sweep of blockwidth and blockheight. The blockheight has a more significant influence on the mechanical mode than the previously investigated blockdepth. However, just as in the previous sweep, no particular combination stands out.

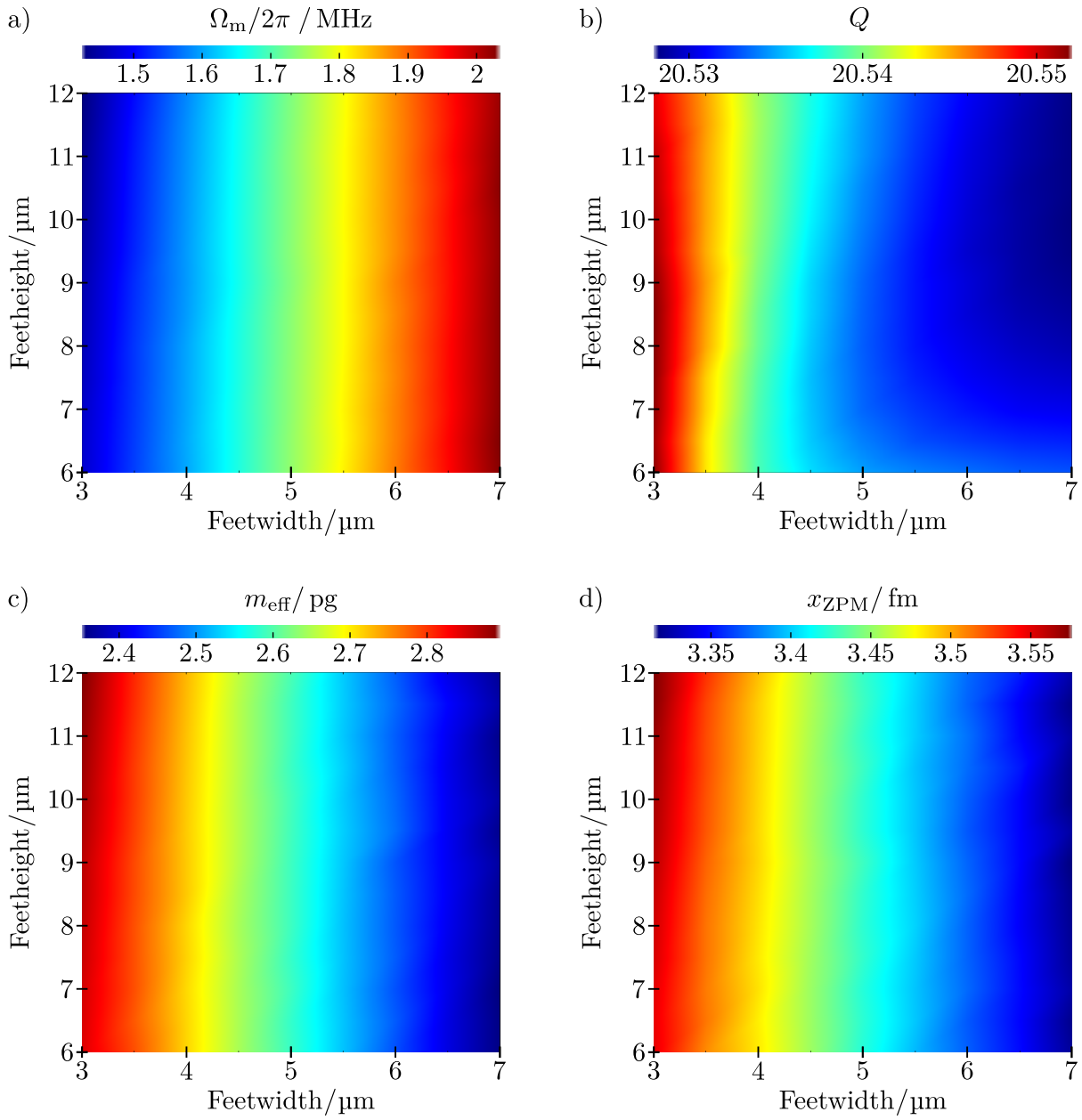

Figure 4.9: Results of a sweep of feetwidth and feetheight. There is no effect of the feetheight on the mechanical mode which suggests that the energy losses of the mode to the substrate are extremely low.

4.2 Fiber Preparation

In order to obtain a superb cavity performance, it is crucial to rely on a process that results in high-quality mirrors. The fibers used in this experiment are processed in-house, in the scope of the Bonn Fiber Lab, before they are sent to an external company (Layertec GmbH) for applying a high reflective coating serving as distributed Bragg reflector (DBR).

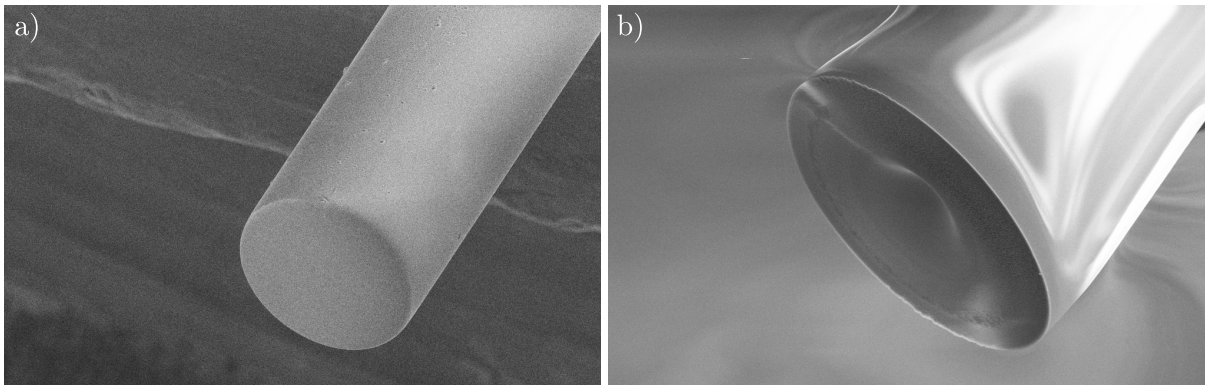

Figure 4.10: a) Electron micrograph of a cleaved fiber endfacet. To prevent charge accumulation, the fiber has been coated with a thin layer of copper. b) Electron micrograph of a fiber after the shooting procedure. Here, no conductive coating was applied, thus the image suffers from distortion due to charge accumulation. In both cases, the tilted view would make a scale bar misleading. For scale, the diameter of the fibers is 125 µm.

Fiber Shooting The cladding of a 780 nm single-mode fiber is stripped off. Since the fibers have a cladding made from copper, it is removed from the unprocessed fiber in a bath of $FeCl_3$. A manual cleaver (Fitel S324, The Furukawa Electric Co. Ltd.) is used for a clean cut of the fiber. The result can be seen in Fig. 4.10a. The fiber is then mounted in a shooting setup that can be used to pattern the topology of the fiber endfacet using a high-power laser: The light of a CO_2-laser ($P = 17$ W, $\lambda = 9.3$ µm) passes through an acousto-optic modulator to optimize the beam profile and to create short pulses from the continuous wave laser. The beam profile and its stability are further improved by additional optical components, monitored and controlled by a photodetector and a feedback loop. The fiber that shall be processed is made of SiO_2, which has a strong absorption band in the wavelength regime of $9 - 9.5$ µm. This can be attributed to the excitation of vibrational resonances of a $Si - O - Si$-group [110]. Thus, the impinging laser power is mostly absorbed by the material, which leads to local heating. The material is ablated and accumulates around the shot position. To machine a fiber end for applications as mirror surface in cavity experiments, a precise and well-controlled procedure needs to be applied. For small radii of curvature, one single shot is applied, while multiple shots are combined in an elaborate procedure for larger radii of curvature. An interferometric setup gathers information about the topography of the machined fiber or substrate and serves for monitoring and evaluating the process [65, 111, 112].
This method can produce radii of the indentation in the order of 100 to 500 µm and beyond. However, the usable area of the indentation on the fiber itself amounts to $20-45$ µm. Figure 4.10b

depicts the exemplary result of the fiber shooting procedure. Aiming for larger manipulated surfaces, the finite size of the fiber limits the results: For shots close to the fiber's edge, the material distribution can not be approximated to be isotropic and thus the properties of temperature conductance change. As a result, the indentation becomes asymmetric. This outcome is not yet considered by the current software controlling the shooting process. For further information, refer to [39, 65, 111, 112].

Fiber Coating The machined fibers are sent to a coating company to be equipped with several layers serving as a DBR. The alternating layers each feature a thickness of $\lambda/4$ of the experiment's wavelength of 780 nm. Depending on the number of layers, different reflectivities can be achieved. The flat half-inch substrates obtain a transmission of 10 ppm (ten parts per million), corresponding to a reflectivity of 99.999%, while the fibers are equipped with a transmission of 2000 ppm (99.8% reflectivity), each for the wavelength regime between 750 nm and 805 nm.

Printing Next, the polymeric structure is applied to either a flat substrate or on top of a machined fiber, depending on the application one is aiming for. For optomechanical experiments in a fiber-fiber cavity, one fiber is equipped with an optomechanical structure, while the other fiber serves as a bare fiber mirror. In a semi-hemispherical setup, the polymeric structure is typically applied on the flat substrate since this allows the fabrication of multiple structures in one printing process, compare Sec. 3.
The photoresist used is IP-S, which features in its polymerized state a refractive index of around 1.505 at a wavelength of 780 nm and a transmission rate larger than 90% [113, 114]. The relevant membrane part was printed at a laserpower of 22% (corresponding to 11 mW) at a scanspeed of 50 µm/s, while the legs of the structure (or in the case of a drum-shaped structure, the legs and the frame) were patterned coarsely. For the membrane, the hatching distance is reduced to 62.5 nm, and the layers of the wood-pile structure are separated by a slicing distance of 263 nm. For the development of the structure, it was immersed in a bath of the organic solvent PGMEA for 30 min and subsequently in isopropyl alcohol for another 30 min. In a post-curing step, the substrate was immersed in isopropyl alcohol and flood-exposed by a 6 W UV lamp. According to the description in Sec. 3.6, a plasma ashing process is applied and helps to further increase the surface quality.

Ferrule Assembly Typically, the fibers that are subject to the aforementioned procedure, including shooting, coating, and printing, have a length of less than 40 cm. For the usage of these fiber pieces in the experimental setup, they need to be optically connected. In practice, the termination of an optical fiber via an FC/APC connector features a lot of advantages, e.g., the easy in- and outcoupling due to standardized holders and the protection of the fiber end. Here, the machined fiber piece is spliced to a commercially available fiber, which is equipped with an FC/APC connector. Therefore, the cladding of the fibers must be removed on the ends that should be spliced. The commercially available and the manufactured fiber need to be cleaved, again using the manual cleaver. Next, they are inserted in a fusion splicer (FSM 100P+, Fujikura Ltd.), which uses a plasma arc to melt the material and merge the fibers. The splicer allows for a precise alignment of the fibers and monitors its performance: Light is coupled in through the

cladding, guided along the core through the splice, and then coupled out again. The occurring losses provide insight into the quality of the splice. A good splice shows losses in the order of 0.2 dB or less.[1]
In the following, the fiber tip is guided through a glass ferrule, which has an inner diameter of 131 µm and thus ensures stable positioning of the fiber. The fiber is mounted with its tip exiting the ferrule on a length of approximately 2 mm. The position is fixed via UV-sensitive epoxy glue: Outside of the ferrule, the glue is applied in a rear part the fiber and connects it to a shear piezo. Applying a voltage, this piezo actuator allows for a linear movement since the ferrule prevents a movement in any other direction. Thus, modulation of the piezo voltage results in a varying cavity length. The finished assembly can be inserted in an optical setup to examine the quality of the fiber mirror.

Fiber Mirror Characterization The light of a tunable continuous wave laser (here driven at a wavelength of 780 nm) is passing through a half-wave plate and a polarizing beam splitter (PBS), compare Fig. 4.11. The half-wave plate is adjusted for the maximal transmission straight through the PBS, while the remaining part is deflected into a beam dump. Behind the PBS, a half-wave plate and a quarter-wave plate follow, which are relevant for the setup as a reflection measurement: Using those, the back-reflected beam from the cavity can be distinguished from the incident beam via the PBS and choosing a cross-polarization arrangement. The incident light is coupled to the fiber, which is spliced to the manufactured fiber mirror. This mirror builds a semi-hemispherical cavity with an opposing mirror substrate. As mentioned above, the fiber position can be modulated along the cavity axis. Here, a signal generator is used to drive the piezo actuator with a triangular voltage signal, which translates to a steady back-and-forth movement of the fiber with constant velocity (assuming to operate the piezo in the range where its translation correlates linearly to the applied voltage). The light coupled out from the cavity passes the spliced fiber again and follows its path back to the PBS, where it is deflected due to the rotation of its polarization via the wave plate assembly. The intensity of the reflected beam can be monitored in the remaining arm of the PBS setup via a photodiode.
While scanning across the cavity length, the cavity resonance condition $L = N \cdot \lambda/2$ is fulfilled for specific lengths L. These resonances show up in the reflection spectrum of the cavity since for those geometries the energy is mostly present in the cavity, and only a minor part leaks out compared to the other configurations. As depicted in Subsec. 2.1.3, the reflection spectrum features a Lorentzian-shaped resonance dip with a dispersive component. The depth of the dip is a measure of the coupling strength of the light to the cavity and is thus used for the selection of a fiber mirror with a high-quality endfacet. The distance between two resonances resulting from the fundamental mode of the cavity directly corresponds to the so-called free spectral range $\nu_{\mathrm{FSR}} = c/2nL$. In our case, the refractive index n is assumed to be equal to 1. Combined with the full width half maximum of a fundamental mode resonance, one can calculate the finesse $\mathcal{F} = \nu_{\mathrm{FSR}}/\nu_{\mathrm{FWHM}}$, which is a characteristic magnitude of a cavity, illustrating how many roundtrups light can take before it is lost from the resonator. Hence, fabricated fiber mirrors can be checked with regard to their performance in cavities. If a fiber mirror proves useful, it is used as the platform to print a polymeric membrane on top.

[1] The manual of the splicer states that splices even in the order of 0.03 dB can be achieved for single-mode fibers. These values are not obtained in our applications, but still, the losses via the splice are negligible.

4.3 Measuring the Optomechanical Coupling Strength

In the following section, the optomechanical coupling strength of a fabricated structure shall be determined. First, the optical setup used is described. We take a closer look at a method to mount an FFPC in a cryostatic environment since we aim for measuring the temperature dependence of the mechanical properties. Next, the underlying relations between the measured quantities and the parameters to be determined are investigated.

4.3.1 Optical Setup

In general, the setup for determining the spectrum of the reflected power (which serves as access point for determining the optomechanical coupling strength) of a membrane-equipped cavity follows the setup which was described before for the fiber mirror characterization, but it features several modifications in details. A locking mechanism needs to be applied: In order to determine the optomechanical response, fluctuations in the cavity geometry that do not arise from the coupling shall strictly be eliminated. Therefore, a locking scheme as described in Sec. 2.4 is applied. This allows for a regulation of the cavity length via the piezo actuator to compensate for long-term drifts and thus filters out low frequencies from the measurement of the reflection spectrum. For this purpose, a lockbox (or high-speed servo controller) is used, connected to the piezo actuator. In the following, the setup is described for usage with the PDH locking scheme. A tuneable (between 760 nm and 785 nm) continuous wave laser is coupled into a single-mode fiber that serves for improving the beam profile, compare Fig. 4.12. The beam passes through an EOM, which is connected to a signal generator. This setup allows for the addition of sidebands onto the laser frequency. As in the previously mentioned setup, the beam passes through a half-wave plate, a PBS, another half-wave plate, and a quarter-wave plate for the cross-polarization configuration of the reflection measurement. The light is coupled into the fiber that is spliced to the manufactured fiber piece. Again, the fiber is glued onto a shear piezo, so the length of the cavity can be precisely controlled. A ferrule provides stability, so only a movement along one axis is possible. The fiber mirror forms a cavity with a planar mirror, which is, this time, equipped with a polymeric structure. The light coupled out from the cavity and coupled back into the fiber is separated via the PBS and monitored using a photodiode. The signal of the photodiode is mixed with the signal that is used to create the sidebands on the incoming laser light, as described in Sec. 2.4. For retrieving the power spectrum, the signal is fed into an electrical spectrum analyzer (ESA).
If the cavity is assembled in the form of a FFPC, so both mirrors used are fiber mirrors, the spatial dimensions of the cavity become very compact. Implementing the FFPC further into a ferrule provides a setup with high sturdiness [41, 109]. The position of both fibers inside the ferrule can be adjusted by rotating the fiber around its axis and changing the cavity length to achieve the best resonance signal. The fibers are then glued into position with epoxy glue, which is, e.g., cured by UV illumination. This provides a monolithic and thus rigid and compact system, which can also be used in a space-limited environment, for example, a vacuum surrounding or a cryostat.

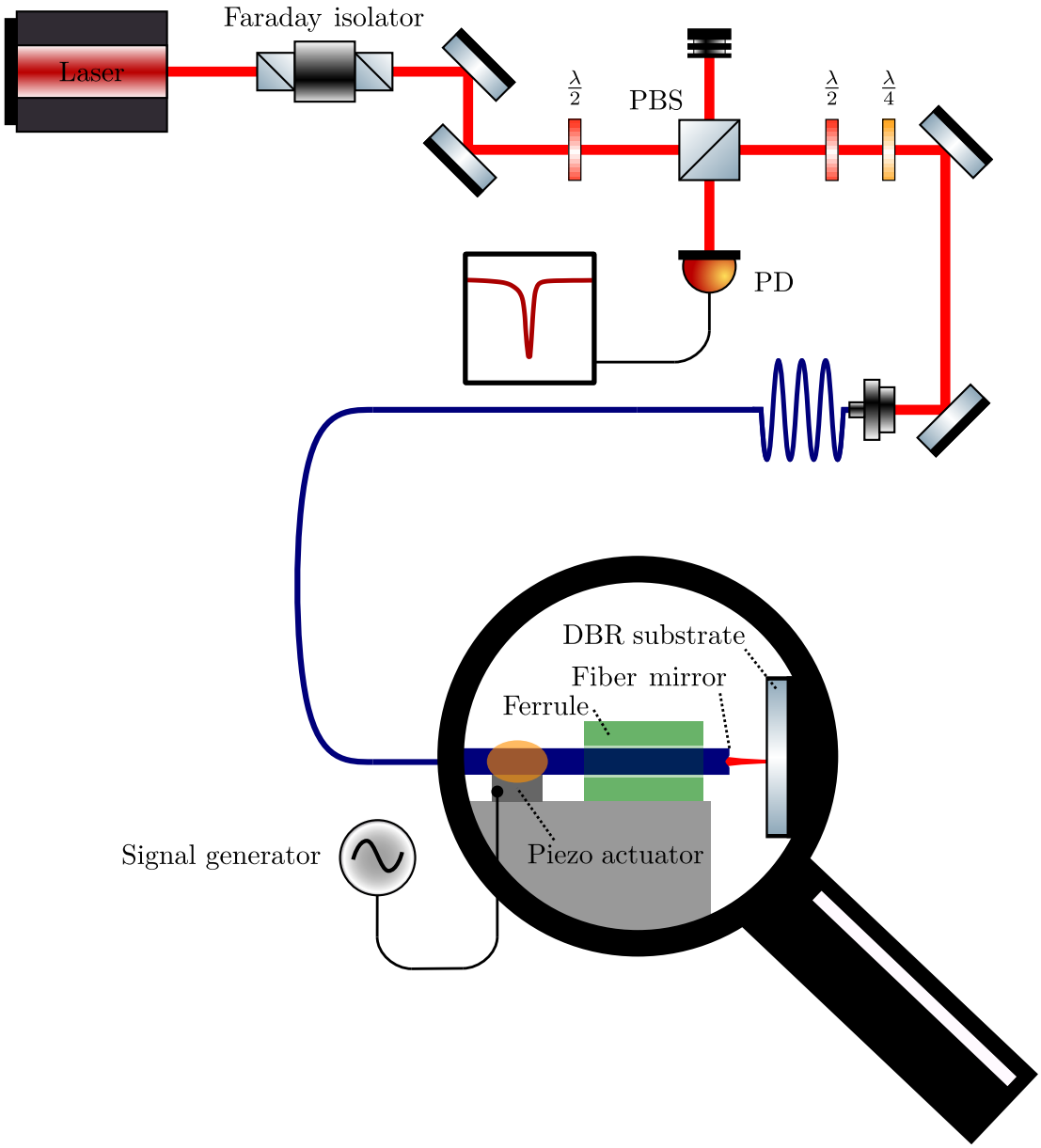

Figure 4.11: Setup for the characterization of the fabricated fiber mirrors. Laser light is coupled into the optical fiber leading to the cavity, which is in this case built from a flat substrate and the fiber mirror that is to be investigated. Via a combination of quarter- and half-wave plate and the usage of a polarizing beam splitter, the reflected light from the cavity is guided to a photodiode. This is used to monitor the reflection signal, which exhibits the characteristic dips (compare Subsec. 2.1.3), if the cavity length is continuously modulated. For the modulation, a signal generator tunes a piezo actuator in its linear regime using a triangular-shaped driving voltage.

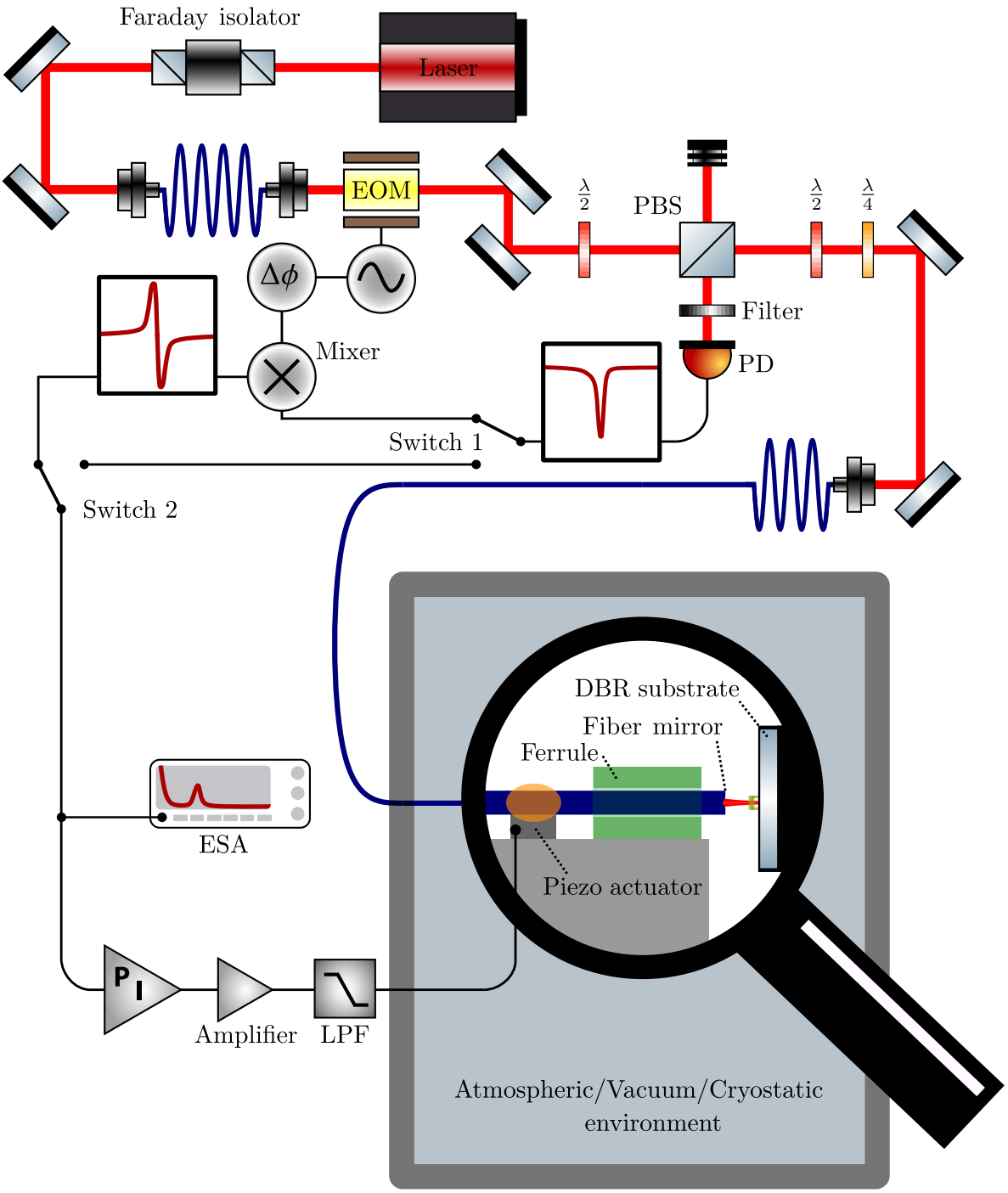

Figure 4.12: Experimental setup for the determination of the reflected power spectrum. The laser is tunable in between 760 nm and 785 nm. An EOM, connected to a function generator, creates sidebands onto the laser frequency, which are necessary for the PDH locking mechanism. Hence, the setup inhibits additional electronic components for the application of the locking scheme as presented in Sec. 2.4. The scheme also depicts the possibility of using side-of fringe-locking, when both signal path switches 1 and 2 are flicked, and the reflection signal is guided directly to the components of the lockbox. The power spectrum is retrieved via an ESA. From this, information about the optomechanical coupling strength can be deduced.

4.3.2 Cryostatic Environment

In order to examine the cavity at low temperatures, it can be inserted into a cryostat. The continuous-flow cryostat (Konti-Cryostat-Mikro, CryoVac GmbH & Co. KG) is made up of a stainless steel enclosure that forms a chamber featuring a holder for a sample inside. The chamber is closed by a lid, which is held into position due to a pressure difference on both of its sides. For the installation of the fiber cavity, a lid is manipulated to allow for guiding the optical fiber and the electrical connections for the piezo actuator into the chamber. Thus, a Swagelok fitting is inserted into a hole that was bored into the lid. The fitting is glued into position. A cone made from polytetrafluoroethylene (PTFE, commonly known as Teflon) is inserted. It features a feedthrough channel for the fiber. When the fiber is in position, the fitting can be torqued so the gap between the fiber and the PTFE cone is closed by the deformation of the cone. This provides a sealed assembly. For the electrical connections, the bored holes are sealed with silver glue. The space inside the cryostat, as well as the possibility to align the cavity once it is mounted inside, are very limited. Hence, an FFPC setup inside a rigid ferrule is used for the experiments: Two fiber mirrors are glued into position inside the ceramic ferrule, which is then inserted into the cryostat.
Due to the low temperatures that can be obtained inside the chamber, water from residual humid air would condensate and cover the inside of the chamber and the sample. Thus, the chamber needs to be evacuated. This is done with the help of a turbo-molecular vacuum pump (HiCube 80 Eco, Pfeiffer Vacuum GmbH). After a pumping period of approximately 3 hours the pressure reaches a value of $1 \cdot 10^{-5}$ mbar. To cool down the cavity, either liquid nitrogen ($T \sim 77\,\mathrm{K}$) or liquid helium ($T \sim 4\,\mathrm{K}$) is used. Using a pump (ME 4 NT, Vacuubrand GmbH & Co. KG), the liquid is pulled from its storage vessel through a piping system into the cryostat. Inside, it is pulled through a heat exchanger made out of brass and designed to hold the substrate. Here, the copper-coated fibers are clamped to the brass module to allow for a temperature transfer. The liquid is then guided outside the cryostat through a heated pipe, and either evaporates into the surroundings or, in the case of helium, is guided back to the helium liquefaction. The process is driven by a controller (TIC 500, CryoVac GmbH & Co. KG), which gathers information from a temperature sensor sitting in the heat exchanger in the cryostat. The controller regulates the flow of the coolant with a valve. There is also the option to switch on a heating mechanism inside the cryostat for temperature stabilization. However, the temperature of the ferrule assembly itself is not accessible since the sensor only measures the temperature of the heat exchanger module. A waiting time in the order of at least two hours should provide a stable temperature distribution.

4.3.3 Retrieving the Optomechanical Coupling Strength from the Reflection Spectrum

In the experiment, the accessible measurand for the optomechanical interaction is the signal sent to the ESA. The ESA decomposes the retrieved signal and splits it up into its constituting frequency components, displaying the respective powers present at each frequency. To gain information about the optomechanical coupling strength from this so-called power spectral density, we investigate the underlying process that forms the signal.

In the experiment, the mechanical mode is subject to thermal excitation via its surrounding at temperature T. According to [115, 116], this is expressed in the spectral density of the displacement fluctuations $\mathcal{S}_{xx}(\omega)$ as

$$\mathcal{S}_{xx}(\omega) \approx \frac{1}{m_{\text{eff}}} \frac{2\Gamma k_B T}{(\omega^2 - \Omega_{\text{m}}^2)^2 + \Gamma^2 \omega^2}. \tag{4.8}$$

Here, Ω_{m} denotes the (fundamental) mechanical resonance frequency, $\Gamma/2\pi$ its mechanical linewidth, k_B Boltzmann constant, and m_{eff} the effective mass as known from Sec. 2.2.
Due to the coupling to the optical mode, the thermally excited mechanical motion causes frequency noise on the optical mode [116]:

$$\mathcal{S}_{\omega_{\text{cav}}\omega_{\text{cav}}}(\omega) = \left(G^{(1)}\right)^2 \mathcal{S}_{xx}(\omega), \tag{4.9}$$

with ω_{cav} being the optical cavity resonance frequency. Rearranging this with respect to the frequency noise given as $f = \omega/2\pi$ results in [41, 66, 109]

$$\mathcal{S}_{\nu\nu}(f) = 2\frac{\mathcal{S}_{\omega_{\text{cav}}\omega_{\text{cav}}}(\omega)}{4\pi^2} \tag{4.10}$$

$$= \frac{2g_0^2}{4\pi^2} \frac{2\Omega_{\text{m}}}{\hbar} \frac{2\Gamma k_B T}{(\omega^2 - \Omega_{\text{m}}^2)^2 + \Gamma^2 \omega^2}. \tag{4.11}$$

Hence, the optomechanical coupling strength can be retrieved from the frequency noise power spectrum of the cavity: From the numerical simulations, the value of the effective mass m_{eff} is well-known. The (fundamental) mechanical resonance frequency Ω_{m} and the linewidth Γ can be extracted from the power spectrum. Measuring the total length of the cavity, the free spectral range is known and hence serves for calibration. With this, a fit to a resonance in the frequency spectrum provides access to the optomechanical coupling strength $|g_0|$ at the respective temperature T.

4.4 Comparative Measurements

In the following, we investigate the influence of different environmental settings on the mechanical resonance. For this purpose, drum-shaped polymeric structures are used as the mechanical system in the cavity. A variety of fabricated structures is shown in Fig 4.13, concerning both, a structure on a fiber as well as an array of structures on a substrate.
To get an idea about the effect that different environmental conditions may have on an optomechanical system, three measurements are compared: An FFPC cavity, equipped with a drum-shaped mechanical structure, is first exposed to atmospheric conditions and a measurement is performed. Next, it is put in a vacuum surrounding, and lastly in the cryostat. Each time, the thermal noise spectrum is measured upon stabilization of the cavity to extract information about the mechanical resonance. The results are depicted in Fig. 4.14.

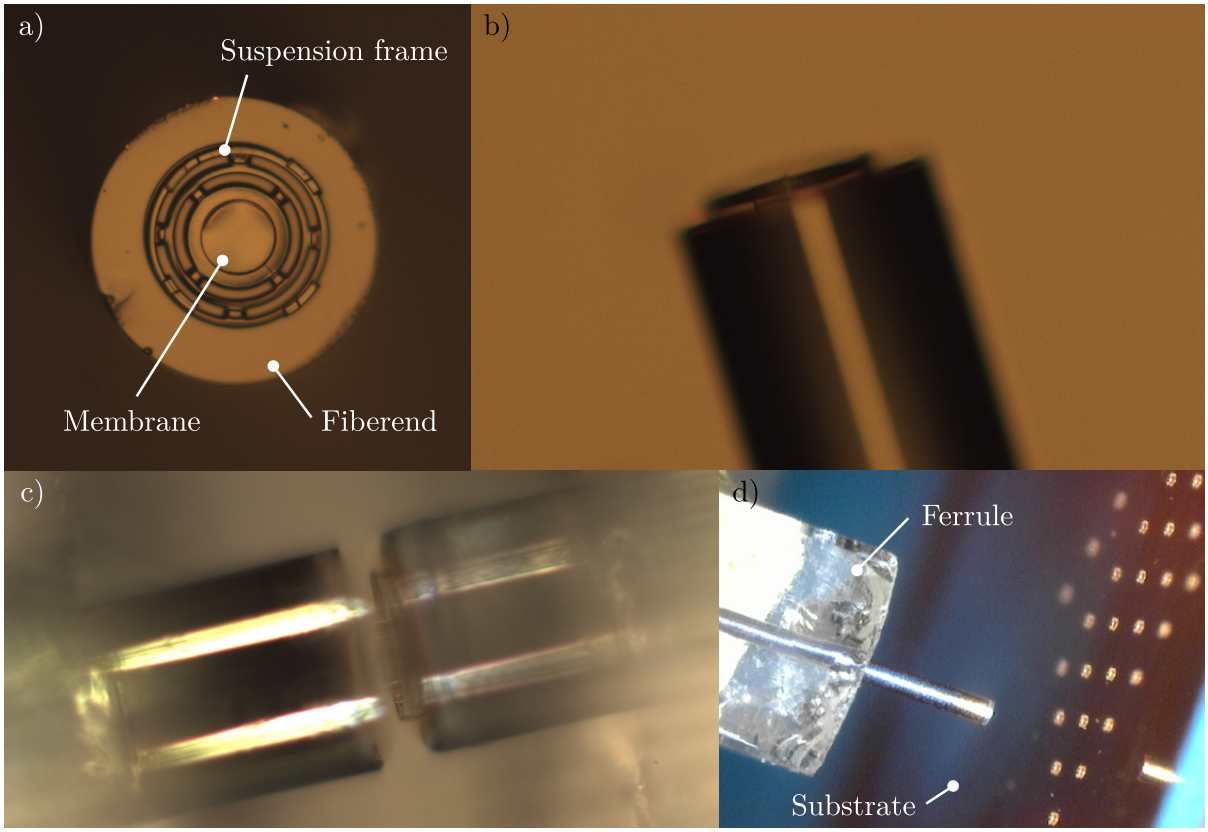

Figure 4.13: Drum-shaped structure that is used for the measurement of the optomechanical coupling (map), as well as for the investigation of the optical spring effect. Located in the center of the structure is the membrane, whose fabrication process was adjusted to yield for superb optical properties. It is suspended from a frame to decouple the membrane from the underlying structure to which the frame is connected via its feet. Part a) and b) show the structure fabricated on a fiber endfacet. Such an equipped fiber can be used to build a fiber-fiber cavity, gaining stability by the implementation into a ferrule, as depicted in c). For a semi-hemispherical cavity geometry, the structure is printed onto a flat mirror, which is then approached by a blank fiber mirror, as depicted in d). Here, the advantages and disadvantages of the respective setup become evident: The substrate allows for the fabrication of a whole array of structures simplifying, e.g., the realization of a parameter sweep. Simultaneously, the cavity setup has an increased size without the help of a hosting ferrule, so it is less rigid and less compact than the fiber-fiber cavity. c) and d): Image courtesy of Lukas Tenbrake.

In lab conditions ($T = 293\,\mathrm{K}$, $p = 1013\,\mathrm{mbar}$), the extracted frequency of the mechanical mode is located around 1.39 MHz, featuring a linewidth of 141 kHz. Applying vacuum conditions ($T = 293\,\mathrm{K}$, $p = 1\,\mathrm{e}^{-6}\,\mathrm{mbar}$) shift the frequency to lower values at around 1.32 MHz and additionally strongly reduces the linewidth to 61 kHz. In a liquid-nitrogen-cooled environment ($T = 77\,\mathrm{K}$, $p = 1\mathrm{e}^{-5}\,\mathrm{mbar}$), the resonance frequency is shifted towards higher values at around 1.54 MHz in combination with an even further reduced linewidth of 22 kHz. The amplitude of the depicted spectra is normalized to comply with each other.

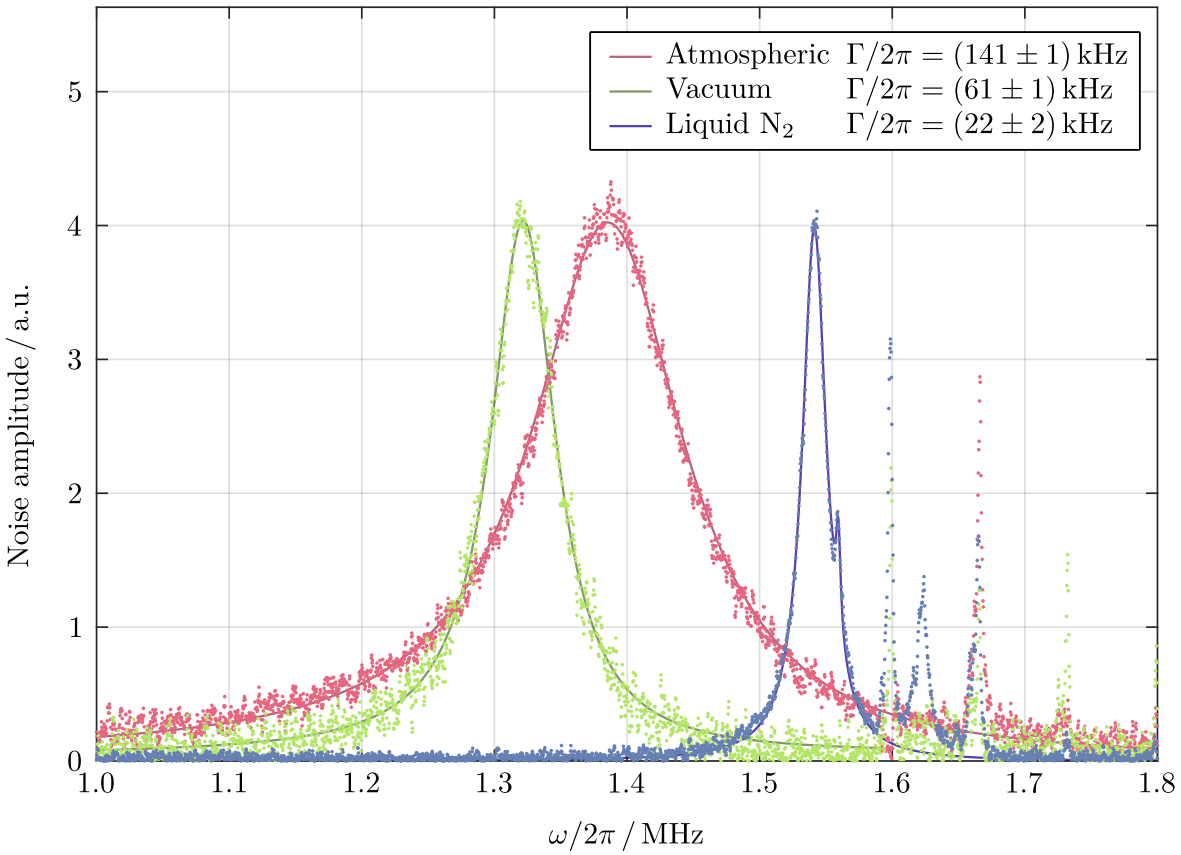

Figure 4.14: Measured mechanical resonances for an FFPC setup equipped with a drum-shaped polymeric structure at different environmental conditions. The dependence of resonance frequency and linewidth on the surrounding can be understood in the context of loss channels and temperature-dependent mechanical properties of the polymeric structure. The measurement was performed together with Lukas Tenbrake.

These results can be understood in the context of reduced damping via vacuum and an increase in stiffness of the polymeric structures at low temperatures, combined with reduced internal losses. As we move from the atmospheric environment to the vacuum environment, the reduced damping via collisions with air molecules allows for a narrower linewidth. Additionally, the resonance is shifted to lower frequencies. This result does not agree with the expectations since, intuitively, the resonance frequency should rather increase due to the reduced damping. Moving on toward the cryogenic environment further reduces the linewidth since internal processes in the polymer reduce the number of possible loss channels. Simultaneously, the resonance frequency is changed due to the increased stiffness of the polymer at low temperatures. Those processes are reviewed quantitatively in the following section. For this purpose, the cryostat is additionally operated with liquid helium to obtain even lower temperatures of $T = 4$ K.

4.5 Temperature-Dependent Mechanics

At atmospheric conditions, losses of the system either result from a damping of the mechanical oscillation via the ambient air, internal damping of the polymeric structure, or losses of the mode into the supporting substrate. The contribution of the latter is negligible due to the sound impedance mismatch between the polymer and the substrate, see Sec. 4.1. The two first-mentioned loss channels can be strongly reduced by transferring the setup into a cryogenic environment. This intrinsically comprises an evacuated chamber, dropping the losses caused by the interplay of the oscillation with air molecules. In the course of cooling down, the physical properties of the polymeric structure experience one or more strong transformations [117], for example changes in the conformation of the molecules or reduced/enhanced mobility in the molecule due to glass transitions. It should be noted that the observed behaviour is strongly dependent on the polymer used, so it may vary between resists [118, 119]. These temperature-dependent effects may be used here for the improvement of the structure's mechanical quality, reducing internal losses. Therefore, the temperature-dependent resonance frequency and linewidth are investigated.
The temperature-dependent mechanics are measured utilizing a bridge-shaped geometry of the polymeric structure, as presented in Subsec. 4.1.3. Figure 4.15 presents the fabricated design and the assembly of a cavity utilizing a DBR substrate or a fiber-fiber cavity. In order to operate a cavity in a cryostatic environment, a fiber Fabry–Pérot cavity, depicted in Fig. 4.15c, is used. Via assembly in a ferrule, the FFPC becomes robust and compact as it provides a monolithic setup. Due to its small form factor, it can be implemented in a cryostat, whose lid has been manipulated to feature feedthroughs for the optical fiber and electrical connections of the piezo actuator driving the length of the cavity.
Via usage of liquid helium as coolant the heat exchanger holding the FFPC assembly and hosting a temperature sensor is cooled to 4 K. An integrated heating coil allows to adjust the temperature of the heat exchanger: A controller regulates the heating current and the flow of the coolant. In this manner, the temperature is increased stepwise between 4 K and $\sim$ 300 K, with a step size of $\sim$ 10 K. At each step, a waiting time of 10 min assures a uniform temperature distribution of the FFPC. The spectrum of the FFPC is recorded and the fit to the mechanical resonance reveals the temperature-dependent shift of the mechanical resonance frequency, see Fig. 4.16a: The cooling alters the mechanical resonance frequency from 3 MHz to 3.5 MHz.
Simultaneously, the plot of the mechanical linewidth depicts a strong temperature dependence, see Fig. 4.16b: The linewidth reduces from $\Gamma/2\pi = 150\,\mathrm{kHz}$ at atmospheric conditions to $\Gamma/2\pi = 6\,\mathrm{kHz}$ at a sensor temperature of 4 K. In addition, the Q-factors for selected data points are given in the graph of Fig. 4.16b. At the lowest obtained temperature ($T_{\mathrm{sensor}} = 4\,\mathrm{K}$), the mechanical quality factor reaches a value of $Q = 590$, while it is $Q = 20$ for the atmospheric case, illustrating the strong increase in mechanical quality.
Thus, the internal structure of the polymer seems to undergo a process affecting its mechanical properties and increasing its stiffness. Glass transitions influence various properties of a polymeric compound as the internal composition of molecules obtains mobility due to the transition. Following the description given in [117], the mechanical damping is strongly affected by the phase change processes that occur during a glass transition process. In addition, the specific heat of polymers is drastically reduced at low temperatures [117]. Thus, phonons only

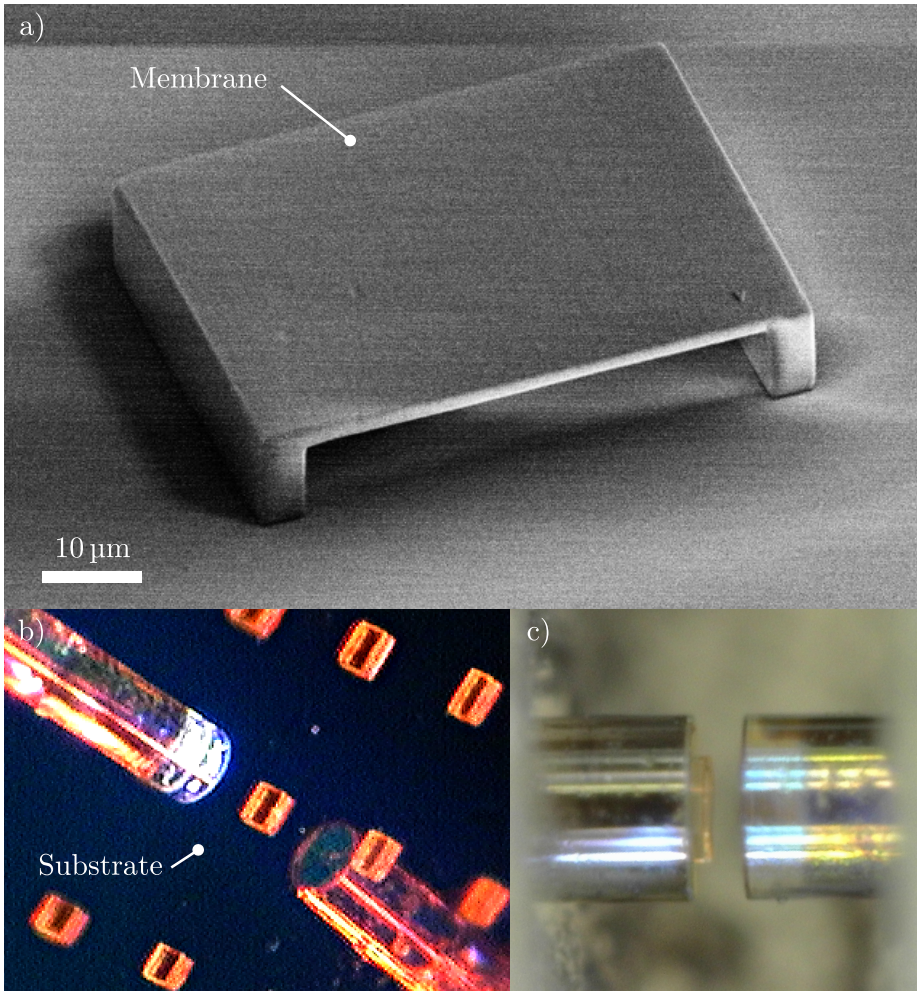

Figure 4.15: Fabricated bridge-shaped polymeric structures. a) The electron micrograph depicts the dimensions of the membrane. The membrane on top has a size of 45 µm × 60 µm, supported by two feet each having a width of 5 µm. The thickness of the membrane is in the order of 3 µm, so several λ_0. The leg height is in the order of 7 µm to 10 µm. This structure is fabricated either on b) a DBR substrate or c) hosted in a fiber-fiber cavity. b) and c): Image courtesy of Lukas Tenbrake.

have a small energy, and only a few are activated. This reduces the number of energy loss channels. The review on the mechanical deformation behavior investigating the low-temperature regime [117] reveals that the Poisson's ratio of a polymer can be strongly influenced by the temperature. The interplay of these effects, and potentially more polychemical effects that are not investigated here, result in the strong improvement of the mechanical quality of the polymeric structure at low temperatures.

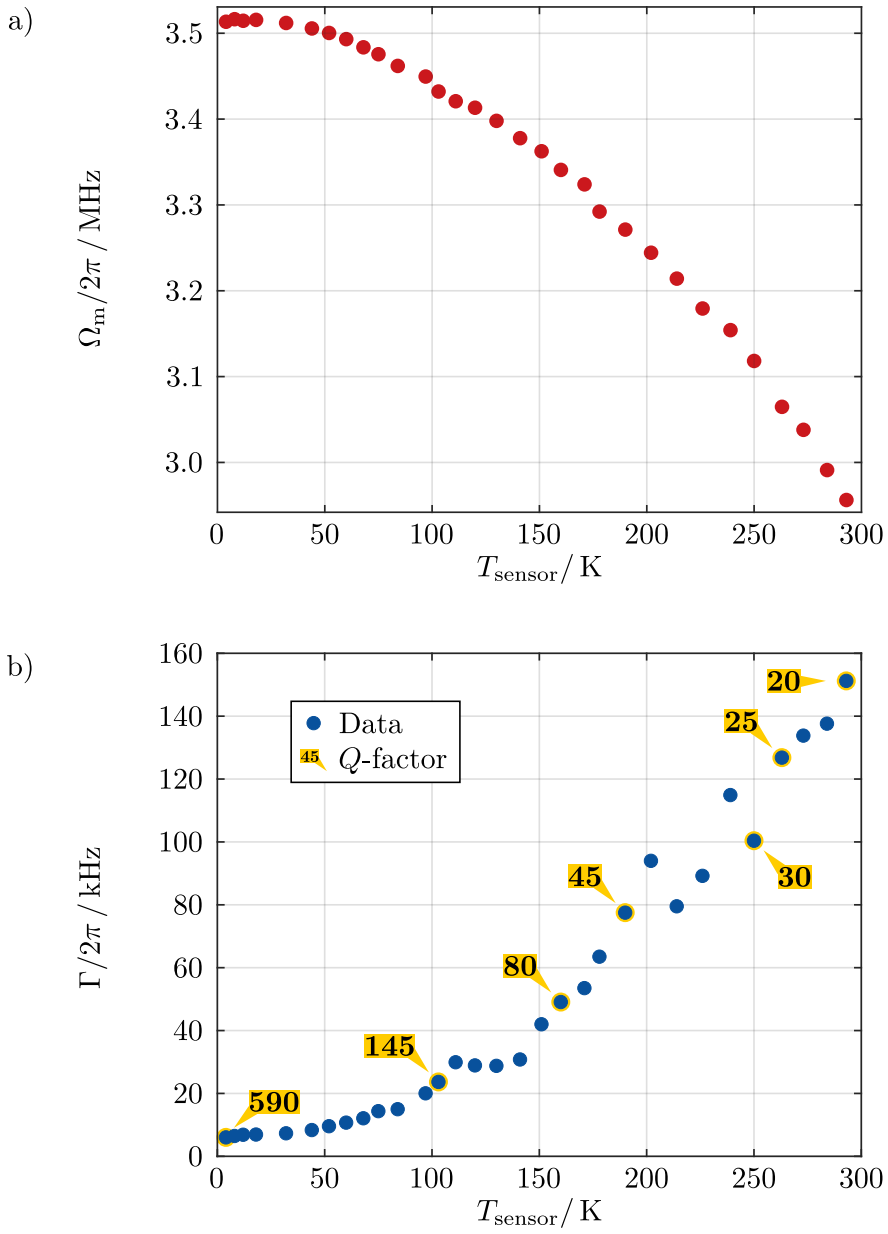

Figure 4.16: Temperature dependence of a) the mechanical resonance frequency and b) the linewidth, measured with a bridge-shaped mechanical structure in an FFPC setup, as depicted in Fig. 4.15c. The graph of the linewidth dependence also shows measured Q-factor values of the mechanical mode for selected data points, marked by yellow contours. The increase in resonance frequency and the corresponding decrease in linewidth when moving towards lower temperatures corresponds to the polymeric structure gaining stiffness. Jumps, which can be in particular be identified for the temperature dependence of the linewidth in b), may be attributed to transition effects that occur due to an internal rearrangement on the molecular scale, e.g., by passing over a glass transition point. The measurement was performed by Lukas Tenbrake, compare [104].

4.6 Mechanical Loss Channels

The experiments at cryogenic temperatures reveal higher mechanical quality factors compared to atmospheric measurements. Nevertheless, the quality factor is limited by an interplay of effects that cause energy to dissipate from the mechanical mode. Thermoelastic dissipation, as presented in [120], describes the occurrence of thermal currents in materials that emerge from induced strain in the course of thermal expansion. The strain gives rise to a temperature gradient, which provokes a thermal current and thus dissipates energy from the mechanical mode [121]. Further losses may arise due to structural deformation. Here, the actual losses strongly depend on the modal shape and the amount of strain that is involved.
The results of the FEM simulation, as depicted in Fig. 4.4a and 4.5a, show the dissipation of the stored energy to the underlying substrate. Even though the losses via this channel are already low in our setup, it should be mentioned that these can be adjusted by the number of legs, their length, or the width or number of cuts in the supporting structure of the membrane. Here, the so-called soft-clamping method [122, 123] can come into play. Thereby the structure's geometry is designed so that the supported mode is evanescently coupled to a clamping region, which features a phononic band gap and thus does not allow for the dissipation of modal energy [124].
Another approach to reduce the losses is the application of optimized materials. This covers the improvement of the material used as well as the application of different materials. In order to adjust the internal losses of the structure, a plasma ashing process can be applied that reduces the overall thickness of the membrane. Thus, the induced strain is reduced and results in lower thermoelastic dissipation (compare above).
Besides the material used, a variety of different photoresists exists [53, 125] and can be applied following the presented procedure. Furthermore, an even wider range of materials can be utilized, if the procedure is adjusted: The basis of the structure, a frame that is decoupled as much as possible from the substrate, could be fabricated via classical DLW, for example. This frame then serves as a platform for the attachment of a different material. One could think of, e.g., evaporating a metallic or dielectric layer[2] or stamping a mono or multilayer with the help of polydimethylsiloxane (PDMS) [126]. On the one hand, this procedure aims for the integration of materials that reveal lower internal losses and thus exhibit superb mechanical quality factors in the cavity. On the other hand, it allows for the integration of interesting types of materials and the examination of the interaction of those with the radiative field in the cavity.

4.7 Optomechanical Coupling Map

In Sec. 2.3 the optomechanical coupling map was presented, depicting the dependence of the frequency-pull parameter $G^{(1)}$ with the variation of the cavity geometry by the means of L_2/λ_0 and d/λ_0. To link this to the performed measurements, one possibility is the fabrication of a vast number of different structures with different geometric parameters. However, a whole line across the map can be probed with just a single structure: The geometrical dimensions of the structure itself are invariable, but the probe laser can be tuned in wavelength. Due to the scaling of the axes with $1/\lambda_0$, this corresponds to a diagonal cut through the map.

[2] This can be realized by utilizing a temporary membrane as basis for the evaporation process which is then dissolved or removed, e.g., via plasma ashing.

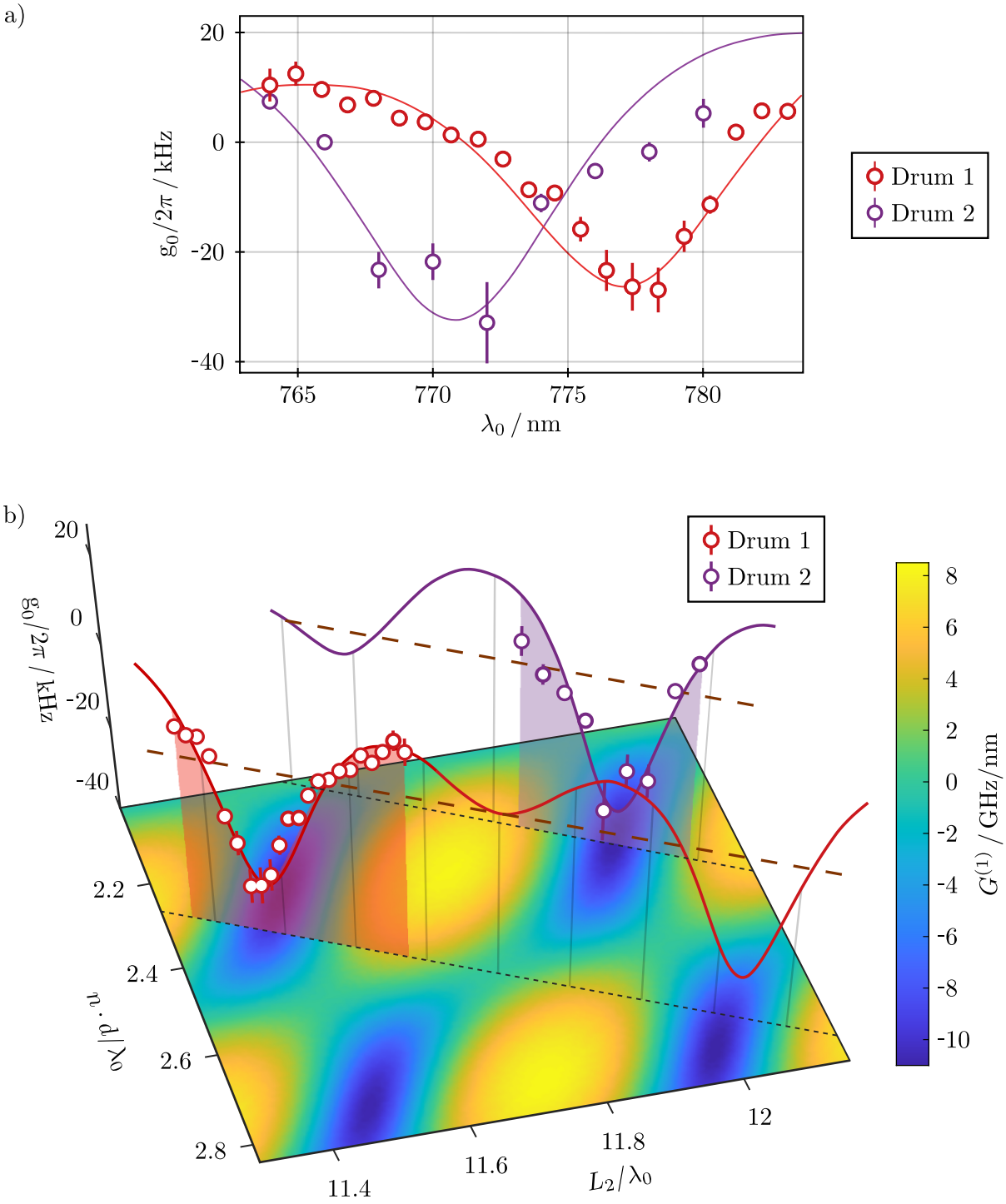

Figure 4.17: a) Measured optomechanical coupling strength $g_0/2\pi$ to the fundamental mechanical mode for two drums, observed at different wavelengths λ_0. A fit to a cut through the optomechanical coupling map, as presented in Sec. 2.3, is performed. b) Depiction of the optomechanical coupling map together with the data and fits from a). The baseline, corresponding to $g_0 = 0$, is highlighted in brown. The measurement was performed by Lukas Tenbrake, compare [104].

Here, two drum-shaped structures as presented in Fig. 4.13 are utilized. The dimensions of the drums are $d \approx 1.2\,\mu\text{m}$ and $L_2 \approx 8.9\,\mu\text{m}$ for drum 1 and $d \approx 1.15\,\mu\text{m}$ and $L_2 \approx 9.2\,\mu\text{m}$ for drum 2[3]. The structures are fabricated on top of a DBR substrate and are approached by a fiber mirror. The tunable laser is adjusted to wavelengths between 760 nm and 785 nm, which corresponds to an adjustment of the geometry in the order of $\mathcal{O}(100\,\text{nm})$. Each time, the spectrum of the cavity is recorded and the optomechanical coupling strength g_0 to the fundamental mode is extracted, following the aforementioned procedure. The results can be found in Fig. 4.17a. A fit, corresponding to a diagonal cut through the coupling map for a fixed λ_0, is then applied to the data points. The resulting fits for both drums are shown in Fig. 4.17a. Figure 4.17b depicts both, the data points and the experimentally found cuts through the coupling map. The retrieved data is in good agreement with the theoretical model, approving the underlying concept of optomechanical coupling. The sign of the coupling strength g_0 is retrieved from the fit to the coupling map, which features an asymmetric distribution of minima and maxima. We observe coupling strengths up to $|g_0|/2\pi \approx 30\,\text{kHz}$. The maximum coupling strength of $|g_0|/2\pi = (33 \pm 7)\,\text{kHz}$ is found for drum 2 at a wavelength of 772 nm. Upon comparison with Fig. 4.16b, it is found that the coupling strength exceeds the linewidth of the mechanical resonance in the cryogenic regime.

4.8 Optical Spring Effect

The optical spring effect describes the change of the mechanical resonance frequency in the optomechanical setup that arises due to radiation pressure transferred by the photons of the radiative mode [70, 127–129]. The effect is sometimes also called light-induced mechanical rigidity and is a pure optomechanical effect. In addition, we have to deal with a thermally-induced nonlinearity [130], induced due to the absorption of light in the cavity, mainly from the polymer. This causes an additional shift of the cavity resonance frequency.
For the determination of the effect in our optomechanical system, the experimental setup is extended and modified, see Fig. 4.18: In addition to the laser that is used to probe the mechanical resonance of the polymeric structure, the light of a second laser source is overlapped. While the probe laser is fixed at a wavelength of 780 nm, the second laser is used as pump laser and is tunable in the wavelength range between 760 nm and 785 nm. The overlap of both beams is realized via a PBS. A wave plate setup and an additional beam splitter allow for the separation of the reflected light from the cavity. A photodiode is used to monitor the reflected signal of the pump laser. The PDH setup and the monitoring of the reflection of the probe laser remain unaffected by the changes to the system. Again, the mechanical resonance frequency Ω_m is extracted from the spectral density $\mathcal{S}_{vv}(f)$ as presented in Subsec. 4.3.3. Here, the pump laser is set to a wavelength addressing a cavity resonance that is shifted by one free spectral range ($\approx 5\,\text{THz}$) from the resonance addressed by the probe laser. The experiment is performed with drum-shaped drums as depicted in Fig. 4.13 at atmospheric conditions.

[3] These values arise from the fit of the measured g_0 to the coupling map as presented in Fig. 4.17. Due to the periodicity of the map, the determination of the values cannot be exactly fixed, but are subject to a modulo operation with half the (material) wavelength.

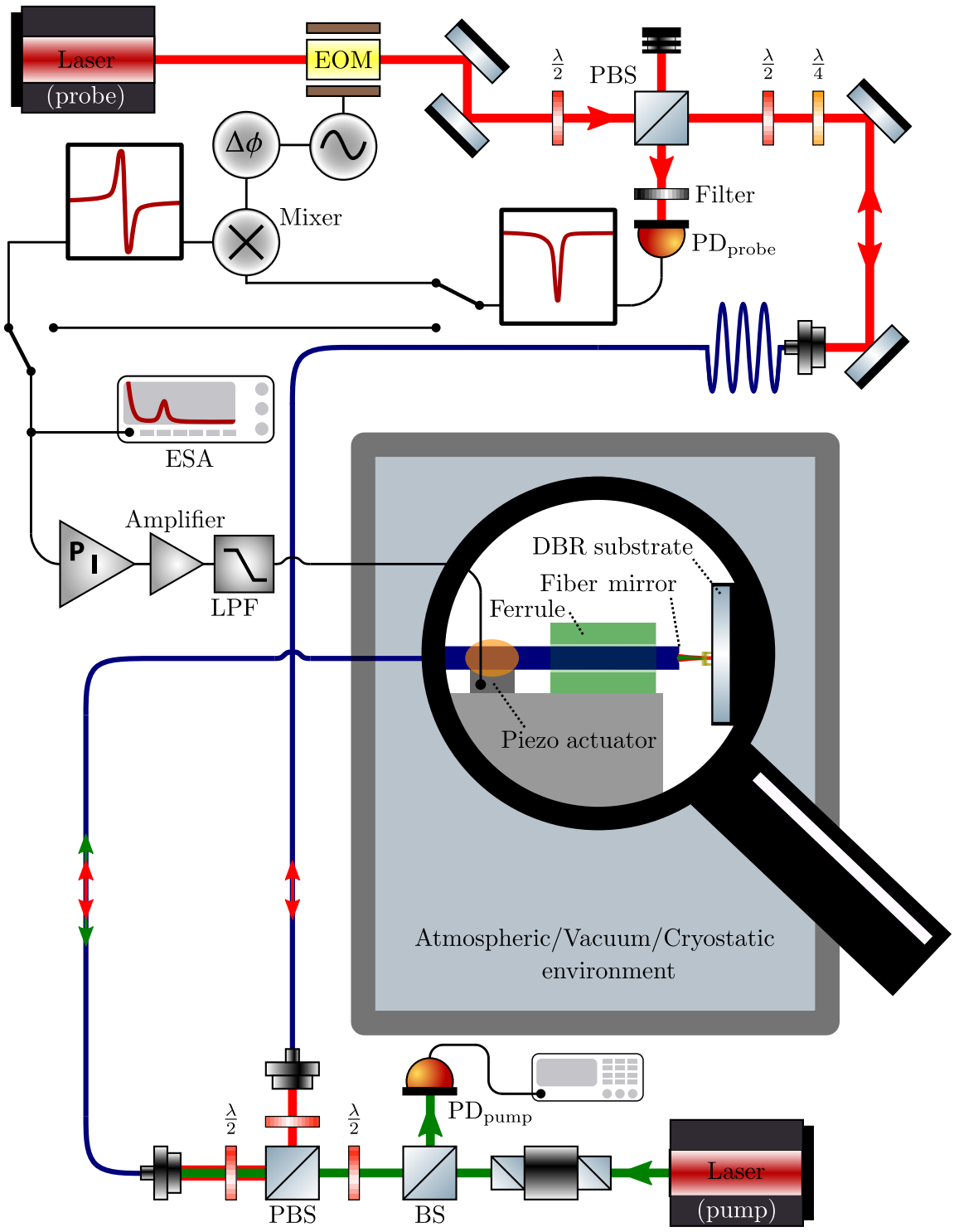

Figure 4.18: Experimental setup for the measurement of the optical spring effect. The setup from Fig. 4.12 is extended by the components depicted at the bottom: A wavelength- and power-tunable pump laser is superimposed to the beam of the probe laser. The pump laser is utilized to tune the mechanical response of the cavity. This time, colored arrows depict the paths of the beams to improve traceability.

In the following, the shift of the mechanical resonance frequency $\Delta\Omega_\mathrm{m}$ is investigated with respect to the cavity detuning Δ between pump and probe laser. In the Doppler regime, so if the cavity intensity decay rate $\kappa \gg \Omega_\mathrm{m}$, the shift can be expressed via

$$\Delta\Omega_\mathrm{m}(\Delta) = g_0^2 n_\mathrm{cav} \frac{2\Delta}{\frac{\kappa^2}{4} + \Delta^2}, \tag{4.12}$$

compare [33, 131, 132]. The factor n_cav indicates the cavity photon number. In the case considered here, effects on the mechanical linewidth are neglected, so amplification or cooling processes that can be achieved in the sideband-resolved regime as presented in Subsec. 2.2.1 do not come into play.

We are interested in the measurement of the mechanical resonance shift $\Delta\Omega_\mathrm{m}(\Delta)$ versus the detuning Δ. Hence, the wavelength of the pump laser is varied and scanned over the optical resonance ($\Delta = 0\,\mathrm{GHz}$). In this process, the cavity photon number is continuously modulated and thus the radiation pressure acting on the membrane varies.

Simultaneously, the spectral density $\mathcal{S}_{vv}(f)$ is recorded and the mechanical resonance frequency Ω_m is extracted. Figure 4.19a shows the results of the measurement of $\mathcal{S}_{vv}(f)$, normalized to the maximum observed $\mathcal{S}_{vv_\mathrm{max}}$, against the detuning at a pump input power of $P_\mathrm{in} = 6.8\,\mathrm{mW}$. A discontinuity in the frequency noise spectra, marked by the black dashed lines, can be observed and is attributed to the optical spring effect.

The resulting shift in the mechanical frequency at a pump laser power of $P_\mathrm{in} = 6.8\,\mathrm{mW}$ can be found in Fig. 4.19b. The same graph depicts the reflection signal of the pump power $P_{\mathrm{PD}_\mathrm{pump}}$ marked in red. This signal is decreasing with increasing detuning, corresponding to a growing number intra-cavity photons grows.

The measurement is repeated with different input pump powers P_in, as indicated by the legend depicted in the upper right corner of Fig. 4.19. Figure 4.19c and 4.19d show the observed shift in the mechanical resonance frequency and the measured reflection signal $P_{\mathrm{PD}_\mathrm{pump}}$ for the remaining powers.

Photothermal nonlinearity [133] causes a shift of the resonance frequency of the optical cavity, as apparent in Fig. 4.19c and 4.19d. The graphs illustrate how the nonlinear behaviour is increasing with ascending pump power, while for low powers the trace of $\Delta\Omega_\mathrm{m}$ merges more and more into a dispersive shape. According to [33], an optomechanical bistability of the structure can be excluded as source for this effect since g_0 and n_cav are not sufficiently large enough to cause such. Instead, the observed effect can be attributed to absorption at the interfaces of the polymeric structure since stronger nonlinearities occur in scenarios where the maximum intensity is located at the polymer's surface.

However, this effect is happening on longer timescales than the dynamics our investigation is aiming for. Hence, the introduction of a slow drift $\Delta' = \Delta - \alpha n_\mathrm{cav}$ can compensate for it. The introduced factor α is the photothermal frequency-pull factor. Following the input-output formalism, as presented in [134], the detuning Δ' is now inserted into the steady-state solution of the equation of motion of the averaged complex light-amplitude $\langle \hat{a} \rangle$ [33, 104]. What follows is a polynomial, cubic in n_cav:

$$0 = \alpha^2 n_\mathrm{cav}^3 - 2\Delta\alpha n_\mathrm{cav}^2 - \left(\Delta^2 - \frac{\kappa^2}{4}\right) n_\mathrm{cav} - \kappa_\mathrm{in} n_\mathrm{in}, \tag{4.13}$$

with n_{in} being the input photon number rate and κ_{in} being the cavity input coupling. From this, two stable and one unstable solution for n_{cav} are obtained. The stable solutions correspond to the two possible directions in which the detuning can be driven. The data points in Fig. 4.19b depict one branch of the solution, while the rest is marked with a dotted line: All measurements in Fig. 4.19 are obtained by scanning the pump laser from $\Delta < 0$ to $\Delta > 0$. Hence, the red data points show how the reflected signal is decreasing, so more and more photons populate the cavity. At the same time, the mechanical resonance frequency increases as a result of the present radiation pressure. The photothermal effect causes the cavity resonance to shift away from the pump laser frequency. At one point, the scan itself catches up with the drifting frequency so that further detuning does not increase the population of the cavity mode anymore but triggers a depletion of the cavity. Thus, the mechanical resonance frequency returns to the unperturbed value and the reflection signal of the cavity jumps back to its baseline.
To fit the data points, $n_{\mathrm{cav}}(\Delta)$ as retrieved from Eq. 4.13, is inserted in Eq. 4.12, where Δ is replaced with Δ' in order to compensate for the photothermal effect. The retrieved expression for $\Delta\Omega_{\mathrm{m}}(\Delta')$ is then used to numerically fit the data points.
We obtain a maximum frequency shift of $\Delta\Omega_{\mathrm{m}}/2\pi = 31\,\mathrm{kHz}$ for the maximum input pump power used $P_{\mathrm{in}} = 6.8\,\mathrm{mW}$. The photothermal frequency-pull factor α in this case amounts to $\alpha/2\pi = (8 \pm 2)\,\mathrm{kHz}$, while the finesse of the cavity can be estimated to 1400 ± 300. To increase the frequency shift even more, higher pump powers as well as the reduction of the photothermal effect, so improving the surface quality of the membrane, would help. Nevertheless, the presented shift of the mechanical resonance frequency already surpasses the mechanical linewidth of the fundamental mode at cryogenic conditions. This paves the way for tuning individual drums, e.g., in multimembrane setups.

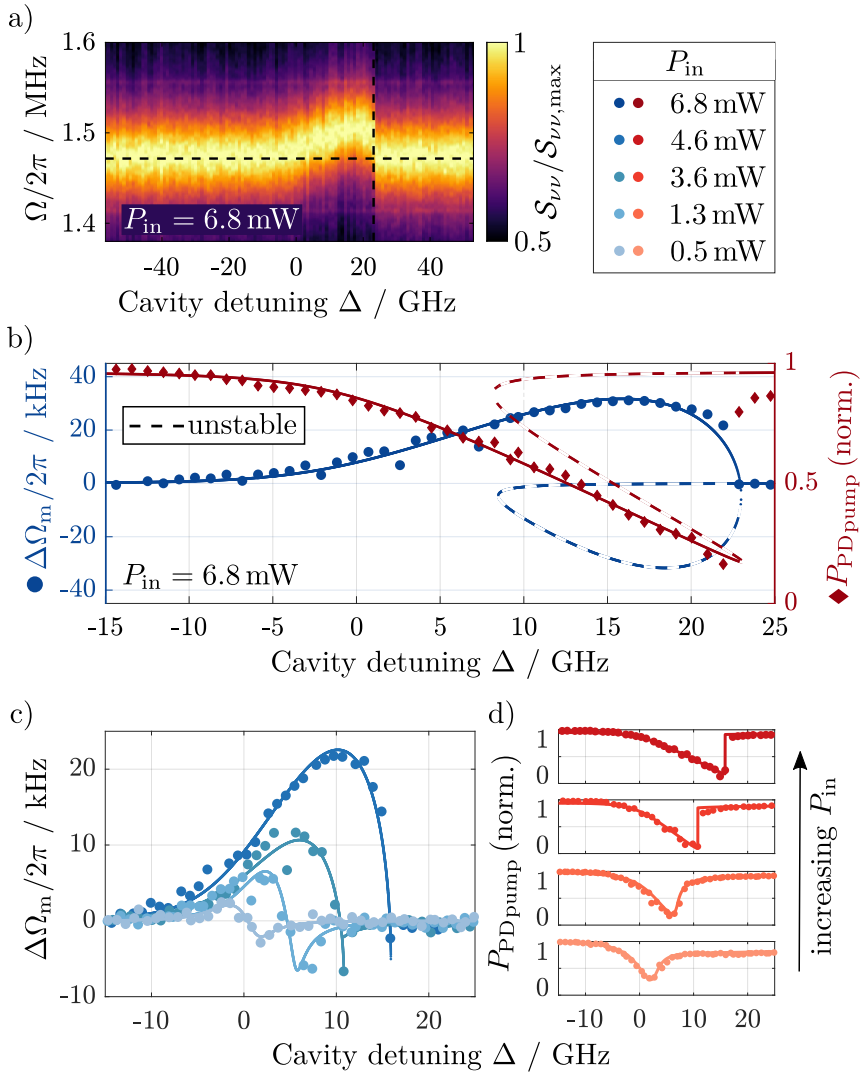

Figure 4.19: Results of the measurements of the optical spring effect with polymeric membranes. Graph a) exemplary shows the normalized retrieved frequency noise spectra, with an apparent effect of the optical spring. In b), c), and d), the dependence of the normalized reflection signal of the pump laser $P_{\mathrm{PD_{pump}}}$ as well as the determined mechanical resonance shift $\Delta\Omega_\mathrm{m}$ is depicted versus the detuning Δ between pump and probe laser. The dotted lines in graph b) correspond either to the unstable solution or the solution retrieved for the reversed scan direction from Eq. 4.13. The graphs c) and d) contain data points arising from different pump input powers, as depicted in the legend in the upper right. Graph c) shows how the trace of $\Delta\Omega_\mathrm{m}$ morphs more and more into a dispersive shape for low input powers. Graph d) depicts the power-dependence of the photothermal nonlinearity. The measurement was performed by Lukas Tenbrake, compare [104].

CHAPTER 5

Structured Metalization of Fibers

This chapter describes an approach to creating almost arbitrary two-dimensional metallic structures on optical fibers. The method chosen here involves the creation of a polymeric mask that is applied to a fiber. Thus, a shadow structure arises in a thermal evaporation process. After the removal of the polymer, the fiber retains its metallic pattern.
The design of the masks used to create structures on the end and side facets of optical fibers is the product of an iterative process. Several generations of designs resulted in the status depicted in this work. A brief overview of the design development is presented, starting with an approach that produces a single electrode on a fiber. Then, the fabrication of a fiber with four separate electrodes using two masks is presented. Finally, the fabrication procedure of an Ω-shaped antenna on top of a fiber is introduced. With the help of a direct laser written ferrule, we managed to connect to the two pads on the fiber with macroscopic wires.

Optical Fibers The following experiments are performed using a common single-mode fiber (780HP, Thorlabs Inc.). This single-mode fiber features the widely used characteristic cladding diameter of 125 µm. While the optical properties of the fiber are not of primary interest, the usage of fibers with standard geometrical dimensions ensures that results can be universally applied to a wide range of commercially available fibers. The coating of the fiber is completely stripped off, thus only bare SiO_2 remains. The fiber is cleaned with isopropanol and cleaved with a manual cleaver (Fitel S324, The Furukawa Electric Co. Ltd.).

5.1 Single Electrode

As a first approach, a polymeric structure is printed directly on top of a fiber. The mount capable of holding a fiber in position for the DLW printing process, as depicted in Fig. 3.1b, is used. The polymeric structure is composed of a flat circular disk, connected via six legs to the fiber endfacet, just like a table[1]. The structure's purpose is the protection of the fiber core and its nearest surrounding during the following evaporation procedure. Thus, the in- and outcoupling

[1] Flat drum-like structures were introduced at the beginning of Ch. 4 and were discussed as optomechanical structure.

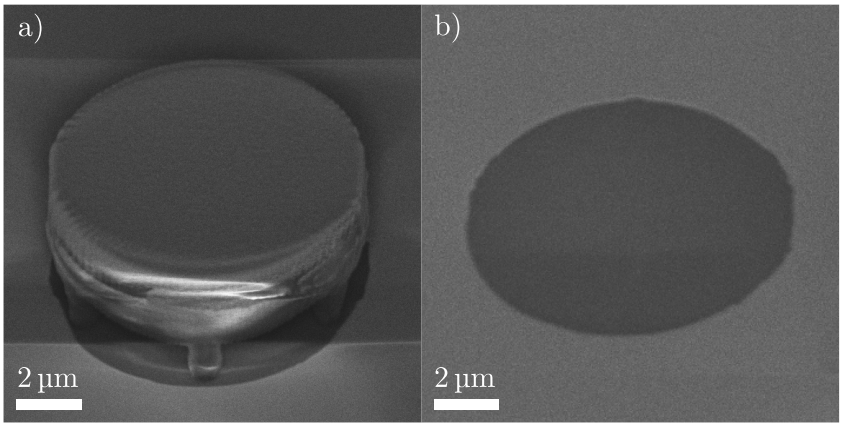

Figure 5.1: Polymeric structure on top of a flat glass substrate. a) The structure is composed of six feet with a disk on top. b) After an evaporation process, the substrate is put into an ultrasonic bath to remove the polymeric structure. Here, the lift-off process worked successfully and reveals the created shade in the metallic film. Due to the tilted viewing angle, the scale bar only serves as a rough guide for the eye.

of light would still be possible while a metallic film covers the outer region of the fiber. The diameter of the table-like structure is thus chosen to be larger than the desired mode's diameter so this region it is not harmed due to clipping. Figure 5.1a depicts the results of a test print on a flat glass substrate. Next, the sample is evaporated with a layer of copper. The structures on a flat glass substrate can then be removed by treatment in an ultrasonic bath. Indeed the shown structure provides sufficient protection during the evaporation process, as it leaves a sharp shadow in the metallic film, compare Fig. 5.1b. Despite the successful result of the presented sample, the removal process of the polymeric structure in general poses a challenge: On a flat glass substrate, the lift-off via an ultrasonic bath works. The rate of success is far from unity, but this can be compensated by the large amount of area that a substrate provides for placing multiple structures on top. However, according to the plan, the structures will be located on optical fiber ends. Here, the removal via ultrasonic bath does not fully serve its purpose: The fiber, as a comparably small and fragile object itself, is subject to the oscillations. Due to the fiber movement, the force separating fiber and structure is reduced. Further attempts, including organic solvents, plasma ashing, or a micromanipulator, either cannot lift off the structure from the fiber or additionally damage the coating on the fiber.
Thus, the design of the structure is modified to feature a pillar on top of the table-like structure, see Fig. 5.2. This pillar is later used as leverage to apply a mechanical force via a micromanipulator: This is a cannula attached to a micrometer translation stage, capable of three-dimensional positioning the tip with high precision. The process is performed under a stereoscopic microscope (Stemi 305, Carl Zeiss AG, equipped with a 2× lens). The structure easily comes off without any residuals. Additionally, the structure features further improvements: The simple table-like structure evolved into a kind of hollow cylindrical shape covered with a lid. The sides of the structure are now closed to avoid the evaporation of material below the structure. This could potentially happen when the substrate's position in the evaporation chamber is inclined to allow for metal deposition on the fiber's side. However, additional holes are left in this coat to allow the unpolymerized resin to flow out. The legs are not omitted but

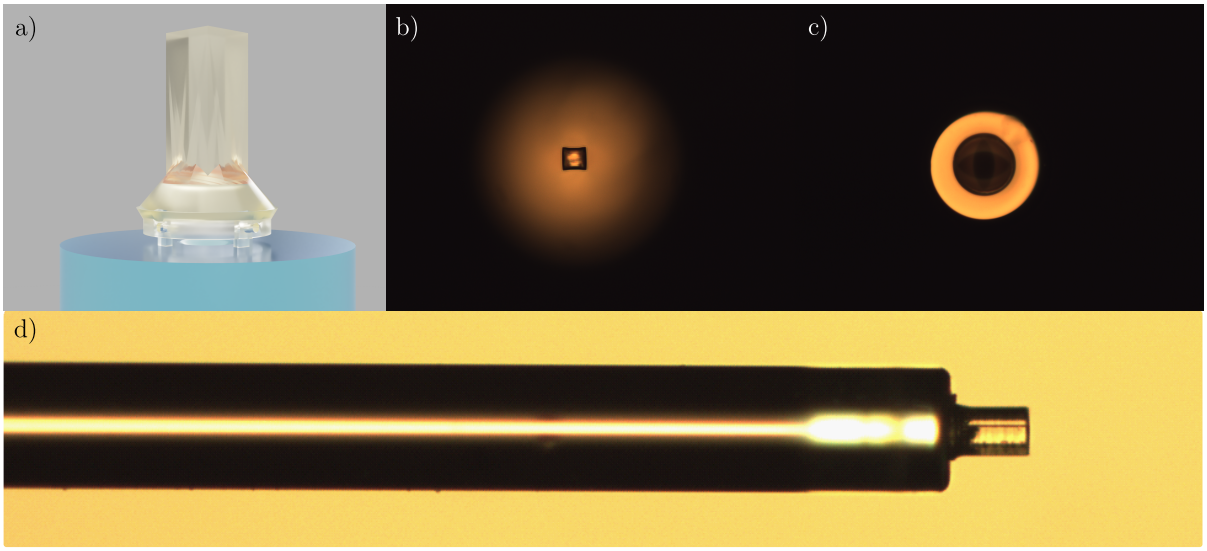

Figure 5.2: Collection of images depicting the cover of the fiber core with a pillar: a) Rendered image of the structure on top of the fiber. For the sake of clarity, the fiber's surface is not depicted as a mirror. b) Fiber in the optical microscope after evaporation, the focal plane is set to the top of the pillar or c) the surface of the fiber. d) View from the side after evaporation. For scale, the fiber's diameter is 125 µm in all images.

kept as short as possible. They are a useful tool to reduce the interface area with the fiber. The structure is written using the photoresist IP-S (Nanoscribe GmbH & Co. KG) and a 63× objective (Plan-Apochromat, Carl Zeiss AG). The diameter of the structure on the fiber amounts to 55 µm. The footprint of the pillar is 25 µm × 25 µm, and the height of the entire structure is 122 µm. Thus, it is divided into two parts, the cover and the pillar. Both are written in galvo scan mode, but with different hatching and slicing properties for a reduction of writing time: The bottom part with a total height of 26 µm features a slicing and hatching distance of 0.3 µm and a laser power of 40% (100% corresponding to 50 mW) at a scan speed of 1000 µm/s. The top part has a slicing and hatching distance of 1 µm and a laser power of 60% at a scan speed of 1000 µm/s. The overall writing time is about seven minutes.

Measurements of a Single Electrode Fiber

In collaboration with the group of Prof. Michael Köhl, namely his student Andreas von Haaren at the University of Bonn, we are able to prove the preservation of the optical properties of a coated fiber: A fiber mirror was created by shooting a cleaved fiber with a CO_2-laser and subsequently applying a dielectric coating. The fiber is then used in a fiber-fiber cavity and the finesse is measured. Next, a polymeric structure is printed on top of one of those fibers. Subsequently, a layer of copper is thermally evaporated before the mechanical removal of the polymeric structure is performed. The resulting fiber endfacet is depicted in Fig. 5.3a. Hereafter, the fiber is assembled in the cavity exactly as before the process of metalization. The finesse of the fiber-fiber cavity is then measured again. As shown in Fig. 5.3b, the data does not show a systematic deviation of the properties before and after the fabrication procedure.

In conclusion, neither the contact of the fiber with the photoresist, nor the chemical development procedure, nor the thermal evaporation, nor the mechanical removal harmed the fiber's coating or structure to the extent that it lost its optical properties. Thus, such a fiber could provide advantages for multiple applications. Upon contacting the metallic film with, e.g., ground potential, the charge accumulation in a fiber trap could be omitted. This charge accumulation is a typical issue present in experiments with a trapped ion [135]. Due to the charge of the ion and the corresponding electric field, charges in the closest proximity (so, on the fiber ends) move and rearrange. Therefore, the ion is influenced by itself, which imposes a perturbation that is avoided when metalized fibers are used.

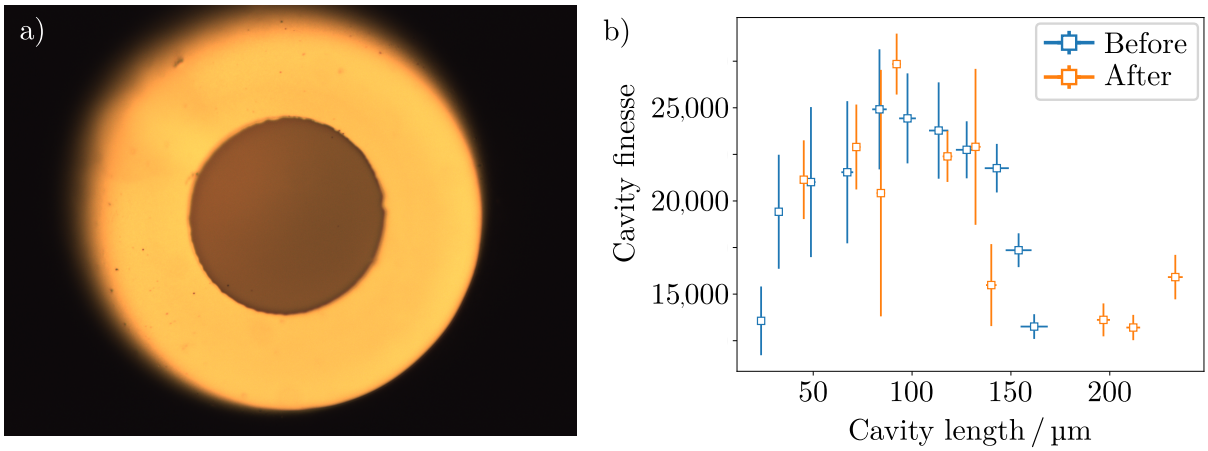

Figure 5.3: a) Microscope image of the endfacet of the fiber after the structure is removed. b) Measurement of the cavity finesse in dependence on the length of the cavity before (blue) and after (orange) the metalization. It becomes evident that the metalization does not harm the performance of the cavity. The measurement was conducted by Andreas von Haaren, University of Bonn. Compare [57].

5.2 Structures with Multiple Electrodes

Analogously to the aforementioned creation, a fiber with more electrodes could serve additional applications. Depending on the geometry and the applied voltage or current, an electric or magnetic field could be emitted that provides some kind of interaction with trapped particles. In the following, we will deal with the creation of such a fiber with four symmetrical electrodes.
The first tests included printing a larger structure on a flat glass substrate. The metalization and subsequent treatment in an ultrasonic bath provided successful results, compare Fig. 5.4a and 5.4b.
In the case of a single electrode on a fiber, the contacting with a wire (e.g., connected to an external voltage source) is not critical: It can be attached to any part of the fiber spot that is covered by the metallic coating. A combination of multiple evaporation steps and/or evaporation at an angle allows the application of contacts on the side of the fiber. Having the wires connected to the sides is beneficial since it avoids the presence of electrical connections on the endfacet: Otherwise, the contacting of the electrodes would inevitably have to be placed on the endfacet as well, which would massively influence the created electric/magnetic field.

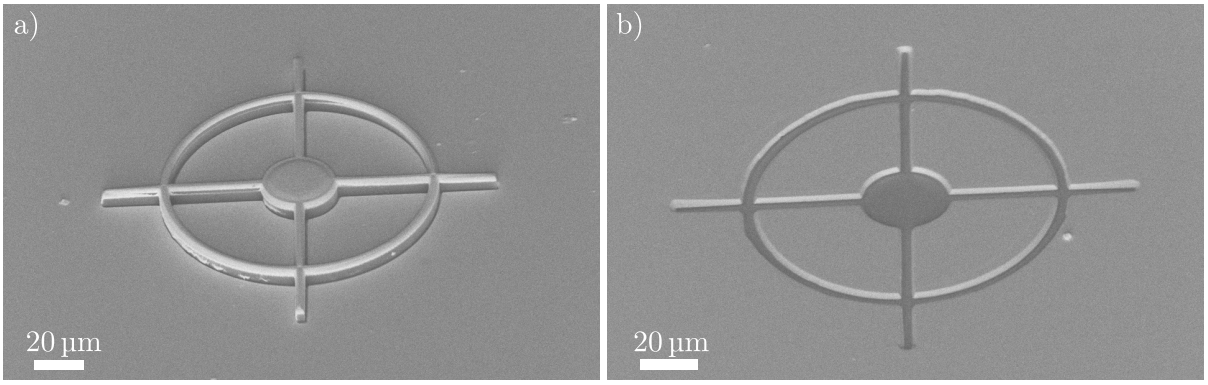

Figure 5.4: Test structure for patterning four distinct electrodes. a) A layer of copper has been evaporated onto the structure and the substrate. b) After a lift-off process in an ultrasonic bath, the polymeric structure could be removed, revealing the electrodes.

An exemplary structure we aim for is presented in Fig. 5.5. This figure shall clarify the terms used later on: Electrodes on the endfacet are connected via conducting stripes to conductive pads sitting on the side of the fiber.
For applying a structure via DLW directly on the side of the fiber, the laser is partially illuminating the fiber itself. Thus, the region with intensities high enough for TPA becomes distorted. Since the structured metalization of the fiber side shall cover a large area, the limited working distance of the used objective imposes an additional limitation. Thereby, the DLW system is not suitable for patterning a mask in this configuration.
These results led to a different approach: A mask is fabricated on a flat glass substrate (as illustrated in Fig. 3.1a) and later applied to an optical fiber by inserting the fiber into the mask. This procedure provides a wide range of possible applications, including different geometries and it is (at least for our application) not inherently limited by the used objective. Further advantages include the possibility of mass fabricating masks without changing the substrate.

5.2.1 Design

Some design principles have proven useful, independent of the desired structure on the fiber: We start with a cylindrical shape larger than the fiber diameter. The side, where it attaches to the substrate, is supported by a block of polymer to improve adhesion to the substrate. A center bore, still larger than the fiber diameter, is applied. Inside the cylindrical coat, four bars are added symmetrically around the center. These serve as guiding rails when the fiber is pushed inside the mask. On top of those, tiny triangular features are applied, serving as barbed hooks for the fiber. These simultaneously hold the mask tight to the fiber and align the fiber and the mask against each other. The mask features a tapered opening. So a fiber, which is gently pushed over the substrate's surface, is guided into the mask. The desired design for the endfacet or the side can then be added to the mask. When the side of the fiber shall be patterned, this pattern is preferably oriented to the bottom of the structure. This provides additional stability to the structure, since the open areas are supported by the substrate and free-floating parts are avoided. To receive a sharp defined pattern on the endfacet of the fiber and on the side, it is desirable to use a process

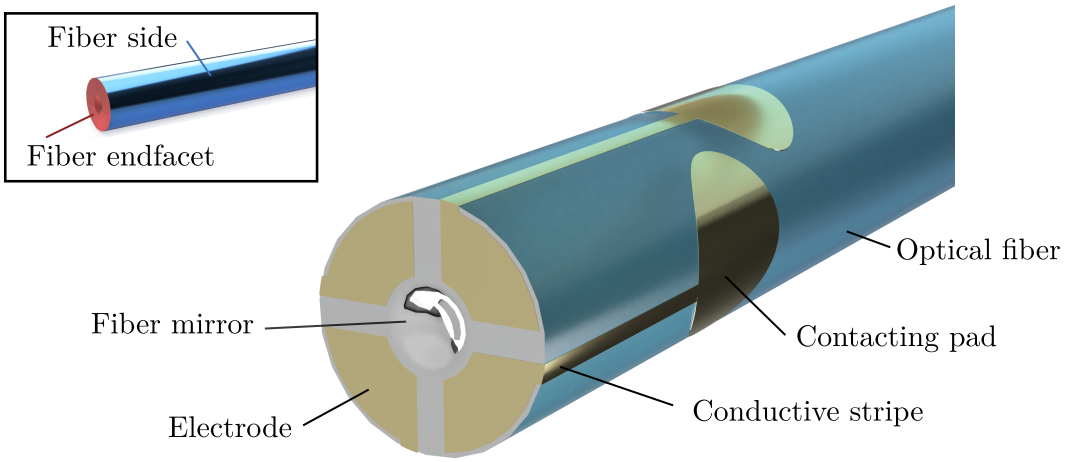

Figure 5.5: Schematic depiction of an optical fiber with metalization. The graphic depicts the expressions that are used for the various elements. The inset depicts what areas are meant by the terms fiber endfacet and fiber side.

involving two masks. One mask is used for patterning the endfacet of the fiber, and the second one for patterning the side. In a subsequent evaporation procedure, the construct can be aligned so that the angle from which the evaporation molecules impinge on the fiber is optimized for the respective mask. Finally, to establish an electrical connection, an overlap between the two mask patterns should be implemented. Thereby, the procedure requires alignment of the already partially structured fiber when inserting it into the second mask. Markers on the masks can simplify this procedure.
When arranging the contacting pads on the side of the fiber, e.g., opposite each other or in a row, it is crucial to ensure sufficient spacing between the conductive stripes: Otherwise, the shadow structure may lead to an electrical connection that is not intended in the case of evaporation at an angle. The placement of the pads along the fiber is arbitrary. However, the longer the mask, the more printing time is needed and the less rigid it is. Due to the fabrication on a large ($22\,\mathrm{mm} \times 22\,\mathrm{mm}$) indium tin oxide (ITO) covered[2] SiO_2 substrate, it is possible to create a whole array of structures in a single printing process. Thus, a variety of masks with slightly different inner diameters can be printed. The polymer tends to shrink in the development procedure. The creation of a whole array covering various inner diameters ensures that there always is a fitting mask for a fiber on the substrate.
Schematically, the fabrication process is depicted in Fig. 5.6. A mask applied to a fiber (Fig. 5.6a) creates a pattern due to shielding (Fig. 5.6b) during an evaporation process in which the fiber is continuously rotated. The same fiber is then inserted into a second mask (Fig. 5.6c) and evaporated again while rotating, resulting in the desired pattern on both the endfacet and the side of the fiber (Fig. 5.6d).

[2] The ITO coating provides a different refractive index than the underlying glass substrate. This difference in refractive indices between the used photoresist and the ITO coating assures a successful outcome of the automated interface finding procedure of the DLW system.

The resulting masks have a dimension of 170 µm × 171 µm × 640 µm (length of the four electrode masks is 755 µm) and are written in the galvo scan mode. The 25× objective (LCI Plan-Neofluar, Carl Zeiss AG) is used in combination with the photoresist IP-S (Nanoscribe GmbH & Co. KG) on an ITO-coated substrate. The object is sliced using a maximum slicing distance of 1 µm and a hatching distance of 1 µm. At a laser power of 100%, corresponding to 50 mW, the scan speed is 100, 000 µm/s, which leads together with the corresponding settling times to a print duration of just under four minutes for each mask.

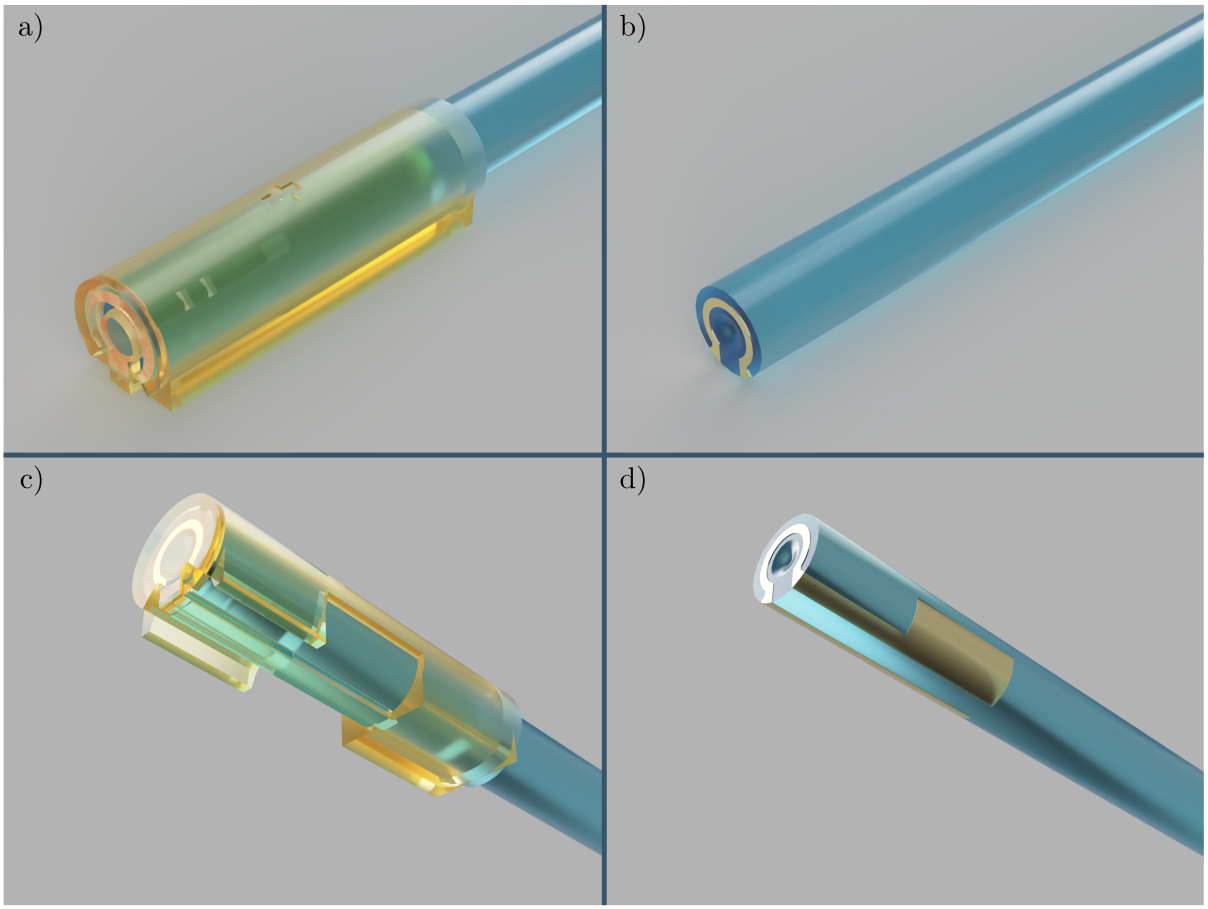

Figure 5.6: Procedure for creating an Ω-shaped antenna on a fiber endfacet: a) A cleaved fiber is inserted into a mask fabricated by DLW. b) After thermal evaporation of copper or gold, e.g., the mask is pulled off and the fiber endfacet shows the metallic structures resulting from the shadowing effect of the mask. c) The fiber is then inserted into a second mask: With regard to the orientation of the already existing structure, a micromanipulator is used to push it into the mask. d) A second evaporation process is performed, during which the fiber is constantly rotated. The axis of rotation is now severely inclined to achieve a coverage of both, the fiber's side and the edge between endfacet and side. This ensures the connection of the structures on the side to the antenna on the endfacet. The mirror coating is omitted in this depiction for improved visibility of the created structure.

5.2.2 Mechanical Handling of the Masks

For the insertion of the fiber into the mask, the aforementioned self-made micromanipulator is modified: A fiber mount, consisting of a V-groove and two clamps that gently push the fiber into the groove, is mounted on a translation stage. The sample with numerous masks is glued with elastic glue (Fixogum, Marabu GmbH) on top of a rotation stage. The setup is located below a stereoscopic microscope. Viewing from the top, it is possible to align the fiber with a mask in two dimensions via the translation and the rotation stage. The translation stage can be used to lower the fiber onto the substrate so the tip of the fiber is positioned directly in front of the intended mask. The fiber is then pushed over the surface of the substrate for a short distance (in the order of 100 µm) before entering into the funnel of the mask. In case the mask provides a tight fit and the fiber does not enter completely, it is useful to lift off the mask with the fiber in this stage. This is done by pushing the fiber into the mask and simultaneously pulling the fiber upwards, away from the substrate. The mask may fly off during this procedure due to the fiber oscillating after the mask becomes detached from the substrate. In this case, a different mask from the array is chosen and the insertion process starts again from the beginning. Otherwise, the mask sits on top of the fiber but is not completely inserted. A flat area, for example the handle of metallic tweezers, can be used to push against the mask gently. Typically, after some reiterations, the fiber is fully inserted, as depicted in Fig.5.6a, and ready for evaporation.
Inserting the fibers again into the second mask after the first evaporation step follows the same principle. In addition, marker structures come into play, which allow for the correct orientation of the masks with respect to the rotation around its axis: In the V-groove, the fiber can be rotated so that the markers are aligned to the top. The needle of the micromanipulator is then guided to apply a small amount of pressure on the top of the mask: Just enough to hold the mask into place without deforming it. The fiber can then be pulled out, see Fig. 5.7. Subsequently, the fiber is directly inserted into a mask for the second evaporation run. In the meantime, the orientation of the fiber itself does not change and matches the orientation of the second mask. To preserve the structure created in the first evaporation run, the above-mentioned bars inside the mask for guiding the fiber can be arranged with a minimum overlap to the created metalized structure. By doing so, the fiber slides into the mask only on its pure glass parts. For the same reason, it is recommended to use the mask that patterns the endfacet of the fiber first before using the mask for the side pads.
Possible short-circuits that may arise around the edge of the fiber must be prevented by accurate alignment of the fiber with respect to the second mask.

5.2.3 Thermal Evaporation

For the evaporation the fibers with masks on top are mounted inside the chamber of a thermal evaporation machine (Univex 250, Leybold GmbH). A rotation stage (8MR151-30 vacuum compatible, Standa Ltd., see Fig. 5.8) is controlled via a controller (8SMC5-USB, Standa Ltd.) and the related software (XILab, Standa Ltd.) and ensures a steady rotational motion of the fibers during the evaporation process. In the past, before the installation of the rotation stage in the chamber, four consecutive evaporation runs were necessary to cover the full circumference of the fiber with material. In case of an additional adhesive layer, even eight runs would have been necessary. In the course of this project, adhesive layers are omitted. Since an adhesive

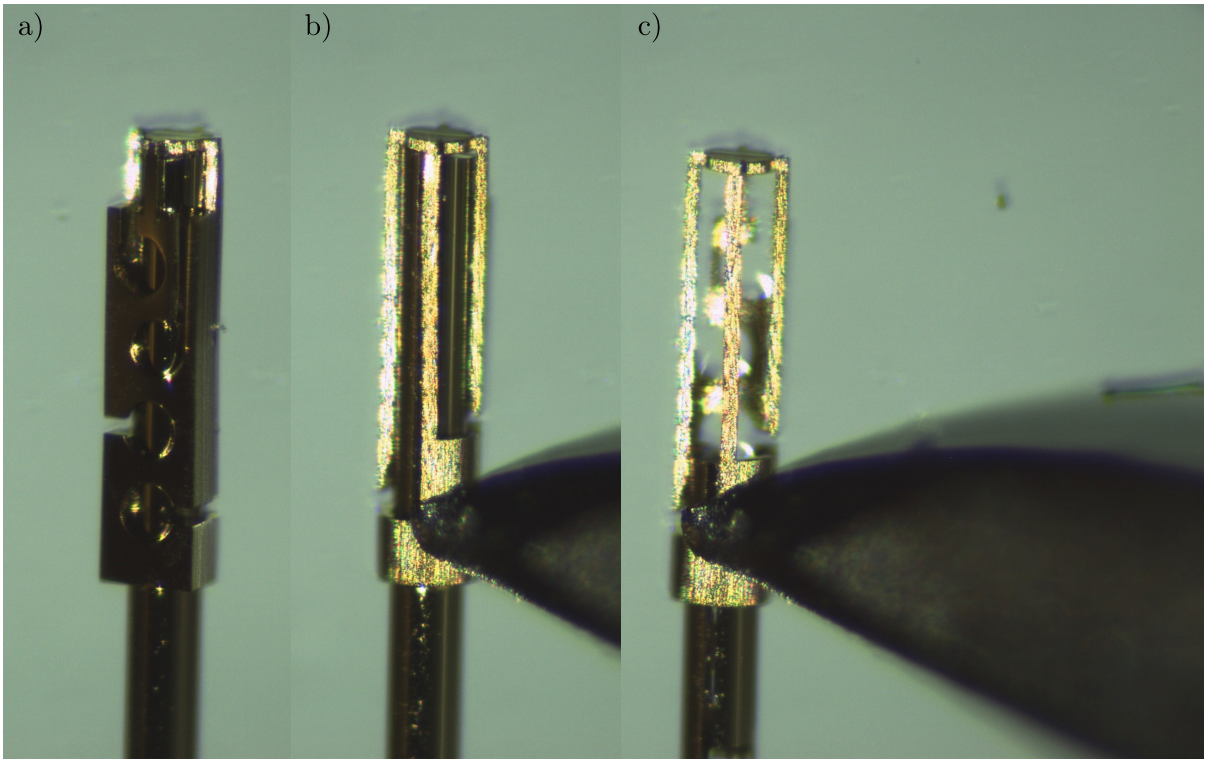

Figure 5.7: Slide show of the removal of a mask. a) First, the fiber is placed in the holder and fixed under the microscope. b) It is then rotated so that the mask is oriented with its flat side towards the underlying glass substrate. The fiber is then lowered with the mask onto the glass substrate. The needle from the micromanipulator is used to push the mask onto the substrate gently. c) The translation stage holding the fiber can then be used to pull out the fiber from the fixed mask.

layer is evaporated from a separate source, see Fig. 5.8, it encloses a different angle with the mask and the underlying fiber than the other material used. This leads to a blurring in the peripheral areas of the shadow structure, where the structure is partly exposed to only one of the two materials. Hence, the resolution of the shadow structure is worse, compared to the usage of a single evaporation source. In addition, chromium, the popular adhesion promoter for the usage with gold (compare [136]), features an electric dipole momentum, which can disturb particle-trapping setups. Due to the lack of an adhesion layer, the created structures from gold must be handled with care since the adhesion to the fiber is not particularly large. For the development of the procedure, the gold was often replaced by copper to achieve large layer thicknesses while still being affordable. Copper features a better adhesion to the fiber [137] but its conductivity is inferior.
The pressure in the chamber is pumped down with the help of a turbo-molecular pump (Turbovac MagIntegra, Leybold GmbH) to a level of $\approx 5 \cdot 10^{-6}$ mbar, before the deposition procedure begins. Located in a tungsten boat, compare Fig. 5.8, gold pieces are heated up by an electric current of 86 A. As soon as the current reaches its target value and the boat and its content is uniformly heated, a shutter opens via a pneumatic system. Typically, a monitoring system for the evaporation rate would come into play now: The evaporation machine is by default equipped

with a sensor for measuring the film-thickness live during the evaporation run. This sensor is a quartz crystal with a characteristic frequency. Due to material deposition on the crystal, its mass and therefore its frequency changes. A computer analyzes this shift, and in combination with the density of the material used for evaporation, the film thickness can be deduced. The indicated thickness of course relates to a certain height above the evaporation source and is only reliable if it is close enough to the samples.
However, aiming for good electrical conduction, thicker evaporated films are advantageous. For this purpose, either the amount of evaporated material can be increased, or the distance between the evaporation source and the fiber can be reduced. The latter is chosen, which can be easily motivated by expenses and the circumstance that some fiber electrodes have been created via the evaporation of gold. Due to the self-made mounting of the rotation stage and its motion, the sensor cannot be used as intended, and the film thickness is estimated. In the presented case, the exact value is not critical. If needed, for example for some of the possible future applications, a glass sample can be mounted next to the fibers and used for atomic force microscopy measurements. Thereby, the thickness of the film on an evenly rotated fiber at roughly the sample position can be deduced.
The positioning of the rotation stage is chosen so that the shadow created is evaporated with a slight inclination between upwards traveling metal molecules and the desired deposition regions on the fiber. Therefore, the mounting depends on the chosen mask: The evaporation of the endfacet of the fiber demands a slight angle between the fiber axis and the upwards traveling gold molecules. Hence, the region on the endfacet, as well as the edge of the fiber, are subject to the material deposition, which is beneficial for establishing a proper conductive connection between the structures on the endfacet and the fiber's side. Analogously, for the evaporation of the pads on the fiber's side, the rotation stage is mounted so that the fiber's side and partially the edge region of the fiber are covered. Figure 5.8 depicts a setup used for evaporation with the mask for patterning the pads on the side of the fiber.

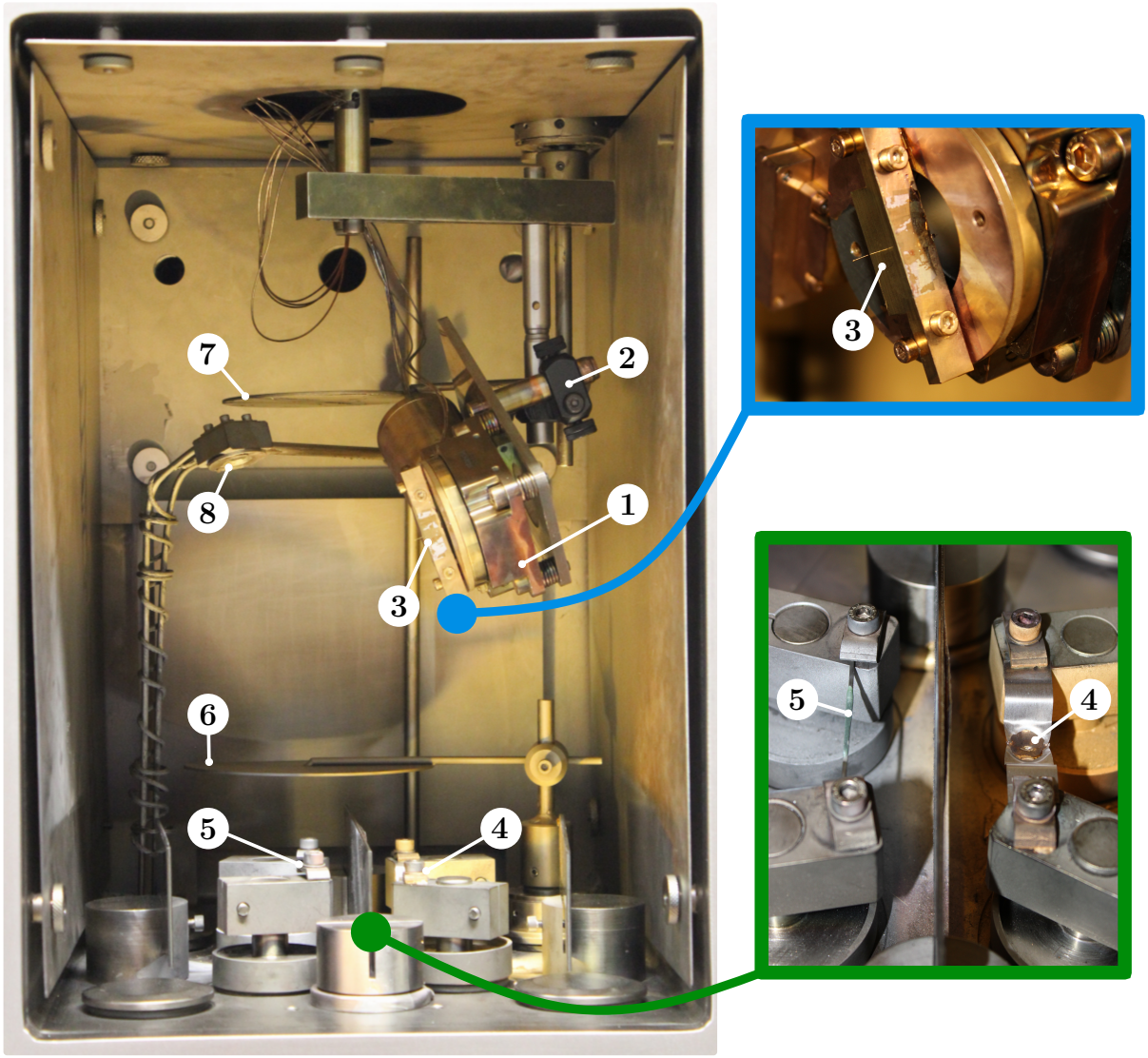

Figure 5.8: Setup of the evaporation machine for the metalization of fibers: The motorized rotation stage ① is aligned using posts and a hinge ②. The fiber itself is mounted on top of the rotation stage ③ and can be fed through the central hole of the stage. Heated by an electric current, a tungsten boat with gold inside ④ evaporates the material. A second evaporation source ⑤ can be used to apply an adhesion layer, namely chromium or titanium. Due to the spatial separation between the sources, the shadows on the fiber do not exactly overlap and cause a smearing out of the desired structure. Thus, only a single evaporation source is used here. The shutters ⑥ and ⑦ are used for the controlled deposition of the material. Due to the installation of the rotation stage, the upper shutter can not be used in this configuration. The quartz crystal ⑧, used for monitoring the evaporation rate, may be unreliable due to the changed distance between the source and the sample and the steady rotation of the fiber. In other scenarios, the rotation stage may shield the evaporation flow from the crystal completely.

5.2.4 Applied Structures

Following the guidelines given in Subsec. 5.2.1, two different structures are realized. Each structure is created in a procedure using a set of two masks. The first set presented below allows dividing the endfacet of a fiber symmetrically into four separate electrodes. These can serve to create an electrical field configured to the requirements of the application. The second example features an Ω-shaped metalization. Here, both ends of the shape can be contacted via contacting pads on the side of the fiber. Thus, this shape can serve as an antenna.

Four Electrodes The design is realized using the masks depicted in Fig. 5.9a and 5.9b. The mask in Fig. 5.9a serves to divide the endfacet into four symmetrical sectors. The electrodes are separated by bars of 15 µm width, and the central region of the fiber is protected by a disk with a diameter of 50 µm. The mask in Fig. 5.9b ensures the patterning of the conductive stripes and the pads on the side of the fiber. In this case, the pads are arranged in a row on the same side of the fiber. This would allow the connection to external wires used with a V-groove substrate. Each pad has a diameter of 100 µm. The resulting structure on the endfacet of the fiber can be found in Fig. 5.9c, while Fig. 5.9d and 5.9e depict the view to the side of the fiber from two slightly different angles.

Ω-Shape An Ω-shaped antenna is created for the application as an integrated antenna on a fiber endfacet. Figure 5.10a and 5.10b show the masks used. In Fig. 5.10a the marking on top of the mask is visible, which simplifies the alignment of the fiber in between the two evaporation procedures when switching from the first to the second mask. The Ω-shaped structure is connected to the pads on the side of the fiber using two stripes, which are guided around the fiber edge. The slits establishing the connection between the Ω-shaped structure on the endfacet and the structure on the side of the fiber are shown in Fig. 5.10c. The contacting pads are sitting on opposite sides of the fiber and spread over 450 µm × 118 µm. This large area ensures simplified alignment in the connection procedure. The outer diameter of the Ω-shape is 100 µm, while its width is 13 µm. While various sizes have been fabricated, possible applications demand for the maximum sized Ω-shape circumference, limited only by the fiber's size, compare Fig. 5.10d.

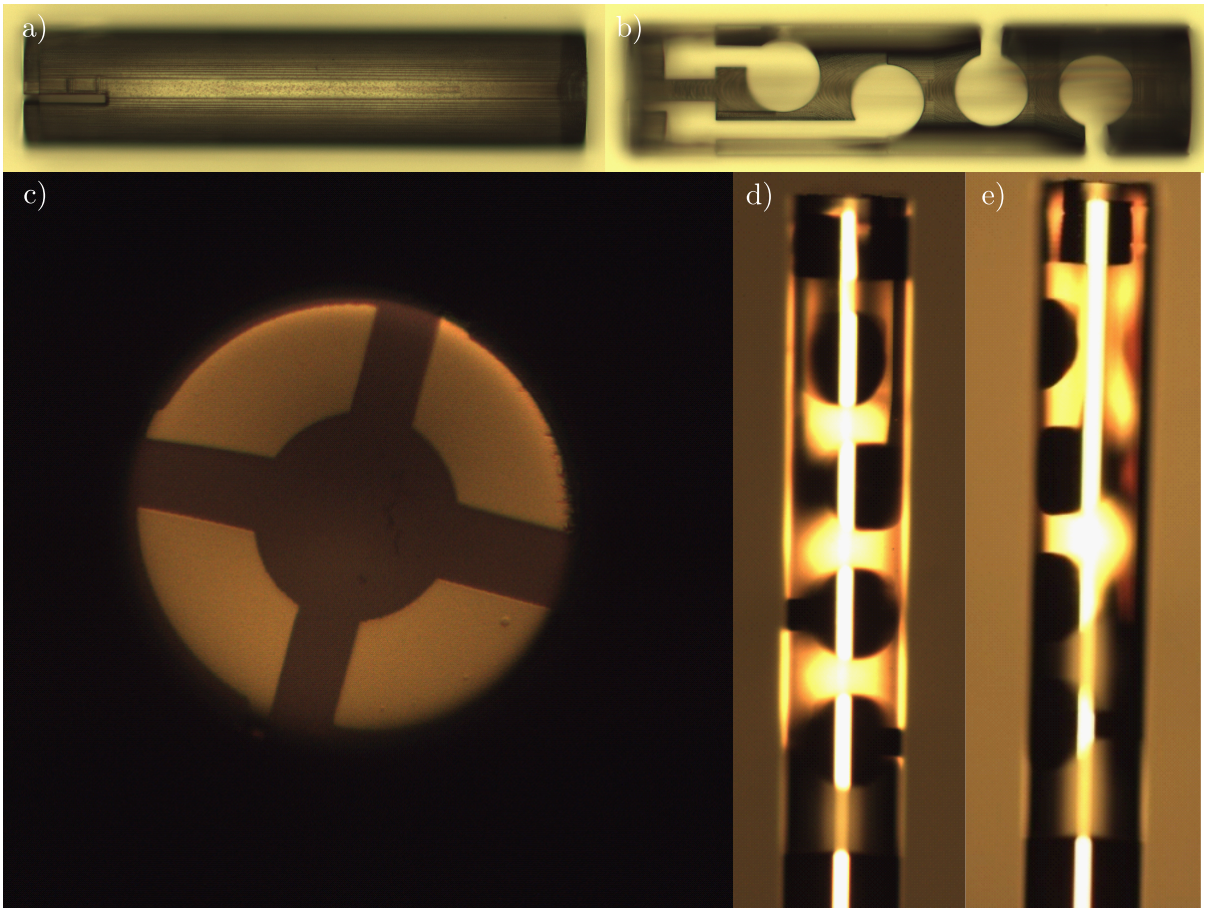

Figure 5.9: Process stages of creating four electrodes on a fiber. a) Shown is the mask responsible for structuring the fiber's endfacet with slits leading around the edge to connect to the pad structure on the side. b) Depicted is the mask used to create the contacting pads on the side of the fiber. The optical microscope is focused on the mask's base, revealing the structure of the four pads. The endfacet of the finished structured fiber is depicted in c) and the view on the side pads in d) and e). The mask's dimensions are 170 µm × 171 µm × 755 µm, the fiber has a diameter of 125 µm.

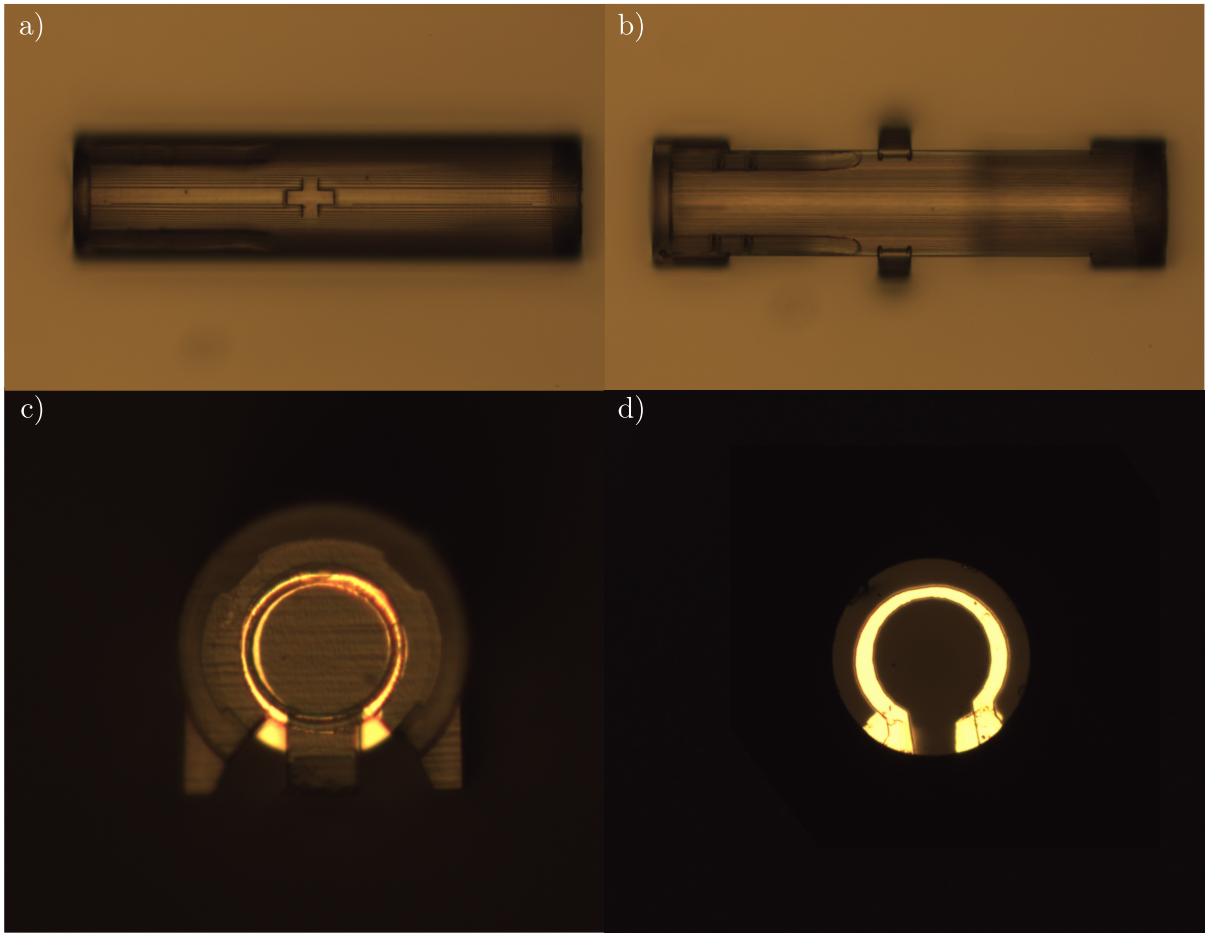

Figure 5.10: Optical microscopy captures from the fabrication procedure: a) and b) The masks, respectively, for the first and second step are presented, printed on a glass substrate. Image c) shows a fiber after the first evaporation step, which is already inserted in the second mask. This corresponds to the schematic depiction shown in Fig. 5.6c. Image d) shows the finished fiber corresponding to Fig. 5.6d. The mask's dimensions are 170 µm × 171 µm × 640 µm for each mask, the fiber has a diameter of 125 µm.

5.2.5 Conductive Connection to the Fiber Pads

Various approaches were tested to connect the electrodes using the pads on the side of the fiber to the outer world. Wire bonding as a technique is not suitable due to the strong curvature of the pads on the side of the fiber. Additionally, the film thickness of the pads of around 1 µm is rather close to the lower limit for reliable bonding procedures. Silver glue could connect pads successfully to wires, but the application only works in a coarse regime. For structures with only one single electrode, this might be the method of choice because it is a fast, reliable, and easy way. However, for more than one electrode on a fiber, the probability of short-circuiting is strongly increased.
To obtain a precise and reliable connection between the pads on the fiber's side and external wires, a conductive promoter is used. A so-called fuzz button (Au/Mo-compound, non magnetic, Custom Interconnects) serves this purpose: This is a piece of wire, crumbled together in a cylindrical shape with 0.01 in in diameter and 0.07 in in length (corresponding to a diameter of 254 µm and a length of 1.78 mm). Gold wire (diameter of 0.1 mm, purity 99.95%, Thermo Scientific) is used to apply pressure on the fuzz button: Due to its crumbled structure, a reliable connection between the fuzz button and wire is established when applying a slight pushing force on the wire. This procedure is performed for both sides, compare Fig. 5.11a.
Using ferrules for the precise alignment of fibers has proven useful in various situations, e.g., in optomechanical experiments. Similarly, a ferrule can be used in this experiment to place and hold the fiber reliably, while wires may be attached simultaneously. Thus, the ferrule needs to provide access to the side of the fiber where the pads are located.
Such a ferrule is produced by DLW. The ferrule provides one channel for the insertion of the optical fiber. Perpendicular to this, located at the end of the ferrule, two additional channels, opposing each other, provide access to the pads on the side of the fiber. The tapered design of these channels ensures the exact placement of the wires and the fuzz buttons at the contact area, see Fig. 5.11b. Due to the dimensions of the channel, the fuzz buttons are limited in their

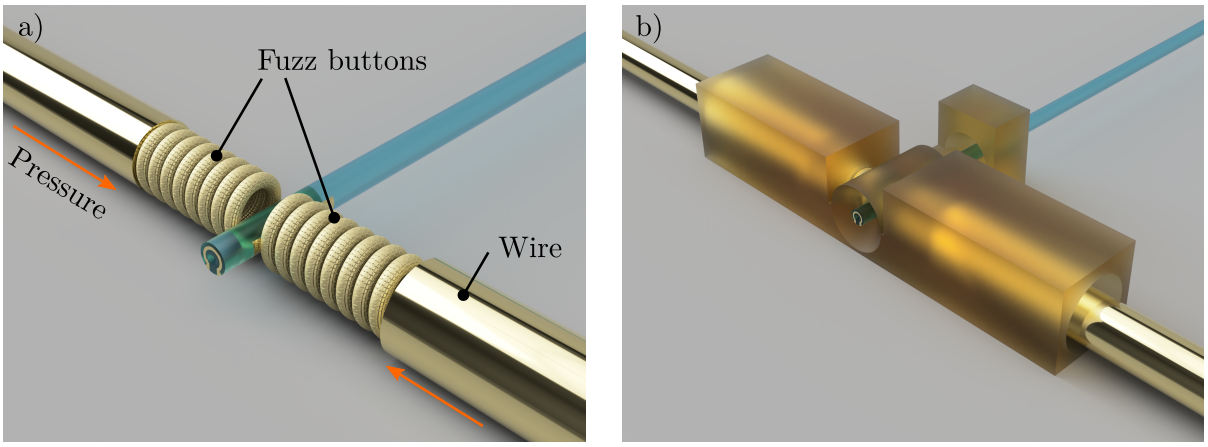

Figure 5.11: Scheme for the electrical connection of a finished fiber: a) The pads on the fiber's side are connected to external wires via conductive fuzz buttons. Via the application of a pressing force, the connection is established. b) For the realization of the scheme depicted in a), the arrangement is encapsulated by a DLW-fabricated structure.

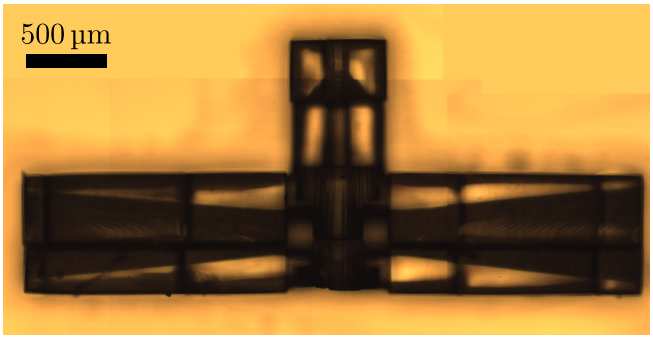

Figure 5.12: Depiction of a polymeric ferrule for the contacting of a metalized fiber. The ferrule exceeds the microscope's field of view, which is why the shown picture is stitched together from multiple captures. The width extends to 3.8 mm × 1.6 mm and the height amounts to 700 µm.

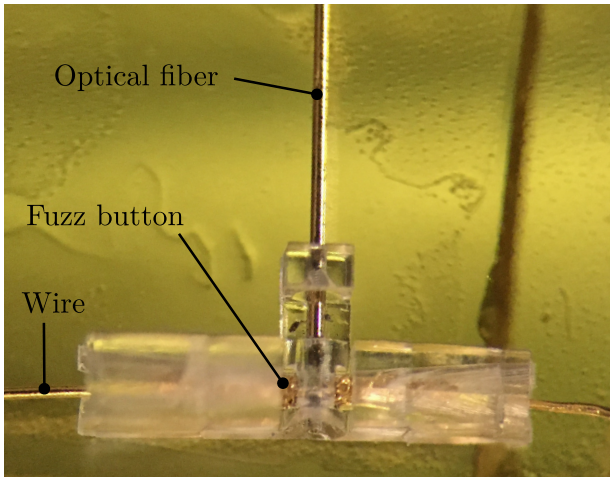

Figure 5.13: Setup of the contacted and finished fiber: A ferrule produced by DLW provides a channel for the optical fiber to fit in. Putting a tiny droplet of super glue on the spatially separated holding block in the back fixes the fiber in its position. The ferrule's two dedicated channels opposing each other provide easy connection to the contacting pads on the fiber's side: A so-called fuzz button as conducting agent and a gold wire can be inserted in these channels. The electrical connection is established by applying a slight pushing force on the gold wires.

movement to the direction perpendicular to the optical fiber. Applying pressure via the wire establishes the contact between the electrode pad on the optical fiber and the fuzz button, as well as between fuzz button and wire. A fabricated version of the ferrule is shown in Fig. 5.12.
The optical fiber is inserted with its rear end first into the ferrule. Thus, neither the endfacet, nor the side structure of the fiber is harmed. For this procedure, the fiber coating needs to be completely stripped off. Ideally, this is done right in the beginning, even before inserting the fiber into the first mask. A ferrule with a larger diameter would also allow for unstripped fibers to be inserted but comprises the disadvantage of less guidance of the fiber tip in the ferrule.
Due to the side pads' size, the fiber alignment with respect to the ferrule does not demand for high precision when only accounting for the electric contact. Alignment with the micromanipulator

and relying on the view through the stereoscopic microscope has proven to be useful. The fiber can be fixed with a tiny droplet of superglue in the back of the ferrule. Due to the spatial separation of the region where the glue is applied to the region of contacting, capillary forces do not destroy the fiber's metalization structure: Without a separating gap, the glue would be pulled into the region of the contacting pads, preventing any electrical contact. The finished setup can be found in Fig. 5.13.
A measurement of the resistance resulted in a value of 11 Ω for the system of gold wire – fuzz button – Ω-shaped antenna – fuzz button – gold wire. This proves that an electrical connection through the Ω-shape is established.
Polymeric structures can be obstacles for some experimental setups regarding their vacuum compatibility. Previously, structures machined with the DLW system have already been applied in vacuum environments without constraints, but the presented ferrule is a giant structure in comparison. As a precaution, an atomic layer deposition procedure may be used to shield the polymeric material from its environment, eliminating any outgassing.

5.2.6 Examples of Less Successful Connection Methods

The above-presented connection approach is the result of a broad range of attempts. There are much more straightforward and more apparent approaches for contacting the electrodes, which were tested but were unsuccessful. In the following, some of those will be briefly illustrated.

Wire Bonding

Wire bonding is widely used to create conducting connections between micrometer-sized pads. Especially in our spatially neighboring particle physics groups at the University of Bonn, wire bonding is popularly used on the chips of pixel detectors.
In a simplified form, a wire bonding machine takes a thin piece of, e.g., gold wire, pushes it onto the bonding patch, and uses ultrasonic oscillations to melt the wire onto the patch. This procedure establishes a conductive connection with a small footprint.
When applying wire bonding to the fiber side, two limitations become clear: On the one hand, the typical layer thickness on the side of the fiber does not exceed 1 µm. For the wire bonding procedure, thicker layers are beneficial. Nevertheless, this would not ultimately exclude wire bonding as the method of choice. However, during a bonding process, the substrate is subject to an upwards pulling force. This force can cause the electrode pads on the fiber to rip off since their adhesion to the fiber is comparably weak. On the other hand, the curved surface of the fiber pad is the ultimate exclusion criterion for the wire bonding procedure: With its curvature at a diameter of 125 µm, the fiber side is severely curved and this imposes an invincible limitation for wire bonding.

Positive Tone Resist on V-groove Substrate

Glass substrates with a carved V-groove are commonly used to align optical fibers. Typically, the depth of the groove exceeds 100 µm. In principle, a positive tone resist (AZ MIR 701, Microchemicals GmbH) can be used on this substrate: The DLW system imprints a pattern

covering the outer area of the substrate and its groove. After the chemical development, the thermal evaporation of a metallic film, and the lift-off procedure, the resulting structures could serve as conducting elements from the fiber pads to some macroscopic patches. For this method, all fiber pads are arranged next to each other on one side of the fiber, as depicted in Fig. 5.9. The fiber would be positioned in the groove with the pads aligned to the conductive stripes. An external force would be used to push the fiber into the groove and establish the electrical connection.
This attempt fails due to the topography of the substrate: The positive tone resist has to be applied in a spin-coating procedure. This results in a film thickness of at maximum 5 µm. Thereby, the V-groove itself is not consistently covered with the resist. Experiments on these substrates show that the patterned paths turn out nicely on the flat glass surface but cannot be fabricated inside the groove.

Silver Glue

Instead of using paths resulting from a lithography process, silver glue could be directly applied to contact the pads to wires. Experiments show that a reliable and reproducible process is impaired by the size of the silver glue droplets and the precision at which the glue can be applied due to its viscous nature. The combination with a binding agent also does not provide successful results, so this approach is not pursued further.

Manipulating Ferrules

Comparable to the V-groove glass substrate, ferrules are used to hold optical fibers in a fixed position. The most widely used and commercially available ferrules are made from ceramic or glass, with an inner diameter of $1 - 10\,\mu m$ larger than the fiber diameter, while their outer diameter amounts to 1.25 mm or even 2.55 mm. In order to create a firm connection, the fibers are typically glued into position after insertion. For a schematic view, see Fig. 5.14a.
Similar to the masks for the fibers, a mask for such a ceramic ferrule is designed and fabricated using DLW. Due to the size of the ferrule, this print exceeds the classical limits: The field of view of the used objective is much smaller than the size of the model, so several blocks are polymerized edge-to-edge to form the final structure (a so-called stitching procedure). After insertion of the ferrule into the mask, it is mounted on the rotation stage in the thermal evaporation chamber. Following thermal evaporation of metal, in this case copper, the mask is pulled off from the ferrule, and reveals the metallic structure: Two large pads, opposing each other, were created on the side of the ferrule, sized large enough for a macroscopic connection, see Fig. 5.14b. Originating here, metallic stripes lead to the fiber channel of the ferrule from opposing sides. They overlap with the channel partially, without touching each other and avoiding a short-circuit, see Fig. 5.14c. A fiber can be inserted and needs to be aligned with regard to the existing contacting pads. Unfortunately, an electric connection between the fiber and the ferrule metalization cannot be established: Placing a droplet of silver glue between the fiber and the ferrule immediately covers the whole circumference of the fiber. Again, the properties of silver glue seem not to be ideal for the application on fibers.

Ultimately, the mechanical manipulation of a ferrule is tested. The idea is to drill a channel transversal to the axis of the optical fiber in a ceramic ferrule. The insertion of a wire would then assure a correct alignment to the fiber pads, comparable to the method that has proven successful.
It turns out that drilling into the ceramic material is not possible, even with hardened drills. In this regard, switching from ceramic to glass ferrules might provide a working platform for the contacting. However, the more obvious approach for us is using the DLW system again to print ferrules that meet our requirements.

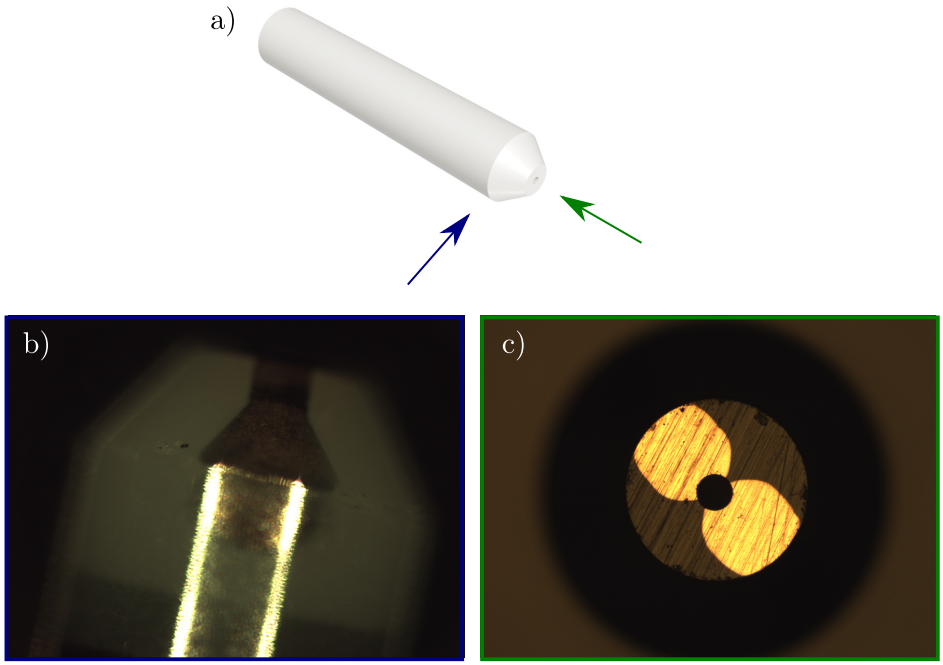

Figure 5.14: A ceramic ferrule with an outer diameter of 1.25 mm, partially covered with a polymeric mask, was subject to an evaporation run. Inset a) shows a schematic view of the ceramic ferrule with arrows marking the point of view regarding the following two insets b) and c). Those are optical microscope images of the resulting structure.

5.2.7 FEM Simulations and Applications

Simulations are performed in order to estimate the electric and magnetic fields that can be obtained with the presented geometries. Again, the software Comsol Multiphysics is consulted to apply a finite element solving procedure. The electrodes are modeled and implemented as depicted beforehand. They are assigned the properties of copper and have a thickness of 1.5 µm, positioned on the end of a fiber made from SiO_2. Stripes of a perfect electric conductor, sitting on the fiber's side, connect to the electrodes or the antenna. These stripes lead to one or more wave excitation ports positioned down the fiber at a distance of more than 100 µm to the fiber endfacet. A sphere limits the calculation domain around the fiber and is implemented as a perfect electric conductor.

Four Electrodes The result of the simulation for the electric field emitted by the four separate electrodes can be found in Fig. 5.15. Depicted is the z-component of the electric field. The electrodes are operated via the wave excitation ports in a Paul trap configuration. Each of the four ports is exemplarily supplied with a voltage amplitude of 1 mV. The electric field features a symmetrical distribution following the electrode's geometry. Three cut planes exemplarily show the electric field at different depths along the z-axis. Thus, this provides a promising platform for, e.g., the interaction with atoms or ions in a cavity. Possible applications include the controlled trapping and excitation of atoms [59, 138–141]. The presented platform paves the road to realize those applications at a much smaller footprint.

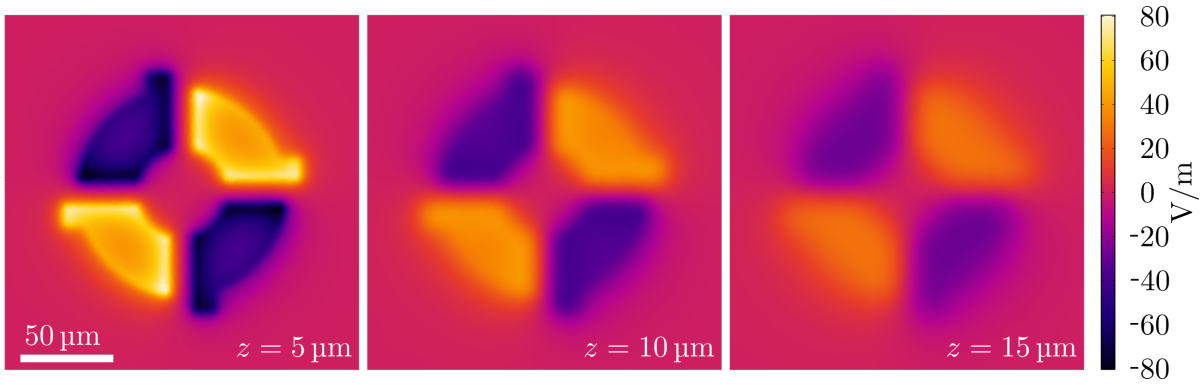

Figure 5.15: The electric field emitted by the electrodes arranged as shown in Fig. 5.9, simulated using Comsol Multiphysics. Depicted is the z-component of the electric field, located at various xy-cut planes, spaced at distances $z = (5, 10, 15)$ µm from the fiber endfacet. The applied potential on the electrode is +1 mV and −1 mV, respectively. The configuration represents a Paul trap. The scaling in size and the color bar used do not change between the three graphs.

Ω-Shape Similar to the simulation presented above, a FEM simulation is applied to determine the fields that emerge from an Ω-shaped antenna. In this case, the magnetic field induced by a current in the antenna is of interest. Figure 5.16 shows the amplitude of the magnetic field. The simulation reveals a homogeneous magnetic field, with a small perturbation at the position that corresponds to the connectors of the antenna. Regarding its possible applications, the magnetic field of the antenna allows for interaction with, e.g., a nitrogen-vacancy (NV) center placed at the endfacet of the fiber. Recent findings have shown that the presence of a magnetic field near a NV center can influence the stimulated emission of the latter [142]. The presented versatile method allows for a compact fabrication of such a tunable system.

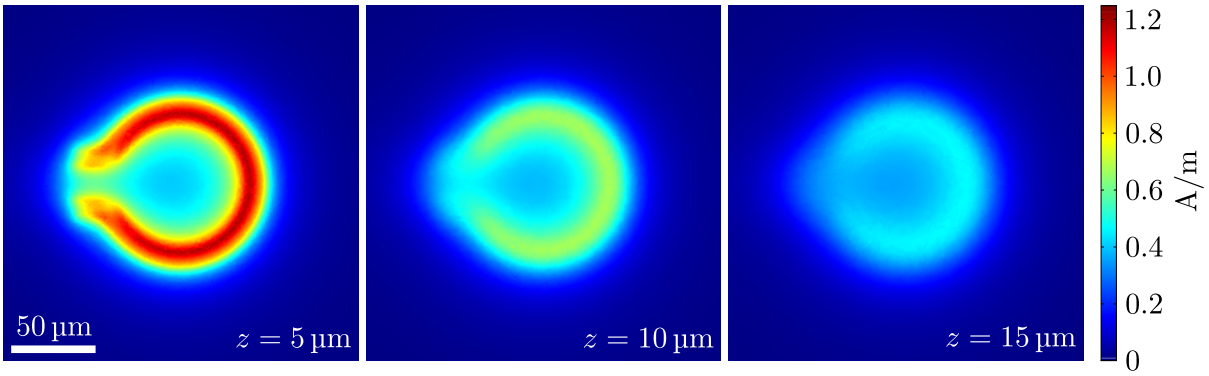

Figure 5.16: Results of the FEM simulation for the magnetic field emitted by the Ω-shaped antenna following the geometry presented in Fig. 5.10. Depicted is the amplitude of the magnetic field H obtained by excitation with an amplitude of 1 mV at the side of the fiber. The present current is calculated via the simulated impedance of the structure, which amounts to $|Z| = 1.8\,\Omega$ in this idealized setup of the simulation. The current thus amounts to 0.56 mA. The three graphs, which share the same scale, show the field in various distances z from the endfacet of the fiber. Apart from the region where the antenna is connected to the feeding conductors at the side of the fiber, the field exhibits a symmetrical distribution.

CHAPTER 6

Outlook

The presented results have shown exemplary realizations of FFPCs and the possibility of adding functionality to those by the method of DLW. It is possible to fabricate a vast number of different arbitrary structures for light-matter interactions. One possibility to improve the optomechanical experiments shown is the further adjustment of the geometry used, e.g., in terms of maximized coupling strength.
The optimization of the geometry goes hand in hand with improving the surface quality to reduce scattering losses further. While a systematic procedure was applied here to result in high-quality surfaces, the application of additional post-development procedures, as well as the usage of different photoresists, may provide possibilities for even lower surface roughness. This would lead to an improvement in the finesse and hence also allow for a wider range in light-induced tuning of the mechanical frequency.
The usage of different materials changes the mechanical and optical properties of the structures so that the resist selection can be tailored to the application. The spectrum of the available photoresists is continuously increasing and does no longer only cover polymeric materials, as the fabrication of fused silica structures via DLW [143] or the fabrication of metallic structures [144] has shown. Nevertheless, one is not even limited to photoresists: It is possible to create a scaffold via DLW, which is then equipped with additional material, e.g., by thermal evaporation of one or more dielectric layers on top. Afterwards, the underlying polymeric scaffold structure can precisely be removed by a suitable process, e.g., plasma ashing. This would allow, for example, for the application of DBR systems as a membrane, providing a significantly improved surface roughness in addition to their optical properties. Another approach to equip the structure with different materials is the possibility to grow material on a printed scaffold, compare [145, 146].
Furthermore, an adhesion promoter, for example PDMS, could be applied to pick up material mechanically. This way, atomically thin layers could be applied to the optomechanical system, either on top of a membrane or even as a membrane. Since those monolayers may serve as quantum emitters [147, 148], the resulting system features a quantum source, whose position can be tuned, hosted in a cavity. This way, a link between optomechanical experiments and the broad research field of atomically thin layers can be established.

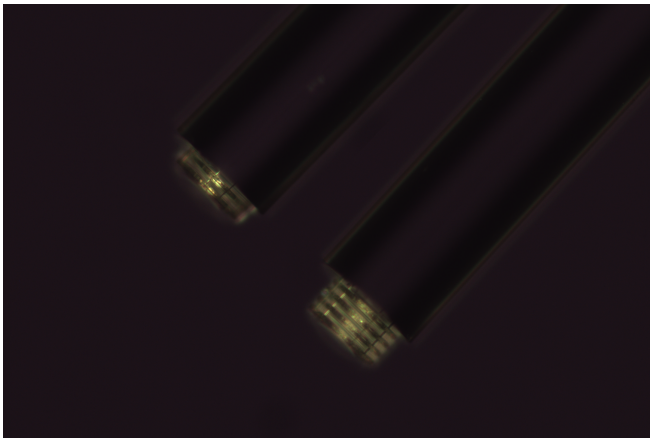

Figure 6.1: Fibers with stacked optomechanical structures: The left fiber is equipped with two membranes, while the right one features four. These fibers can be used to build cavities divided into multiple segments interacting with each other.

Changing the point of view, the presented experiments also allow for a characterization of the material used: We have found that, especially in the cryogenic regime, the cavity response is highly dependent on the mechanical properties of the material. Hence, unknown mechanical properties can be quantified via this setup.
Another way to expand on the shown methods is to investigate multi-membrane systems [149]. One way of realization is the stacking of membranes on top of each other, compare Fig. 6.1, resulting in very compact systems. The membranes of this construct could then be coupled and form a cavity setup that would provide multiple segments interacting with each other [150]. Similarly, multiple linked membranes could be positioned laterally next to each other, for example, on a half-inch substrate. This can be used to act as a mechanical metamaterial in two dimensions: The optical spring effect may be used to tune the individual mechanical properties. Hence, the individual tuning is significantly less complex than in comparable systems [151]. These mechanical metamaterials may serve for vibration routing in two dimensions and for distributed sensing.

The presented method of structuring fiber endfacets with masks allows for applications beyond the presented examples. The fabrication of the masks via DLW provides the possibility for arbitrary structures. For example, abraded fibers or even whole ferrules can be equipped with fitting masks. For the deposition of material, one is not limited to the usage of metals: If available, dielectric layers, for example forming a DBR, can be applied via ion beam evaporation. In this thesis, the creation of a ferrule via DLW allowed for the contacting of the electrode pads of the fiber. Due to the resist used, the vacuum compatibility of the final construct may be limited. One approach to overcome this issue might be the coverage of the ferrule with an additional layer before assembly. Atomic layer deposition might supply a shielding of the polymeric structure that prevents outgassing. Another approach can be taken by manipulating commercially available glass ferrules. Channels need to be drilled for the insertion of fuzz buttons and external wires. This way, polymeric structures would be omitted entirely, enabling vacuum applications without restrictions.

The resulting setup, comprising a fiber mirror equipped with electrodes, which are accessed by external wires, can be used in an FFPC setup. This FFPC provides a very compact and rigid platform for the manipulation of single atoms or ions. For example, quantum repeaters would benefit from the compactness of the resonators. Quantum repeaters enable the distribution of quantum information over long distances and thus would make the anticipated quantum internet possible. Due to the decay of quantum information transmitted via fibers, quantum repeaters, serving as nodes in the network, become necessary. In the anticipated system, such nodes are positioned in the order of $O(10 - 100\,\mathrm{km})$ apart from each other [152]. At the node position the signal is processed by the help of a quantum memory. At the moment, the most promising candidates for the realization are trapped atoms/ions, nitrogen-vacancy centers, or quantum dots [152]. If atoms or ions integrated in FFPCs prove useful, the presented manipulation of fibers provides a versatile platform for the creation of these FFPCs, resulting in rigid, customizable, cost-efficient, and compact resonators.

Combining the findings of both projects, electrodes can be integrated in an optomechanical setup of an FFPC. A mask would for example shield parts of a membrane during an evaporation process. The electrode-equipped structure can then be used as optomechanical device in an FFPC. Previous findings have shown the tunability of optomechanical structures by electrostatic [153] or piezoelectric [154] manipulation of the cavity properties. The polymeric structure can either serve as a membrane for the MIM configuration or it is used as the end mirror of a cavity, being directly mounted on top of the fiber mirror [155, 156]. Hence, our approach may lead to the development of an ultra-compact electrically tunable resonator.

CHAPTER 7

Summary

DLW serves as a powerful tool for fabricating arbitrary three-dimensional structures on the micrometer scale. We presented the application of structures fabricated via DLW inside FFPCs, aiming at providing additional functionality into those. This work covered the fabrication and characterization of optomechanical structures inside an FFPC as well as the structured metalization of fiber endfacets and the associated contacting of those. The versatile applications in combination with optical fibers provide a platform for experiments with integrated optical and electrical features.

The design of the polymeric structure that is subject to the interaction with the light field in the optomechanical experiments was optimized. On the one hand, a finite element method was applied to investigate the expected mechanical properties of the structure. On the other hand, a systematic experimental search for fabrication parameters yielding the minimal surface roughness of the fabricated polymeric structure was performed. Based on the finding of those processes, structures were applied on both DBR substrates and fiber mirrors. In contrast to the membranes that were mostly used up to now in optomechanical experiments, the DLW-fabricated membranes exhibit a large membrane thickness in the order of several λ. The optomechanical coupling strength for the membrane-in-the-middle setup was measured in atmospheric conditions. The temperature-dependency of the linewidth and the shift of the mechanical resonance frequency in atmospheric, vacuum, and cryogenic environments were investigated. An optomechanical coupling strength up to a value of $g_0/2\pi \approx 30\,\mathrm{kHz}$ was observed. Hence, the coupling strength surpasses the mechanical linewidth in the cryogenic regime.

In addition, the optical spring effect was investigated on the basis of the printed structures. A wavelength-tunable pumping laser was utilized to obtain a frequency shift of the mechanical mode. The maximum observed frequency shift yielded in $\Delta\Omega_\mathrm{m}/2\pi = 31\,\mathrm{kHz}$ for an input pump power of 6.8 mW, exceeding the mechanical linewidth of the structure at cryogenic conditions. The measurement of the mechanical frequency shift depending on the detuning between pump and probe laser and on the pump laser's power input was in good agreement with the theoretical predictions.

The versatile fabrication procedure, the reduction of the linewidth via cooling, the ability of light-induced tuning of the mechanical mode, and the possibility to apply a broad range of materials provide a powerful platform for the implementation of further optomechanical experiments.

Furthermore, we have presented a method to create almost arbitrary metallic patterns on optical fiber endfacets. The usage of DLW-fabricated masks allows for the application of structured metallic films directly on top of the fiber. Hence, FFPCs with integrated electrodes, e.g., for creating electrical or magnetic fields inside the cavity region, can be realized. We presented two designs, a fiber segmented into four separate electrodes for applying an electrical field as well as an Ω-shaped antenna for the creation of a magnetic field. The associated numerical simulations revealed the expected field distributions. For contacting, a ferrule was fabricated via DLW. This allowed for a design featuring dedicated channels for the insertion of the optical fiber and external conducting elements, reducing the hassle of aligning both. As conduction promoters, fuzz buttons filled the gaps between the evaporated pads on the fiber's side and gold wires. Due to the usage of non-magnetic fuzz buttons and a metallic film of copper or gold on the fiber without any adhesion layer, no material with magnetic dipole moment might disturb the cavity region. The electrical connection of the construct was shown exemplary by measuring a resistance of 11 Ω of the setup with Ω-shaped antenna on an optical fiber.
The presented approach paves the way for numerous applications: Via using masks during an evaporation process, almost arbitrary structures on a variety of workpieces can be fabricated featuring details on the micrometer scale. One is not limited to the metallic films presented here since, likewise, dielectrics can be applied by, e.g., ion beam evaporation. This method allows for the creation of structures onto substrates that are not accessible by conventional nanofabrication methods. The presented elements can serve as components for very compact cavities for the trapping of particles, e.g., as part of quantum repeater nodes.

Bibliography

[1] K. J. Vahala, *Optical microcavities*, Nature **424**, 839–46 (2003).

[2] A. A. Savchenkov, A. B. Matsko, V. S. Ilchenko, and L. Maleki, *Optical resonators with ten million finesse*, Optics Express **15**, 6768–73 (2007).

[3] Y.-N. Zhang, Y. Zhao, and R.-Q. Lv, *A review for optical sensors based on photonic crystal cavities*, Sensors and Actuators A: Physical **233**, 374–89 (2015).

[4] M.-C. Lee and M. C. Wu, *MEMS-actuated microdisk resonators with variable power coupling ratios*, IEEE Photonics Technology Letters **17**, 1034–6 (2005).

[5] M. L. Gorodetsky, A. A. Savchenkov, and V. S. Ilchenko, *Ultimate Q of optical microsphere resonators*, Optics Letters **21**, 453–5 (1996).

[6] D. Meschede, *Optik, Licht und Laser*, Vieweg+Teubner, 2008.

[7] J. L. Bromberg, *The birth of the laser*, Physics Today **41**, 26–33 (1988).

[8] J. Ye, D. Vernooy, and H. Kimble, *Trapping of single atoms in cavity QED*, Physical Review Letters **83**, 4987 (1999).

[9] G. Berden, R. Peeters, and G. Meijer, *Cavity ring-down spectroscopy: Experimental schemes and applications*, International Reviews in Physical Chemistry **19**, 565–607 (2000).

[10] Q. Qiao, J. Xia, C. Lee, and G. Zhou, *Applications of photonic crystal nanobeam cavities for sensing*, Micromachines **9**, 541 (2018).

[11] N. Ismail, C. C. Kores, D. Geskus, and M. Pollnau, *Fabry–Pérot resonator: Spectral line shapes, generic and related Airy distributions, linewidths, finesses, and performance at low or frequency-dependent reflectivity*, Optics Express **24**, 16366–89 (2016).

[12] W. Rosenfeld, *A high finesse optical resonator for cavity QED experiments*, Diploma Thesis, Rheinische Friedrich-Wilhelms-Universität Bonn, 2003.

[13] H. Walther, B. T. Varcoe, B.-G. Englert, and T. Becker, *Cavity quantum electrodynamics*, Reports on Progress in Physics **69**, 1325 (2006).

[14] R. Holzwarth, M. Zimmermann, T. Udem, and T. Hänsch, *Optical clockworks and the measurement of laser frequencies with a mode-locked frequency comb*, IEEE Journal of Quantum Electronics **37**, 1493–501 (2001).

[15] T. W. Hänsch, *Nobel lecture: Passion for precision*, Reviews of Modern Physics **78**, 1297 (2006).

[16] I. Georgescu, *Nobel Prize 2012: Haroche & Wineland*, Nature Physics **8**, 777–7 (2012).

[17] D. J. Wineland, *Nobel Lecture: Superposition, entanglement, and raising Schrödinger's cat*, Reviews of Modern Physics **85**, 1103 (2013).

[18] B. C. Barish and R. Weiss, *LIGO and the detection of gravitational waves*, Physics Today **52**, 44–50 (1999).

[19] B. Abbott, R. Abbott, R. Adhikari, P. Ajith, B. Allen, G. Allen, R. Amin, S. Anderson, W. Anderson, M. Arain, et al., *LIGO: The laser interferometer gravitational-wave observatory*, Reports on Progress in Physics **72**, 076901 (2009).

[20] R. Weiss, *Nobel Lecture: LIGO and the discovery of gravitational waves I*, Reviews of Modern Physics **90**, 040501 (2018).

[21] F. Marquardt and S. M. Girvin, *Optomechanics*, Physics **2**, 40 (2009).

[22] P. Jones, O. Maragó, and G. Volpe, *Optical tweezers*, Cambridge University Press, 2015.

[23] H. Mabuchi and A. Doherty, *Cavity quantum electrodynamics: Coherence in context*, Science **298**, 1372–7 (2002).

[24] Z. Shen, *Experimental Research of Cavity Optomechanics*, Springer Nature, 2021.

[25] S. Gigan, H. Böhm, M. Paternostro, F. Blaser, G. Langer, J. Hertzberg, K. C. Schwab, D. Bäuerle, M. Aspelmeyer, and A. Zeilinger, *Self-cooling of a micromirror by radiation pressure*, Nature **444**, 67–70 (2006).

[26] A. Schliesser, R. Rivière, G. Anetsberger, O. Arcizet, and T. J. Kippenberg, *Resolved-sideband cooling of a micromechanical oscillator*, Nature Physics **4**, 415–9 (2008).

[27] Y.-S. Park and H. Wang, *Resolved-sideband and cryogenic cooling of an optomechanical resonator*, Nature Physics **5**, 489–93 (2009).

[28] E. Verhagen, S. Deléglise, S. Weis, A. Schliesser, and T. J. Kippenberg, *Quantum-coherent coupling of a mechanical oscillator to an optical cavity mode*, Nature **482**, 63–7 (2012).

[29] G. Gagliardi and H.-P. Loock, *Cavity-enhanced spectroscopy and sensing*, vol. 179, Springer, 2014.

[30] B.-B. Li, L. Ou, Y. Lei, and Y.-C. Liu, *Cavity optomechanical sensing*, Nanophotonics **10**, 2799–832 (2021).

[31] R. W. Andrews, R. W. Peterson, T. P. Purdy, K. Cicak, R. W. Simmonds, C. A. Regal, and K. W. Lehnert, *Bidirectional and efficient conversion between microwave and optical light*, Nature Physics **10**, 321–6 (2014).

[32] I. Favero and K. Karrai, *Optomechanics of deformable optical cavities*, Nature Photonics **3**, 201–5 (2009).

[33] M. Aspelmeyer, T. J. Kippenberg, and F. Marquardt, *Cavity optomechanics*, Reviews of Modern Physics **86**, 1391 (2014).

[34] B. D. Hauer, T. J. Clark, P. H. Kim, C. Doolin, and J. P. Davis, *Dueling dynamical backaction in a cryogenic optomechanical cavity*, Physical Review A **99**, 053803 (2019).

[35] M. Eichenfield, J. Chan, R. M. Camacho, K. J. Vahala, and O. Painter, *Optomechanical crystals*, Nature **462**, 78–82 (2009).

[36] X. Sun, X. Zhang, and H. X. Tang, *High-Q silicon optomechanical microdisk resonators at gigahertz frequencies*, Applied Physics Letters **100**, 173116 (2012).

[37] S. Gröblacher, K. Hammerer, M. R. Vanner, and M. Aspelmeyer, *Observation of strong coupling between a micromechanical resonator and an optical cavity field*, Nature **460**, 724–7 (2009).

[38] A. Gillespie and F. Raab, *Thermally excited vibrations of the mirrors of laser interferometer gravitational-wave detectors*, Physical Review D **52**, 577 (1995).

[39] D. Hunger, T. Steinmetz, Y. Colombe, C. Deutsch, T. W. Hänsch, and J. Reichel, *A fiber Fabry–Perot cavity with high finesse*, New Journal of Physics **12**, 065038 (2010).

[40] T. Steinmetz, Y. Colombe, D. Hunger, T. Hänsch, A. Balocchi, R. Warburton, and J. Reichel, *Stable fiber-based Fabry–Pérot cavity*, Applied Physics Letters **89**, 111110 (2006).

[41] C. A. Saavedra, *Development of tunable fiber Fabry–Pérot micro-resonators with high passive stability: A demonstration for molecular oxygen gas spectroscopy*, Ph.D. Thesis, Universidad de Guanajuato, 2022.

[42] J. Baraillon, B. Taurel, P. Labeye, and L. Duraffourg, *A lensed fiber Bragg grating-based membrane-in-the-middle optomechanical cavity*, Scientific Reports **12**, 1–12 (2022).

[43] X. Zhou, S. Venkatachalam, R. Zhou, H. Xu, A. Pokharel, A. Fefferman, M. Zaknoune, and E. Collin, *High-Q silicon nitride drum resonators strongly coupled to gates*, Nano Letters **21**, 5738–44 (2021).

[44] X. Chen, C. Chardin, K. Makles, C. Caër, S. Chua, R. Braive, I. Robert-Philip, T. Briant, P.-F. Cohadon, A. Heidmann, et al., *High-finesse Fabry–Perot cavities with bidimensional Si_3N_4 photonic-crystal slabs*, Light: Science & Applications **6**, e16190–e16190 (2017).

[45] S. Maruo, O. Nakamura, and S. Kawata, *Three-dimensional microfabrication with two-photon-absorbed photopolymerization*, Optics Letters **22**, 132–4 (1997).

[46] T. Gissibl, S. Wagner, J. Sykora, M. Schmid, and H. Giessen, *Refractive index measurements of photo-resists for three-dimensional direct laser writing*, Optical Materials Express **7**, 2293–8 (2017).

[47] R. Borisov, G. Dorojkina, N. Koroteev, V. Kozenkov, S. Magnitskii, D. Malakhov, A. Tarasishin, and A. Zheltikov, *Fabrication of three-dimensional periodic microstructures by means of two-photon polymerization*, Applied Physics B: Lasers & Optics **67**, (1998).

[48] M. Deubel, G. Von Freymann, M. Wegener, S. Pereira, K. Busch, and C. M. Soukoulis, *Direct laser writing of three-dimensional photonic-crystal templates for telecommunications*, Nature Materials **3**, 444–7 (2004).

[49] T. Gissibl, S. Thiele, A. Herkommer, and H. Giessen, *Two-photon direct laser writing of ultracompact multi-lens objectives*, Nature Photonics **10**, 554–60 (2016).

[50] N. Rohbeck, R. Ramachandramoorthy, D. Casari, P. Schürch, T. E. Edwards, L. Schilinsky, L. Philippe, J. Schwiedrzik, and J. Michler, *Effect of high strain rates and temperature on the micromechanical properties of 3D-printed polymer structures made by two-photon lithography*, Materials & Design **195**, 108977 (2020).

[51] R. K. Jayne, T. J. Stark, J. B. Reeves, D. J. Bishop, and A. E. White, *Dynamic Actuation of Soft 3D Micromechanical Structures Using Micro-Electromechanical Systems (MEMS)*, Advanced Materials Technologies **3**, 1700293 (2018).

[52] S. Kawata, H.-B. Sun, T. Tanaka, and K. Takada, *Finer features for functional microdevices*, Nature **412**, 697–8 (2001).

[53] A. Selimis, V. Mironov, and M. Farsari, *Direct laser writing: Principles and materials for scaffold 3D printing*, Microelectronic Engineering **132**, 83–9 (2015).

[54] J. Li, S. Thiele, R. W. Kirk, B. C. Quirk, A. Hoogendoorn, Y. C. Chen, K. Peter, S. J. Nicholls, J. W. Verjans, P. J. Psaltis, et al., *3D-printed micro lens-in-lens for in vivo multimodal microendoscopy*, Small **18**, 2107032 (2022).

[55] A. Asadollahbaik, S. Thiele, K. Weber, A. Kumar, J. Drozella, F. Sterl, A. M. Herkommer, H. Giessen, and J. Fick, *Highly efficient dual-fiber optical trapping with 3D printed diffractive fresnel lenses*, ACS Photonics **7**, 88–97 (2019).

[56] P. Ruchka, S. Hammer, M. Rockenhäuser, R. Albrecht, J. Drozella, S. Thiele, H. Giessen, and T. Langen, *Microscopic 3D printed optical tweezers for atomic quantum technology*, Quantum Science and Technology **7**, 045011 (2022).

[57] H. Pfeifer, L. Ratschbacher, J. Gallego, C. Saavedra, A. Faßbender, A. von Haaren, W. Alt, S. Hofferberth, M. Köhl, S. Linden, et al., *Achievements and perspectives of optical fiber Fabry–Perot cavities*, Applied Physics B **128**, 1–15 (2022).

[58] T. Ballance, H. Meyer, P. Kobel, K. Ott, J. Reichel, and M. Köhl, *Cavity-induced backaction in Purcell-enhanced photon emission of a single ion in an ultraviolet fiber cavity*, Physical Review A **95**, 033812 (2017).

[59] P. Kobel, M. Breyer, and M. Köhl, *Deterministic spin-photon entanglement from a trapped ion in a fiber Fabry–Perot cavity*, npj Quantum Information **7**, 1–7 (2021).

[60] F. L. Pedrotti, L. M. Pedrotti, and L. S. Pedrotti, *Introduction to optics*, Cambridge University Press, 2017.

[61] Y. Miroshnychenko, *Design and test of an optical high finesse resonator for single atom experiments*, Diploma Thesis, Rheinische Friedrich-Wilhelms-Universität Bonn, 2002.

[62] D. Z. Anderson, *Alignment of resonant optical cavities*, Applied Optics **23**, 2944–9 (1984).

[63] Y. Mizuyama, "How to Analyze Laser Cavity Stability with Multiphysics Ray Tracing," *Comsol Blog*, 2017.

[64] J. Gallego, S. Ghosh, S. K. Alavi, W. Alt, M. Martinez-Dorantes, D. Meschede, and L. Ratschbacher, *High-finesse fiber Fabry–Perot cavities: Stabilization and mode matching analysis*, Applied Physics B **122**, 1–14 (2016).

[65] J. Gallego Fernandez, *Strong coupling between small atomic ensembles and an open fiber cavity*, Ph.D. Thesis, Rheinische Friedrich-Wilhelms-Universität Bonn, 2017.

[66] L. Tenbrake, *Fiber cavity optomechanics with polymer membranes*, Master Thesis, Rheinische Friedrich-Wilhelms-Universität Bonn, 2021.

[67] R. B. Griffiths, *Consistent quantum theory*, Cambridge University Press, 2003.

[68] A. A. Clerk and F. Marquardt, "Basic theory of cavity optomechanics," *Cavity Optomechanics*, Springer, 2014 5–23.

[69] B. S. Sheard, M. B. Gray, C. M. Mow-Lowry, D. E. McClelland, and S. E. Whitcomb, *Observation and characterization of an optical spring*, Physical Review A **69**, 051801 (2004).

[70] T. J. Kippenberg and K. J. Vahala, *Cavity opto-mechanics*, Optics Express **15**, 17172–205 (2007).

[71] F. Marquardt, *Quantum optomechanics*, Quantum machines: Measurement and control of engineered quantum systems (Les Houches Session XCVI), edited by M. Devoret, B. Huard, R. Schoelkopf, and L. Cugliandolo, (2011).

[72] P.-F. Cohadon, A. Heidmann, and M. Pinard, *Cooling of a mirror by radiation pressure*, Physical Review Letters **83**, 3174 (1999).

[73] V. Braginsky and S. Vyatchanin, *Low quantum noise tranquilizer for Fabry–Perot interferometer*, Physics Letters A **293**, 228–34 (2002).

[74] A. Jayich, J. Sankey, B. Zwickl, C. Yang, J. Thompson, S. Girvin, A. Clerk, F. Marquardt, and J. Harris, *Dispersive optomechanics: A membrane inside a cavity*, New Journal of Physics **10**, 095008 (2008).

[75] M. Aspelmeyer, T. J. Kippenberg, and F. Marquardt, "Chapter 1 - Introduction," *Cavity optomechanics: Nano- and micromechanical resonators interacting with light*, ed. by M. Aspelmeyer, T. J. Kippenberg, and F. Marquardt, Springer, 2014 1–4.

[76] I. Favero, J. Sankey, and E. M. Weig, "Mechanical resonators in the middle of an optical cavity," *Cavity Optomechanics*, Springer, 2014 83–119.

[77] K. Ujihara, *Output coupling in optical cavities and lasers: A quantum theoretical approach*, John Wiley & Sons, 2010.

[78] S. G. Johnson, M. Ibanescu, M. Skorobogatiy, O. Weisberg, J. Joannopoulos, and Y. Fink, *Perturbation theory for Maxwell's equations with shifting material boundaries*, Physical Review E **65**, 066611 (2002).

[79] R. Drever, J. L. Hall, F. Kowalski, J. Hough, G. Ford, A. Munley, and H. Ward, *Laser phase and frequency stabilization using an optical resonator*, Applied Physics B **31**, 97–105 (1983).

[80] E. D. Black, *An introduction to Pound–Drever–Hall laser frequency stabilization*, American Journal of Physics **69**, 79–87 (2001).

[81] M. Nickerson, *A review of Pound–Drever–Hall laser frequency locking*, JILA, University of Colorado and NIST, (2019).

[82] Y. Feng, *Laser Frequency Stabilization with Pound–Drever–Hall Technique*, Master Thesis, Cornell University, 2015.

[83] P. Dudek, *FDM 3D printing technology in manufacturing composite elements*, Archives of Metallurgy and Materials **58**, 1415–8 (2013).

[84] S. Wickramasinghe, T. Do, and P. Tran, *FDM-based 3D printing of polymer and associated composite: A review on mechanical properties, defects and treatments*, Polymers **12**, 1529 (2020).

[85] A. Kafle, E. Luis, R. Silwal, H. M. Pan, P. L. Shrestha, and A. K. Bastola, *3D/4D Printing of polymers: Fused deposition modelling (FDM), selective laser sintering (SLS), and stereolithography (SLA)*, Polymers **13**, 3101 (2021).

[86] J. Z. Manapat, Q. Chen, P. Ye, and R. C. Advincula, *3D printing of polymer nanocomposites via stereolithography*, Macromolecular Materials and Engineering **302**, 1600553 (2017).

[87] M. T. Gale and K. Knop, "The fabrication of fine lens arrays by laser beam writing," *Industrial Applications of Laser Technology*, vol. 398, SPIE, 1983 347–53.

[88] M. T. Gale, G. K. Lang, J. M. Raynor, and H. Schütz, "Fabrication of microoptical components by laser beam writing in photoresist," *Micro-Optics II*, vol. 1506, SPIE, 1991 65–70.

[89] M. T. Gale, M. Rossi, J. Pedersen, and H. Schütz, *Fabrication of continuous-relief micro-optical elements by direct laser writing in photoresists*, Optical Engineering **33**, 3556–66 (1994).

[90] M. Thiel, J. Fischer, G. Von Freymann, and M. Wegener, *Direct laser writing of three-dimensional submicron structures using a continuous-wave laser at 532 nm*, Applied Physics Letters **97**, 221102 (2010).

[91] H.-B. Sun and S. Kawata, *Two-photon photopolymerization and 3D lithographic microfabrication*, NMR• 3D Analysis• Photopolymerization, 169–273 (2004).

[92] M. Wöhlecke, K. Betzler, and M. Imlau, *Nonlinear optics*, Script, Fachbereich Physik, Universität Oldenburg, 2003.

[93] J. B. Müller, J. Fischer, and M. Wegener, "Chapter 3 - Reaction mechanisms and in situ process diagnostics," *Three-dimensional microfabrication using two-photon polymerization*, ed. by T. Baldacchini, Micro and Nano Technologies, Oxford: William Andrew Publishing, 2016 82–101.

[94] Nanoscribe GmbH & Co. KG, *IP-S Photoresist Material Safety Data Sheet*, 2017.

[95] K. Ruhland, F. Habibollahi, and R. Horny, *Quantification and elucidation of the UV-light triggered initiation kinetics of TPO and BAPO in liquid acrylate monomer*, Journal of Applied Polymer Science **137**, 48357 (2020).

[96] S. Jockusch and N. J. Turro, *Phosphinoyl radicals: Structure and reactivity. A laser flash photolysis and time-resolved ESR investigation*, Journal of the American Chemical Society **120**, 11773–7 (1998).

[97] J. B. Müller, *Exploring the mechanisms of three-dimensional direct laser writing by multi-photon polymerization*, Ph.D. Thesis, Karlsruher Institut für Technologie, 2015.

[98] K.-S. Lee, R. H. Kim, P. Prabhakaran, D.-Y. Yang, T. W. Lim, and S. H. Park, *Two-photon stereolithography*, Journal of Nonlinear Optical Physics & Materials **16**, 59–73 (2007).

[99] L. Sui, X. Wang, D. Zhao, and J. Qu, *Application of 3D laser scanner for monitoring of landslide hazards*, The International Archives of the Photogrammetry, Remote Sensing and Spatial Information Sciences **37**, (2008).

[100] P. R. Apeagyei et al., *Application of 3D body scanning technology to human measurement for clothing Fit*, International Journal of Digital Content Technology and its Applications **4**, 58–68 (2010).

[101] J. Tong, J. Zhou, L. Liu, Z. Pan, and H. Yan, *Scanning 3D full human bodies using kinects*, IEEE Transactions on Visualization and Computer Graphics **18**, 643–50 (2012).

[102] P. Bazylewski, S. Ezugwu, and G. Fanchini, *A review of three-dimensional scanning near-field optical microscopy (3D-SNOM) and its applications in nanoscale light management*, Applied Sciences **7**, 973 (2017).

[103] J. Wang, "Surface preparation techniques for biomedical applications," *Coatings for Biomedical Applications*, Elsevier, 2012 143–75.

[104] L. Tenbrake, A. Faßbender, S. Hofferberth, S. Linden, and H. Pfeifer, *Direct laser-written optomechanical membranes in fiber Fabry–Perot cavities*, arXiv preprint arXiv:2212.13532, (2022).

[105] T. Frenzel, M. Kadic, and M. Wegener, *Three-dimensional mechanical metamaterials with a twist*, Science **358**, 1072–4 (2017).

[106] *Structural Mechanics Module User's Guide*, Comsol Multiphysics GmbH, 2019.

[107] J. Dean, *Introduction to the Finite Element Method (FEM)*, University of Cambridge, Department of Materials Science & Metallurgy.

[108] A. H. Safavi-Naeini and O. Painter, "Chapter 10 - Optomechanical crystal devices," *Cavity optomechanics: Nano- and micromechanical resonators interacting with light*, ed. by M. Aspelmeyer, T. J. Kippenberg, and F. Marquardt, Springer, 2014 195–231.

[109] C. Saavedra, D. Pandey, W. Alt, H. Pfeifer, and D. Meschede, *Tunable fiber Fabry–Perot cavities with high passive stability*, Optics Express **29**, 974–82 (2021).

[110] R. Kitamura, L. Pilon, and M. Jonasz, *Optical constants of silica glass from extreme ultraviolet to far infrared at near room temperature*, Applied Optics **46**, 8118–33 (2007).

[111] D. Röser, *Fiber Fabry–Perot cavities for quantum information and spectroscopy*, Master Thesis, Rheinische Friedrich-Wilhelms-Universität Bonn, 2019.

[112] M. A. Scharfstädt, *Implementation of a micro-mirror production setup for quantum information applications*, Master Thesis, Rheinische Friedrich-Wilhelms-Universität Bonn, 2022.

[113] M. Schmid, D. Ludescher, and H. Giessen, *Optical properties of photoresists for femtosecond 3D printing: Refractive index, extinction, luminescence-dose dependence, aging, heat treatment, and comparison between 1-photon and 2-photon exposure*, Optical Materials Express **9**, 4564–77 (2019).

[114] Y. Li, S. Park, M. McLamb, M. Lata, S. Schöche, D. Childers, I. Aggarwal, M. Poutous, G. Boreman, and T. Hofmann, *UV to NIR optical properties of IP-Dip, IP-L, and IP-S after two-photon polymerization determined by spectroscopic ellipsometry*, Optical Materials Express **9**, 4318–28 (2019).

[115] P. R. Saulson, *Thermal noise in mechanical experiments*, Physical Review D **42**, 2437 (1990).

[116] M. Gorodetksy, A. Schliesser, G. Anetsberger, S. Deleglise, and T. J. Kippenberg, *Determination of the vacuum optomechanical coupling rate using frequency noise calibration*, Optics Express **18**, 23236–46 (2010).

[117] G. Hartwig, *Polymer properties at room and cryogenic temperatures*, Springer Science & Business Media, 1995.

[118] E. D. Lemma, F. Rizzi, T. Dattoma, B. Spagnolo, L. Sileo, A. Qualtieri, M. De Vittorio, and F. Pisanello, *Mechanical properties tunability of three-dimensional polymeric structures in two-photon lithography*, IEEE Transactions on Nanotechnology **16**, 23–31 (2016).

[119] S. Chung and S. Park, *Effects of temperature on mechanical properties of SU-8 photoresist material*, Journal of Mechanical Science and Technology **27**, 2701–7 (2013).

[120] C. Zener, *Internal friction in solids II. General theory of thermoelastic internal friction*, Physical Review **53**, 90 (1938).

[121] E. Serra, F. Cataliotti, F. Marin, F. Marino, A. Pontin, G. Prodi, and M. Bonaldi, *Inhomogeneous mechanical losses in micro-oscillators with high reflectivity coating*, Journal of Applied Physics **111**, 113109 (2012).

[122] A. H. Ghadimi, S. A. Fedorov, N. J. Engelsen, M. J. Bereyhi, R. Schilling, D. J. Wilson, and T. J. Kippenberg, *Elastic strain engineering for ultralow mechanical dissipation*, Science **360**, 764–8 (2018).

[123] M. J. Bereyhi, A. Beccari, S. A. Fedorov, A. H. Ghadimi, R. Schilling, D. J. Wilson, N. J. Engelsen, and T. J. Kippenberg, *Clamp-tapering increases the quality factor of stressed nanobeams*, Nano Letters **19**, 2329–33 (2019).

[124] Y. Tsaturyan, A. Barg, E. S. Polzik, and A. Schliesser, *Ultracoherent nanomechanical resonators via soft clamping and dissipation dilution*, Nature Nanotechnology **12**, 776–83 (2017).

[125] K.-S. Lee, R. H. Kim, D.-Y. Yang, and S. H. Park, *Advances in 3D nano/microfabrication using two-photon initiated polymerization*, Progress in Polymer Science **33**, 631–81 (2008).

[126] Z. Hu, Z.-B. Liu, and J.-G. Tian, *Stacking of exfoliated two-dimensional materials: A review*, Chinese Journal of Chemistry **38**, 981–95 (2020).

[127] O. Arcizet, P.-F. Cohadon, T. Briant, M. Pinard, and A. Heidmann, *Radiation-pressure cooling and optomechanical instability of a micromirror*, Nature **444**, 71–4 (2006).

[128] M. Hossein-Zadeh, H. Rokhsari, A. Hajimiri, and K. J. Vahala, *Characterization of a radiation-pressure-driven micromechanical oscillator*, Physical Review A **74**, 023813 (2006).

[129] M. Hossein-Zadeh and K. J. Vahala, *Observation of optical spring effect in a microtoroidal optomechanical resonator*, Optics Letters **32**, 1611–3 (2007).

[130] T. Carmon, L. Yang, and K. J. Vahala, *Dynamical thermal behavior and thermal self-stability of microcavities*, Optics Express **12**, 4742–50 (2004).

[131] P. Rohse, J. Butlewski, F. Klein, T. Wagner, C. Friesen, A. Schwarz, R. Wiesendanger, K. Sengstock, and C. Becker, *A cavity optomechanical locking scheme based on the optical spring effect*, Review of Scientific Instruments **91**, 103102 (2020).

[132] M. Ludwig, *Optomechanics in the Quantum Regime*, Diploma Thesis, Ludwig-Maximilians-Universität München, 2008.

[133] J. Ma, *Photothermal nonlinearity in optical cavities and optomechanical systems*, Ph.D. Thesis, The Australian National University, 2020.

[134] C. W. Gardiner and M. J. Collett, *Input and output in damped quantum systems: Quantum stochastic differential equations and the master equation*, Physical Review A **31**, 3761 (1985).

[135] M. Teller, D. A. Fioretto, P. C. Holz, P. Schindler, V. Messerer, K. Schüppert, Y. Zou, R. Blatt, J. Chiaverini, J. Sage, et al., *Heating of a trapped ion induced by dielectric materials*, Physical Review Letters **126**, 230505 (2021).

[136] J. Hoogvliet and W. Van Bennekom, *Gold thin-film electrodes: An EQCM study of the influence of chromium and titanium adhesion layers on the response*, Electrochimica Acta **47**, 599–611 (2001).

[137] P. Benjamin and C. Weaver, *The adhesion of evaporated metal films on glass*, Proceedings of the Royal Society of London. Series A. Mathematical and Physical Sciences **261**, 516–31 (1962).

[138] W. Paul, *Electromagnetic traps for charged and neutral particles*, Reviews of Modern Physics **62**, 531 (1990).

[139] M. Steiner, H. M. Meyer, C. Deutsch, J. Reichel, and M. Köhl, *Single ion coupled to an optical fiber cavity*, Physical Review Letters **110**, 043003 (2013).

[140] J. Millen, P. Fonseca, T. Mavrogordatos, T. Monteiro, and P. Barker, *Cavity cooling a single charged levitated nanosphere*, Physical Review Letters **114**, 123602 (2015).

[141] K. Schüppert, *Quantum interface - A fiber cavity perpendicular to a linear ion trap*, Ph.D. Thesis, Leopold-Franzens-Universität Innsbruck, 2020.

[142] F. A. Hahl, L. Lindner, X. Vidal, T. Luo, T. Ohshima, S. Onoda, S. Ishii, A. M. Zaitsev, M. Capelli, B. C. Gibson, et al., *Magnetic-field-dependent stimulated emission from nitrogen-vacancy centers in diamond*, Science Advances **8**, eabn7192 (2022).

[143] F. Kotz, A. S. Quick, P. Risch, T. Martin, T. Hoose, M. Thiel, D. Helmer, and B. E. Rapp, *Two-photon polymerization of nanocomposites for the fabrication of transparent fused silica glass microstructures*, Advanced Materials **33**, 2006341 (2021).

[144] E. H. Waller, J. Karst, and G. von Freymann, *Photosensitive material enabling direct fabrication of filigree 3D silver microstructures via laser-induced photoreduction*, Light: Advanced Manufacturing **2**, 228–33 (2021).

[145] F. Klein, B. Richter, T. Striebel, C. M. Franz, G. v. Freymann, M. Wegener, and M. Bastmeyer, *Two-component polymer scaffolds for controlled three-dimensional cell culture*, Advanced Materials **23**, 1341–5 (2011).

[146] L. Brigo, A. Urciuolo, S. Giulitti, G. Della Giustina, M. Tromayer, R. Liska, N. Elvassore, and G. Brusatin, *3D high-resolution two-photon crosslinked hydrogel structures for biological studies*, Acta Biomaterialia **55**, 373–84 (2017).

[147] T. T. Tran, K. Bray, M. J. Ford, M. Toth, and I. Aharonovich, *Quantum emission from hexagonal boron nitride monolayers*, Nature Nanotechnology **11**, 37–41 (2016).

[148] Y.-M. He, G. Clark, J. R. Schaibley, Y. He, M.-C. Chen, Y.-J. Wei, X. Ding, Q. Zhang, W. Yao, X. Xu, et al., *Single quantum emitters in monolayer semiconductors*, Nature Nanotechnology **10**, 497–502 (2015).

[149] P. Piergentili, R. Natali, D. Vitali, and G. Di Giuseppe, "Two-membrane cavity optomechanics: Linear and non-linear dynamics," *Photonics*, vol. 9, MDPI, 2022 99.

[150] A. Xuereb, C. Genes, and A. Dantan, *Strong coupling and long-range collective interactions in optomechanical arrays*, Physical Review Letters **109**, 223601 (2012).

[151] H. Pfeifer, T. Paraiso, L. Zang, and O. Painter, *Design of tunable GHz-frequency optomechanical crystal resonators*, Optics Express **24**, 11407–19 (2016).

[152] P. van Loock, W. Alt, C. Becher, O. Benson, H. Boche, C. Deppe, J. Eschner, S. Höfling, D. Meschede, P. Michler, et al., *Extending quantum links: Modules for fiber- and memory-based quantum repeaters*, Advanced Quantum Technologies **3**, 1900141 (2020).

[153] R. Perahia, J. Cohen, S. Meenehan, T. M. Alegre, and O. Painter, *Electrostatically tunable optomechanical "zipper" cavity laser*, Applied Physics Letters **97**, 191112 (2010).

[154] C. Xiong, L. Fan, X. Sun, and H. X. Tang, *Cavity piezooptomechanics: Piezoelectrically excited, optically transduced optomechanical resonators*, Applied Physics Letters **102**, 021110 (2013).

[155] J. C. Williams, *Dynamic micromechanical Fabry–Perot cavity sensors fabricated by multiphoton absorption onto optical fiber tips*, Master Thesis, Air Force Institute of Technology, Wright-Patterson Air Force Base, Ohio, 2020.

[156] J. W. Smith, J. C. Williams, J. S. Suelzer, N. G. Usechak, and H. Chandrahalim, *Three-dimensional Fabry–Pérot cavities sculpted on fiber tips using a multiphoton polymerization process*, Journal of Micromechanics and Microengineering **30**, 125007 (2020).

Glossary

ABS	Acrylnitrit-Butadien-Styrol-Copolymere
AFM	Atomic Force Microscope
BAPO	Bis(2,4,6-Trimethylbenzoyl)-Phenylphosphineoxide
BS	Beam Splitter
CAD	Computer-Aided Design
DBR	Distributed Bragg Reflector
DLW	Direct Laser Writing
EOM	Electro-Optical Modulator
ESA	Electrical Spectrum Analyzer
FDM	Fused Deposition Modeling
FEM	Finite Element Method
FFPC	Fiber Fabry–Pérot Cavity
FSR	Free Spectral Range
FWHM	Full Width at Half Maximum
ITO	Indium Tin Oxide
LCD	Liquid Crystal Display
LPF	Low-Pass Filter
MIM	Membrane-in-the-Middle
NIR	Near-Infrared
NMP	N-Methyl-2-Pyrrolidon
NV	Nitrogen-Vacancy
OPA	One-Photon Absorption
PBS	Polarizing Beam Splitter
PD	Photodiode
PDH	Pound–Drever–Hall
PDMS	Polydimethylsiloxane
PETA	Pentaerythritol Triacrylate
PGMEA	Propylene Glycol Methyl Ether Acetate
PLA	Polylactic Acid
PSD	Power Spectral Density
RF	Radio Frequency
SEM	Scanning Electron Microscope
SLA	Stereolithography Apparatus
SoF	Side-of-Fringe
TPA	Two-Photon Absorption
UV	Ultraviolet
ZPM	Zero-Point Motion

Publications

Parts of this thesis have been published in scientific journals:

- H. Pfeifer, L. Ratschbacher, J. Gallego, C. Saavedra, A. Faßbender, A. von Haaren, W. Alt, S. Hofferberth, M. Köhl, S. Linden and D. Meschede, *Achievements and perspectives of optical fiber Fabry–Perot cavities*, Applied Physics B **128**, 1–15 (2022), https://doi.org/10.1007/s00340-022-07752-8.
- L. Tenbrake, A. Faßbender, S.Hofferberth, S. Linden and H. Pfeifer, *Direct laser-written optomechanical membranes in fiber Fabry–Perot cavities*, arXiv preprint arXiv:2212.13532 (2022).

Acknowledgements

At the end of my thesis, I thank all the people who supported me during the last few years.

First of all, I would like to thank Prof. Dr. Stefan Linden for giving me the opportunity to work on this interesting project. Starting from the time of my bachelor's thesis in 2015 and covering the time of my master's thesis in 2017, I was able to perform research on various interesting topics within the Nanophotonics group. Every project on its own provided fascinating research work in an inspiring environment. The opportunity to deal with a project involving the direct laser writing system enabled insights into multiple interesting topics.
Thank you for the fruitful discussions, the guidance through the project, and – equally important – the off-time on hiking tours, barbecue events, or conference trips. Thank you to Priv.-Doz. Dr. Elisabeth Soergel for being the second supervisor of my thesis. I learned a lot from the numerous proseminar courses. Not only contentwise but also from the point of structuring!
I want to thank Prof. Dr. David Luitz and Prof. Dr. Ulrike Endesfelder for joining the committee.

The presented project was partly founded by the research grants FaResQ, Q.Link.X, and QR.X. I am grateful for the support provided, including the financial aspect, networking, and collaborations that emerged from the meetings.
I want to thank Dr. Hannes Pfeifer and Lukas Tenbrake from the group of Prof. Dr. Sebastian Hofferberth, formerly of the group of Prof. Dr. Dieter Meschede. It was a fruitful collaboration that yielded not only in the results and experiments shown but has also been a lot of fun! Additionally, Hannes and Lukas provided a lot of assistance that covered more than just the topics of our joint project. I really could rely on your support all the time, which was marvelous!
I want to thank all members of the Nanophotonics group, especially former and present Ph.D. students Mike Prämassing, Till Leuteritz, Zlata Fedorova, Lok-Yee Yan, Yuhao Zhang, Hans-Joachim Schill, Anna Sidorenko, Paul Steinmann, and Max Wegerhoff. You provided a delightful and enjoyable working atmosphere.
Last but not least, I thank my parents for their continuous support. Thank you for your love and help. If I had not had this, I surely would not have been able to get it to this point. Thanks to my sister Isabel for the dental emergency action on very short notice during the writing period of this thesis. Finally, I would like to thank Leonie for the love and support throughout the recent years.